# INVESTIGATING THE EFFECTS OF NETWORK STRUCTURE AND AFFERENT FEEDBACK IN MODELS OF RHYTHMIC MOVEMENT

by

**Lucy E. Spardy**

B.S. Mathematics, Duquesne University, 2005

M.A. Mathematics, University of Pittsburgh, 2008

Submitted to the Graduate Faculty of

the Department of Mathematics in partial fulfillment

of the requirements for the degree of

**Doctor of Philosophy**

University of Pittsburgh

2012

UNIVERSITY OF PITTSBURGH

MATHEMATICS DEPARTMENT

This dissertation was presented

by

Lucy E. Spardy

It was defended on

July 16th 2012

and approved by

Jonathan E. Rubin, Department of Mathematics

Brent Doiron, Department of Mathematics

G. Bard Ermentrout, Department of Mathematics

Douglas J. Weber, Department of Physical Medicine & Rehabilitation

Dissertation Director: Jonathan E. Rubin, Department of Mathematics

# INVESTIGATING THE EFFECTS OF NETWORK STRUCTURE AND AFFERENT FEEDBACK IN MODELS OF RHYTHMIC MOVEMENT

Lucy E. Spardy, PhD

University of Pittsburgh, 2012

Animals can generate distinct rhythmic behaviors using a shared set of muscles and motoneurons, and in certain cases, the structure responsible for generating these movements is unknown. Distinct networks could be dedicated solely to particular behaviors, a singular network could control various movements through reorganization or under different inputs, or a hybrid of these two concepts could exist. In the first chapter of this thesis, we explore the compatibility of different network characteristics with experimental results regarding swimming and scratching rhythm generation in the turtle. We propose three distinct architectures that represent a range of connectivity between networks responsible for these rhythms, and test their performance against a set of experimental benchmarks regarding dual stimulation. The results of our modeling concur with experimental results, suggesting that networks that generate locomotion and scratching share important components.

In the second and third chapters, we focus our attention on a previously published neuromechanical locomotor model. In this closed loop system, a central pattern generator (CPG) establishes a rhythm under sufficient supra-spinal drive and controls the activity of a pendular limb, which sends afferent signals back to the CPG, affecting its operation. Increasing the drive to the CPG increases the limb frequency through changes in the stance phase duration only, which is a key feature of normal overground locomotion. Using geometric singular perturbation theory, we analyze the mechanisms responsible for rhythm generation in the CPG, both in the presence and absence of feedback. We exploit our observations to construct a reduced model that is qualitatively similar to the original, but tractable for

rigorous discussion. We prove the existence of a locomotor cycle in this reduced system using a novel version of the Melnikov function, adapted for discontinuous systems. We highlight how the limb dynamics shape overall model behavior, and indicate a crucial relationship between components that controls the model's asymmetric response to drive changes. Finally, we utilize our understanding of the model dynamics to explain its performance under various modifications, including recovery of oscillatory behavior after spinal cord injury and response to changes in load.

**Keywords:** central pattern generators (CPGs), rhythm generation, escape, release, central nervous system (CNS).

# TABLE OF CONTENTS

# LIST OF TABLES

# LIST OF FIGURES

# PREFACE

for thoroughness and work ethic. Trevor, who was always there to proofread, motivate, and listen. Travis, who showed me the meaning of being a truly great friend. Justin, who never failed to ground me when I was on the ledge.

To my parents, who have always encouraged me to be the best version of myself, but have always accepted me as I am. And to Nikki and Sarah – if I have nothing else but the two of you, I have everything.

This thesis is dedicated in loving memory of Katie Michel. Your unparalleled tenacity, courage, and spirit is a constant source of inspiration to me. I would not be half the person I am today without you.

# 1.0  INTRODUCTION

In the early 1900s, T. Graham Brown showed that the mammalian spinal cord could generate stepping patterns without rhythmic afferent input, proposing the idea of the half-center oscillator model of the spinal locomotor network [11, 12]. Views shared by Sherrington and others proposed an alternative concept, that the spinal cord contained sufficient sensory reflex circuitry to produce the basic alternation of flexor and extensor activity in locomotion [67, 52], with switching in the locomotor cycle triggered by sensory feedback. The former viewpoint was generally ignored in favor of the latter until fifty years later, when the idea that locomotion could be produced by the central nervous system (CNS) in absence of sensory afferents was again demonstrated in other systems like the locust, where oscillatory behavior replicating the rhythm seen in flight was exhibited despite the removal of timed sensory inputs [82] and in the deafferented crayfish abdominal nerve cord, which could generate coordinated spiking in motor axons, seen during forward swimming [52]. Rhythmic patterns in absence of sensory feedback in in vitro experiments in newts, cockroaches, leeches, and cats, provided further evidence that alternating flexor and extensor activity could be produced solely by the central nervous system [52].

Brown's original concept of a half-center model was later tailored by Lundberg to provide the prevailing structure of two excitatory neural populations driving flexor and extensor motoneurons and inhibiting each other via inhibitory interneurons. These networks, which produce oscillatory output in absence of rhythmic input and sensory afferents, are referred to as *central pattern generators* (CPGs). CPGs underlie a wide variety of repetitive movements, such as breathing, swallowing, swimming, and many others.

A fundamental question that remains to be answered regards the structure of networks responsible for generating rhythmic movements from a shared set of muscles and motoneu-

rons. On one end of the spectrum, distinct CPGs could be configured solely for individual tasks, and on the other, a multifunctional circuitry might be able to produce various rhythms under different inputs or reorganization. Certainly a hybrid of these two configurations could exist, where distinct networks overlap and share key components. Identifying the neurons central to the circuitry responsible for certain movements can be a difficult task for motor systems physiologists, however, due to both the complexity of the CNS and because neurons can be embedded within regions responsible for other functions [44].

Evidence from recordings in both invertebrate and vertebrate systems indicates that individual interneurons participate in multiple rhythms generated by the same set of muscles and motoneurons. Some examples include tadpole and zebrafish swimming and struggling, mollusk withdrawal and escape swimming, cat scratch and walking, and in multiple forms of scratching in the turtle [51, 8, 33]. These observations posit the concept that a singular network is capable of generating distinct rhythms under various inputs. However, evidence from zebrafish larvae, adult turtles, and hatching tadpoles suggest that in addition to multifunctional neurons, some networks possess specialized interneurons which are selectively activated during certain behaviors, and silent or inhibited during others. Therefore, networks underlying multiple rhythms might be comprised of multifunctional neurons working in conjunction with specialized interneurons that can be called upon to select and generate various patterns. For smaller invertebrate networks where complete connectivity diagrams can be produced (like in the crustacean stomatogastric system), whether networks generating various rhythms are unitary, distinct, or separate but overlapping can be resolved [32]. In the large vertebrate nervous system, however, the structure of the spinal network cannot easily be deduced from individual neuron recordings [32].

To test the degree to which networks responsible for distinct rhythms overlap, experimentalists simultaneously provide stimuli responsible for evoking either rhythm in isolation. If the resultant motor pattern exhibits hybrid dynamics between the patterns, like frequency increases, rearranged motoneuron firing, or even interruptions, inferences can be drawn indicating shared circuitry underlying the rhythms. In Chapter 2, we will investigate the structure of the network underlying scratching and swimming rhythms in the adult red-eared turtle. In previous work [32], our collaborators generated experimental results indicating

that shared circuitry is involved in producing these rhythms, and we used the performance of a few simple mathematical models to suggest the potential network architecture capable of yielding their results. We will extend that preliminary modeling by a thorough investigation of the capabilities of the proposed models, comparing and contrasting our results with those published in [32], and indicate some limitations of the modeling, along with future directions for studying this problem.

While it is imperative to emphasize the fundamental role that CPGs play in rhythm generation, it is vital that one does not unintentionally neglect the important influence of sensory feedback. Certainly, the ability to locomote with ease in our environment offers many evolutionary rewards and in light of differing terrains, various obstacles, and other perturbations, stable gait could not be achieved without the contribution of sensory feedback. Despite the fact that flight in the locust was shown to be inherent to the CNS, it was also shown that the cycle frequency was greatly reduced without sensory input, indicating that the presence of feedback, while not necessary for the basic alternating pattern, is an important component to modulate the rhythm [82]. In many other systems, it has been shown that feedback can set the overall timing of the step cycle by facilitating the switch between locomotor phases, influence selection or suppression of motor patterns, aide in proper foot placement in uneven terrain, and countless other considerations [81, 44, 46, 61]. Understanding how rhythm generating units synthesize afferent commands is, therefore, a key question for scientists investigating problems in locomotion, respiration, and other rhythmic activities.

One characteristic feature of normal overground locomotion in most mammals is that an increase in speed is achieved through a shortening of the stance phase, during which a limb is in contact with the ground, without change in the duration of the swing phase, during which the limb moves without ground contact [31, 27]. The source of this asymmetry could potentially lie in the CPG structure, in the set of drives to the CPG from supraspinal sources such as the brain stem, or in the afferent feedback to the CPG, and which possibility is correct remains the subject of scientific debate [39, 26, 35]. The suggestion that this asymmetric response indicates a CPG that is wired to modulate the step cycle through changes in extensor burst durations has been contradicted by experimental studies

3

of fictive locomotion using decerebrate, immobilized cat preparations [41, 84] and recent investigations of deletions, or spontaneous errors, during fictive locomotion [41, 64, 65, 48] which provide evidence for a symmetrical, half-center organization of the spinal locomotor CPG. In fact, under electrical stimulation of the midbrain locomotor region, variations in cycle duration were accomplished through modulations of flexor, not extensor, bursts in the majority of the cases [84], further indicating that the CPG is not inherently biased. In that same paper, a simple model was produced that could fit data favoring either extensor controlled or flexor controlled locomotion, provided that an offset factor (input to either half-center) was asymmetric, suggesting that the CPG might produce an asymmetric response due to an asymmetric drive signal.

In Chapters 3 and 4, we consider the alternative hypothesis, that the asymmetric response could be accomplished via feedback control in spite of symmetries in both the CPG and top down drive. We focus our attention on a model that Markin et al. [46] recently proposed, where a locomotor CPG is coupled to a mechanical limb segment. Given a sufficiently strong, constant drive, the CPG oscillates and controls two antagonistic muscles, whose anti-phase contractions force a pendular limb. Feedback signals, based on muscle length/velocity and force, are generated and sent back to the CPG, closing the loop. The model is able to generate periodic oscillations with frequencies that depend on drive strength over a wide range of values. The CPG is symmetric in the sense that its extensor and flexor components are identical, and in the absence of feedback, frequency increases occur through an equivalent shortening of both extensor and flexor phases. When afferent feedback is introduced, however, the model exhibits asymmetric changes in phase durations in response to drive alterations that match closely with experimental results, providing evidence that CPG or drive asymmetry is not necessary for this behavior. Our primary goal is to use dynamical systems analysis to explain the mechanisms underlying the performance of this computational model, as a step towards establishing general conditions under which the observed simulation results can be expected to hold, clarifying which model features are essential to its behaviors, and enhancing the predictive capacity of the model. In Chapter 3, we explain how the presence of feedback initiates phase transitions in the CPG at a particular relationship between limb position and velocity, overriding the intrinsic mechanism responsible for

4

oscillations in the open loop configuration. Mathematical analysis of a model implementing continuous feedback signals can be particularly complex, so we offer a reduced model whose performance is qualitatively similar to the original, but tractable for analysis. We show that this model admits a periodic solution under certain conditions, adapting classical theorems from dynamical systems theory to apply to our system, which exhibits discontinuities due to particular model terms. These discontinuities create natural divisions in the locomotor cycle, and we highlight the different dynamics present in each of these phases in Chapter 4. Proximity of the limb trajectory to a saddle point in phase space causes one phase in particular to be sensitive to changes in motoneuron output, and hence, drive strength, explaining the phase asymmetry and indicating a key relationship that must be supported in order for the model to generate oscillatory behavior.

In the rest of Chapter 4, our understanding of the model's operation under baseline conditions allows us to explain its performance under various perturbations. For instance, the body regularly responds to adjustments in load, whether they be gradual, due to weight loss or gain, or instantaneous, such as walking assisted by a hand rail. To determine how load affects the kinematics of walking, studies have been performed on subjects where a percentage of body weight is supported by a harness over a range of treadmill speeds. These experiments indicate that as body weight support is increased, the phase asymmetry characteristic is reduced, meaning that the stance duration takes up less of the overall cycle duration [36, 63]. We implement a comparative study in this model by reducing the strength of the ground contact force. This modification affects the relationship between the limb trajectory and the saddle point at stance onset and significantly reduces the dependence of the stance phase duration on drive, replicating the reduction in the phase asymmetry characteristic.

Another discussion with far reaching applications is whether the body can regain locomotor function after spinal trauma. Studies have produced evidence that recovery of locomotion can occur after rehabilitation with regular treadmill training, and/or pharmacology, with the general consensus being that this occurs in part due to strengthening the feedback connections to the weakly excited CPG [46]. We can mimic the effects of spinal trauma by setting the constant drive parameter to zero in this model. The limb does not oscillate under this modification, but oscillatory behavior can be recovered when the strength of afferent feed-

back is increased. We show that when drive is absent, motoneuron activity is too weak to sustain the crucial relationship between the limb trajectory and saddle point. We explain how increasing the feedback results in restoration of the necessary alignment, indicating precisely how distinct feedback signals affect the particular components that promote synergy between the CPG and the limb.

Finally, a limbless locomotor model has suggested that the CPG contains the input-output relationship of the behavior it controls, and that input to the CPG might be expressed as the desired speed of movement [83]. Without a limb, input to the CPG in that model corresponds to supra-spinal drive only, and speed of movement is calculated from CPG cycle duration based on a relationship generated by experiments [31]. Investigating the relationship between input to the CPG and output frequency using the neuromechanical model offers two extensions to this study: input, in this case, corresponds to both descending and sensory sources, and speed can be determined using both the suggested relationship and separately using the limb kinetics. We will analyze the crucial role that feedback plays in this topic, utilizing our analysis to explain, and in some cases suggest alterations to optimize, the linear relationship that is produced between these two variables.

## 2.0 DETERMINING THE SPINAL NETWORK STRUCTURES UNDERLYING RHYTHMIC MOVEMENT IN TURTLES

In this chapter, we employ mathematical modeling to infer the structure underlying rhythm generation in the turtle spinal cord. The turtle model is an excellent subject for study for multiple reasons. First, the turtle is a diving animal that possesses effective hypoxia defense strategies, allowing it to withstand hypoxia/anoxia much better than other mammals, allowing preparations to remain healthy up to three times as long [43]. In addition, to efficiently study the performance of a motor system, a complete description of the behavior in question must be obtained. This includes a classification of the sequence of muscle activation responsible for the behavior, identification of the motoneurons controlling those muscles, and understanding which interneurons participate in the rhythm. Depending on the system to be studied, some of these tasks can be very difficult, for instance, when certain interneurons affecting a particular behavior are not active in phase with the behavior [44]. This is not the case for the adult red-eared turtle, where the behaviors are well described [42, 57, 50, 77]. In addition, a variety of movements can be independently evoked through specific stimuli.

Presenting stimuli responsible for different rhythmic behaviors simultaneously is a method experimentalists use to reveal network interactions. The resultant motoneuron pattern evoked from delivering these stimuli together can indicate whether the network(s) responsible for either rhythm share components. In [32], our collaborators experimentally investigated the level of interaction between networks responsible for turtle swimming and three forms of scratching, which are distinct rhythms that can be produced under various forms of stimulation in vivo. These rhythms are characterized by rhythmic alternation between hip flexor ($HF$) and hip extensor ($HE$) motoneurons, along with activation of knee extensor ($KE$), with distinct burst amplitudes and ordering of activation. Experiments regarding these

7

rhythms have been performed previously [22, 38], and have indicated that hybrid motor patterns and rhythm resetting can occur under brief dual stimulation. This newer work advanced these findings by considering dual scratching and swimming stimulation over several cycles. Frequency increases and hybrid features exhibited in the patterns generated by dual stimulation concurred with earlier results and indicated that the circuitry responsible for these rhythms overlaps.

Mathematical modeling can be used in conjunction with experiments to clarify results and offer testable predictions for further experiments. Here, we use mathematical models to explore the compatibility of different network characteristics with the results of our collaborators' experiments. These models represent a simplified version of the neuronal networks present in the spinal cord. We propose three unique architectures that represent various degrees of interaction within networks responsible for swimming and scratching. Model neurons in these networks are described by systems of ordinary differential equations where the variables representing voltage and gating processes operate on different timescales, enabling us to formalize arguments describing their activity using geometric singular perturbation theory. Through the models' ability or inability to produce experimental results regarding dual stimulation, we aim to mathematically infer the structure of the underlying network in the turtle spinal cord.

In Section 2.1, we provide a brief overview of the experiments performed by our collaborators, streamlining their conclusions into a concise list of benchmarks that guide our modeling attempts. An introduction to the neuronal dynamics and the various architectures under consideration is located in Section 2.2, and in Section 2.3, we present an overview of our preliminary modeling results (published along with experimental results from Section 2.1 in [32]). In that paper, differences in model output under various parameter choices led us to conclude that a particular structure was more likely to produce the experimental results than the others. The rest of the chapter is devoted to new work, dedicated to evaluating the extent to which our initial conclusions are dependent on parameter choices. To do this, we will randomly generate parameter sets for either modeling framework and ascertain the models' ability to support the prescribed benchmarks. In Section 2.4, we automate our search process by setting up algorithms to randomly generate sets of parameters and to evaluate

8

whether, under these choices, the models produce favorable dynamics. The networks we propose will be comprised of six neurons with various connectivity. In all of the structures, swim is evoked by a subset of three neurons. In Section 2.5, we will discuss the parameter sets we generated that produce swim dynamics in a 3-neuron model. We will use these sets to build the full modeling structures in Sections 2.6 and 2.7, and detail the performance of the models under these new parameter choices, attempting to deduce key features inherent to the sets that promote favorable dynamics. Finally, an observation that differentiated these models in [32] required parameter sets to produce particular dynamics under a certain stimulation. Random searches did not produce sets exhibiting these dynamics, so in Section 2.8 we present an analysis we performed to constrain parameter space. A targeted search in the regime indicated by this analysis was indeed able to produce sets that promoted desired results. In the discussion, we summarize our conclusions obtained from this investigation and indicate its limitations, highlighting our intentions for future work.

We will make ample use of abbreviations throughout this document. Some key terms used throughout Chapter 2 are listed in the upper portion of Table 1.

## 2.1 EXPERIMENTAL RESULTS YIELD A LIST OF BENCHMARKS

In an immobilized preparation, electrical stimulation in a particular area of the turtle body can elicit a swimming motoneuron pattern, and scratching the turtle surface in various locations elicits scratching motoneuron patterns (Figure 1). Simultaneous delivery of stimuli generating various behaviors reveals interactions between the networks responsible for these tasks. In [32], our collaborators investigated dual stimulation of various forms of scratches paired with forward swim. Their findings indicated that there is most likely a shared circuitry responsible for these movements, since under dual stimulation, the resulting motoneuron pattern could be a hybrid of the two rhythms, lead to interruptions, and exhibit a larger frequency than either the original swim or scratch alone. Though our collaborators considered three different scratch and swim pairings, we choose to focus on only one scratch rhythm, for simplicity. We selected caudal scratch because it exhibits phase differences that are most

9

| Term | Description |
|------|-------------|
| UCPG | Unitary CPG; singular architecture comprised of specialized and multifunctional interneurons |
| LCPG | Linked CPG; architecture comprised of distinct modules with interconnectivity |
| DCPG | Dyadic CPG; architecture comprised of distinct modules without interconnectivity |
| $KE$ | knee extensor motoneuron |
| $HF$ | hip flexor motoneuron |
| $HE$ | hip extensor motoneuron |
| $ke_j$ | knee extensor interneuron that projects to $KE$; $j \in 1, 2$ indicates scratch or swim CPG |
| $hf_j$ | hip flexor interneuron that projects to $HF$; $j \in 1, 2$ indicates scratch or swim CPG |
| $he_j$ | hip extensor interneuron that projects to $HE$; $j \in 1, 2$ indicates scratch or swim CPG |
| $i_k$ | scratch-specialized interneurons in UCPG |
| input/drive to $u_k$ | $\alpha I_{u_k}$ |
| total input to $u_k$ | $\alpha I_{u_k} - \sum_{u_j \neq u_k} b_{u_k u_j} u_j$ |
| $f_T$ | function that calculates the output activity of each neuron, 'T' indicates turtle |
| subswim | reduced swim stimulation strength; generates tonic or below threshold firing among swim neurons |
| UnitaryT, UnitaryS | published UCPG parameter sets that generate tonic and below threshold firing under subswim, respectively |
| LinkedT, LinkedS | published LCPG parameter sets that generate tonic and below threshold firing under subswim, respectively |
| $\alpha$ | parameter controlling the strength of the swim stimulus |
| $\beta$ | parameter controlling the strength of the drive to $ke$ and $hf$ alone |
| S collection | 3-neuron parameter sets that produce below threshold firing when the swim stimulus is reduced |
| T collection | 3-neuron parameter sets that produce tonic activity by at least one neuron when the swim stimulus is reduced |
| $t_{me}$ | time point when the steady state of $(w_1, w_2)$ shifts away from $(1,0)$ with increasing $w_2$ |
| $t_e$ | time point when nullclines split and $(w_1, w_2)$ is attracted to $(0, 1)$ in fast time (escape mechanism) |
| $t_{mr}$ | time point when the steady state of $(w_1, w_2)$ shifts away from $(1,0)$ with decreasing $w_1$ |
| $t_r$ | time point when nullclines split and $(w_1, w_2)$ is attracted to $(0, 1)$ in fast time (release mechanism) |
| $d$ | constant supra-spinal drive fed to CPG neurons |
| $V_i$ | voltage drop across the membrane of neuron $i$ |
| $RG\text{-}k$ | rhythm generator neuron $k$; $k \in \{F, E\}$ |
| $In\text{-}k$ | inhibitory interneuron $k$; $k \in \{F, E\}$ |
| $PF\text{-}k$ | pattern formation neuron $k$; $k \in \{F, E\}$ |
| $Mn\text{-}k$ | motoneuron $k$; $k \in \{F, E\}$ |
| $q$ | limb angle with the horizontal |
| $v$ | limb angular velocity |
| $Ia\text{-}F$, $II\text{-}F$ | feedback terms to the flexor side |
| $Ia\text{-}E$, $Ib\text{-}E$ | feedback terms to the extensor side |
| $FB_i$ | summed feedback to neuron $i$ |
| $FB_{crit}$ | feedback required to excite an inactive $In$ above threshold; independent of drive |
| $TTC$ | Stance Transition Curve; location in limb phase space where flexor activates |
| $WTC$ | Swing Transition Curve; location in limb phase space where extensor activates |
| eStance | portion of the locomotor phase where $Mn\text{-}E$ is active and ground reaction is present |
| fStance | portion of the locomotor phase where $Mn\text{-}F$ is active and ground reaction is present |
| eSwing | portion of the locomotor phase where $Mn\text{-}E$ is active and ground reaction is absent |
| fSwing | portion of the locomotor phase where $Mn\text{-}F$ is active and ground reaction is absent |
| $I$ | moment of inertia of limb with respect to suspension point |
| $K$ | coefficient of gravitational moment |
| $b$ | angular viscosity in the hinge joint |
| $M_{GRmax}$ | amplitude of moment of ground reaction force |
| $M_E$, $M_F$, $M_{GR}$ | moment applied to limb from flexor, extensor, or ground reaction |
| $f_C$ | function that calculates the output activity of each neuron, 'C' indicates cat |
| $H$ | Heaviside function that calculates inhibitory output in the reduced model |
| $m_{phase}$ | fixed, drive-dependent motoneuron output during phase; obtained from time average of original model |
| $\{\}$ | notation indicating that the constant within is piecewise (phasewise) defined |
| $x_\epsilon = (q_\epsilon, v_\epsilon)$ | saddle point of system $\dot{x} = f(x) + \epsilon g(x)$ for $\epsilon \in [0, 1]$ |
| $W^u(x_\epsilon), W^s(x_\epsilon)$ | unstable, stable manifold from $x_\epsilon$ |
| $\tilde{W}^s(x_\epsilon)$ | trajectory governed by the eSwing vector field that converges to $x_\epsilon$ as $v \uparrow 0$ |
| $\gamma_0$ | homoclinic orbit emanating from $x_0$ |
| $\Sigma$ | transversal to the flow |
| $\mathcal{M}$ | Melnikov function; sign indicates how the homoclinic perturbs with increasing $\epsilon$ |
| $M^*_{phase}$ | fixed muscle moment during phase; obtained to produce negative Melnikov sign |
| $h^k(\epsilon) = (h^k_q(\epsilon), h^k_v(\epsilon))$ | intersection of the stable and unstable manifolds with $\Sigma$; $k \in \{u, s\}$ |

10

**Table 1:** *Key notation for common terms in Chapters 2 and 3.*
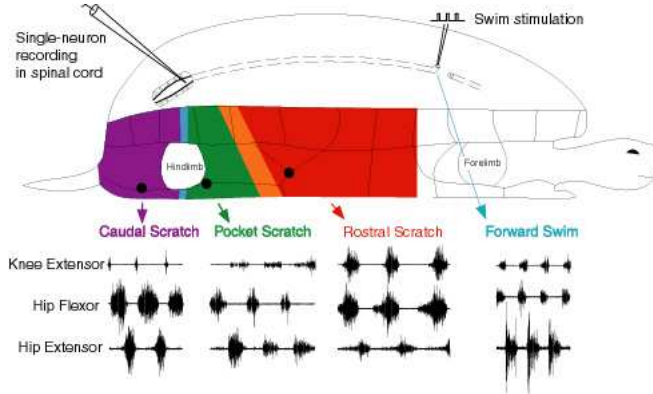
**Figure 1:** *Turtle stimulation schematic. Applying electrical or manual stimulation in the colored portions of the turtle body produce swim or scratch motoneuron patterns. Republished from [9], with permission from Annals of the New York Academy of Sciences.*

distinct from those occurring in forward swim ([23, 42, 57], see the traces in Figure 1). See Figure 2 for another example of a caudal scratch and forward swim motoneuron pattern, along with evidence for frequency increases under dual stimulation in two animals. Below, we summarize our collaborators' relevant experimental results in a succinct list of modeling benchmarks.

Any model we propose must:

1. produce a swim and scratch motoneuron pattern under distinct patterns of constant stimulation to model neurons

2. increase the frequency of the swim rhythm when the strength of the swim drive is increased ([42]);

3. under dual stimulation, output a pattern with a higher frequency than the frequencies of the swim or scratch rhythms alone;

4. produce swim when reduced swim stimulation is applied with full scratch stimulation.

These benchmarks are the guidelines we will use when evaluating the performance of our models. In the next section, we provide a rigorous definition of the scratch and swim rhythms, as well as the mathematical description of neurons in our models and the various architectures we will analyze.

11
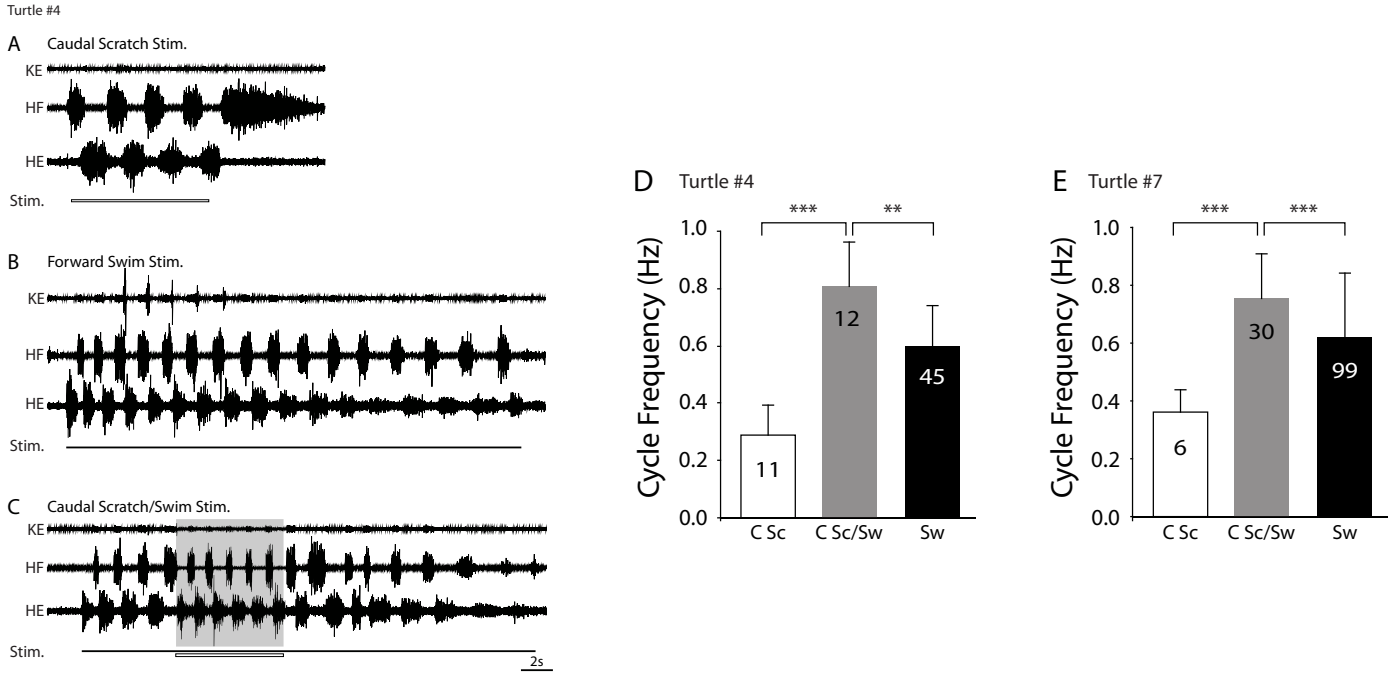
**Figure 2:** *Caudal scratch and forward swim dual stimulation produces motoneuron patterns with an increased frequency than either alone. Application of stimuli is indicated below motoneuron traces with a line. (A) and (B) motor pattern exhibited during caudal scratch and forward swim stimulation, respectively. (C) Dual stimulation applied during the shaded region exhibits a pattern with a larger frequency than in (A) or (B). (D), (E), Summary of two animals' performance under dual stimulation experiments. The rhythm exhibited under dual stimulation (gray bars) has a larger frequency than either swim or scratch frequencies alone (white and black bars). The numbers in each bar indicate the number of episodes/cycles considered. See [32] for more details.*

## 2.2   INTRODUCTION TO THE DISTINCT NETWORK ARCHITECTURES

To illustrate the ways in which outputs generated by different types of network architectures could or could not be consistent with our collaborators' experimental observations, we devise and test three simple network models, each featuring a particular architecture of connections among neurons (Figure 3). Each model consists of a small system of ordinary differential equations representing the activity of the interneurons in the network, with parameters tuned to produce forward swim and scratch rhythms in response to corresponding levels of constant

stimulation. Based on the features of rhythms evoked in physiological experiments, we define a swim rhythm as a periodic network output in which KE and HF are active together in anti-phase with HE, with active durations that satisfy $|KE| \approx |HF| < |HE|$. We define a scratch rhythm as a periodic network output in which activation proceeds from KE to HF to HE, with little or no overlap, and active durations satisfying $|KE| < |HF| << |HE|$, as seen experimentally in caudal scratch.

It has been suggested that one circuit may be responsible for the timing of cycles (i.e. rhythm generation), and separate circuits may be responsible for the phase and shape of each motor nerve burst (i.e. pattern generation) [49]. In each network, we make the simplifying assumption that rhythm and pattern generation are both accomplished by the same group of cells. The three models differ in terms of their CPG architectures (Figure 3). The
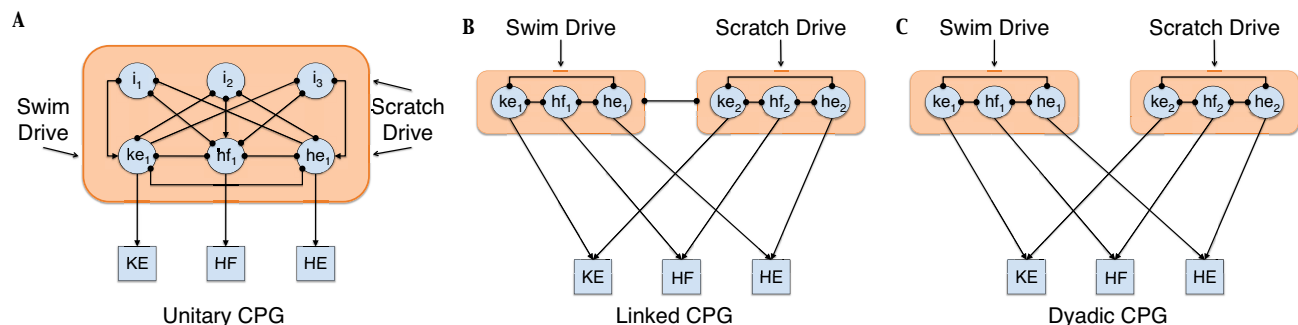


**Figure 3:** *Schematics for the three architectures considered. (A) In the UCPG, a subset of neurons in the CPG produces the swim rhythm, but scratch can be obtained by exciting the full set. (B,C) Each of the latter two structures is comprised of two separate CPGs - one that produces the swim rhythm, the other the scratch rhythm - but the LCPG (B) implements all to all connectivity between them, allowing output to be integrated prior to the motoneuron level. The DCPG (C) has no interconnectivity between structures. In all configurations, interneurons $\{ke, hf, he\}$ project to motoneurons $\{KE, HF, HE\}$, respectively. In the UCPG, additional driver cells $i_1, i_2, i_3$ are partnered with $ke_1, hf_1, he_1$, respectively, and provide additional excitation to these neurons under scratch stimulation (excitatory connections shown with an arrow). All other connections in the networks are inhibitory (inhibitory connections indicated with a circle)*

dyadic CPG (DCPG) is conceptually the simplest, consisting of two separate CPG modules – one able to produce a scratch rhythm and another that can generate a swim rhythm – that do not interact directly (Figure 3C). The linked CPG (LCPG) also includes distinct scratch and swim CPG modules but features inhibitory interactions between the modules

(Figure 3B). In each of these configurations, interneurons $\{ke, hf, he\}$ project to motoneurons $\{KE, HF, HE\}$, respectively, with subscripts to differentiate whether interneurons lie in the swim or scratch modules. The unitary CPG (UCPG) is comprised of a single, fully connected CPG able to generate both rhythms through the output of a collection of multifunctional and specialized neurons. Echoing the literature that indicates the existence of scratch-specialized neurons [9], the UCPG generates the swim rhythm when a subset of neurons is stimulated but produces scratch when that subset and an additional set of specialized neurons are activated together. We introduce these cells as extra "driver" cells – each specialized cell has a designated partner cell in the multifunctional network ($i_1$ with $ke_1$, $i_2$ with $hf_1$, and $i_3$ with $he_1$) to which it provides excitatory input (indicated with arrowed connections in Figure 3A). As in the previous architectures, the output of $\{ke_1, hf_1, he_1\}$ in this structure projects to motoneurons $\{KE, HF, HE\}$, respectively. The UCPG can be differentiated from the LCPG by the presence of excitatory connections and existence of multifunctional neurons. Specifically, in the UCPG, if any neuron from the set $\{ke_1, hf_1, he_1\}$ were shut off, the model would be unable to produce either rhythm. In the LCPG, no such neuron exists; suppressing one neuron from $\{ke_1, hf_1, he_1, ke_2, hf_2, he_2\}$ would affect the model's ability to perform either swim or scratch, but not both. In all three models, scratch and swim outputs of the CPG interact at the motoneuron level, and motoneuron activity is used to characterize network output. For simplicity, each network includes just three motoneurons, one corresponding to each of $KE, HF$, and $HE$.

Within each model, neurons are simulated using Wilson-Cowan equations [25] of the form

$$u'_k = -u_k + f_T(\alpha I_{u_k} - \sum_{u_j \neq u_k} b_{u_k u_j} u_j - g a_{u_k})$$

$$\tau_{u_k} a'_{u_k} = -a_{u_k} + u_k, \tag{2.1}$$

where $u$ is an element of the set $\{ke, hf, he, i\}$, representing the neuron's role within the network (see Figure 3 – in particular, $i$ denotes scratch-specialized neurons within the UCPG model); $I_{u_k}$ refers to a constant external drive, and

$$f_T(x) = 1/(1 + \exp(-r(x - \theta))) \tag{2.2}$$

14

with $\theta$=0.2, $g$=0.5, and $r$=10. In later sections, we will refer to a collection of $n$ neurons with dynamics described by equation (2.1) as an $n$-neuron (or $n$-cell) network. The variable $u_k$ represents a measure of the activity of neuron $k$ of type $u$, whereas $a_{u_k}$ denotes adaptation of the neuron. The parameter $b_{u_k u_j}$ denotes the connection strength from $u_j$ to $u_k$; $g$ quantifies the extent to which changes in adaptation affect activity; and $\tau_{u_k}$ denotes the time constant of adaptation, relative to the activity time constant of 1. For simplicity, we allow single neurons to send excitatory (negative $b$) outputs to some targets and inhibitory (positive $b$) outputs to others; identical results could be obtained by splitting such neurons into excitatory and inhibitory pairs. When we wish to refer only to the constant stimulus a neuron receives $(\alpha I_{u_k})$, we will use the term "drive" or "input." When we wish to include the effects of changes in inhibition from other neurons $(\alpha I_{u_k} - \sum_{u_j \neq u_k} b_{u_k u_j} u_j)$, we will use the term "total input."

The output of each motoneuron is defined simply by comparing the sum of its total input with a threshold, $\theta_{th} = 0.6$. That is, we compute $KE = [\sum ke_k - \theta]_+, HF = [\sum ke_k - \theta]_+,$ and $HE = [\sum ke_k - \theta]_+$, where we define

$$
[x]_+ = \begin{cases} h(x) & \text{if } x > 0; \\ 0 & \text{if } x \leq 0. \end{cases}
$$

In the UCPG model, each motoneuron receives input from only one neuron in the CPG. In the other two structures, input to a motoneuron is the summation of outputs from members of each module, as indicated in Figure 3. Since we do not model the effects of motoneuron outputs on muscles, the particular choice of $h$ is irrelevant to this work and will therefore be left arbitrary. We indicate a specific threshold in order to maintain consistency when calculating active phase durations.

"Swim stimulation" corresponds to a fixed set of drives $\{I_{u_k}\}$ that induces a model to generate the swim rhythm. "Scratch stimulation" is analogous but with $\{I_{u_k}\}$ taking different values than in the swim case. If a neuron does not participate in a particular rhythm, it receives a constant value $I_{u_k} = 0$ and is inactive. The drive a neuron receives during "dual stimulation" is chosen to be the sum of the drives it receives during the scratch and swim rhythms. In some simulations, the strength of the swim stimulation is altered by

15

multiplying all swim stimulation parameters by a factor $\alpha$, the default value of which was 1 (see Table 2). "Subthreshold swim stimulation" refers to a reduced swim drive ($\alpha < 1$), which results in either below threshold or tonic (above threshold for the full duration) input to the motoneurons, both of which are seen experimentally. We refer to the stimulation given in either of those cases as "subswim." We will see in later sections that the ability of one of our models to support Benchmark 4 relies on the output of the swim module under this reduced stimulation, even though swim stimulation is subthreshold (for this work, we chose threshold at $\theta_{th} = 0.6$).

When $\tau$ is large, neurons described by equation (2.1) have dynamics that operate on different time scales. This system is referred to as a fast-slow system, since $a_{u_k}$ evolves more slowly than $u_k$ except where $|f_T|$ is small. In this type of system, examining the curves where the right hand side of equation (2.1) equal zero is particularly helpful in understanding the neuronal dynamics. These curves are called nullclines. From equation (2.2), the $a_{u_k}$-nullcline satisfies $u_k = -a_{u_k}$ and the $u_k$-nullcline satisfies $u_k = f_T(\alpha I_{u_k} - \sum_{u_j \neq u_k} b_{u_k u_j} u_j - g a_{u_k})$. Notice that the calculation of the $u_k$-nullcline depends on the choice of drive and on continuous inhibition from other neurons in the system. Thus, this nullcline shifts in phase space over time as the neurons interact. See Figure 4 for an example. In this system, $a'_{u_k} < 0$ for points in phase space above the $a_{u_k}$ nullcline and $a'_{u_k} > 0$ below it. Similarly, $u'_k < 0$ above the $u_k$-nullcline, and $u'_k > 0$ below the $u_k$-nullcline, as indicated with arrows in Figure 4 for the inhibited nullcline. A formal discussion of fast-slow dynamics can be found in Section 3.2.1 (presented for a different neuron model). We note here that due to the different timescales, the neurons in this system track their $u_k$-nullcline, moving up or down as directed by the vector field, until decreased/increased inhibition sufficiently shifts their nullclines and causes the neurons to cross threshold.

To illustrate how dominance switches occur between neurons described by equation (2.1), consider a symmetric 2-cell model (where both neurons receive the same constant drive and inhibit each other equally). Assume $u_1$ starts in the silent state (below threshold) at the point indicated with a red star on the inhibited nullcline in Figure 4 and $u_2$ is initialized in the active state (above threshold) indicated with a red dot on the uninhibited nullcline in Figure 4. As $u_1$ travels down the $u_1$-nullcline, its activity level increases, which decreases
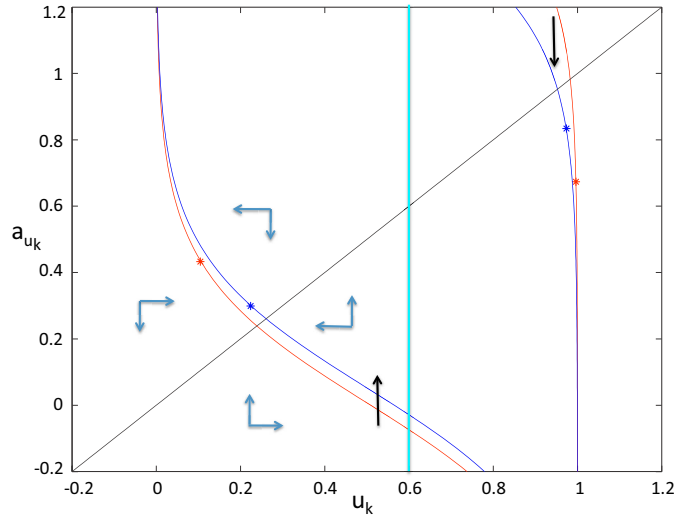
**Figure 4:** *Movement of nullclines in $(u_k, a_{u_k})$ phase space during an oscillation as time progresses. Timepoints are indicated with colored stars that correspond to their relevant $u_k$-nullclines (red indicates the first time point, blue the second time point). Threshold is indicated in cyan. As the activity level of the inhibited neuron increases, it provides stronger inhibition to the free neuron, which shifts the uninhibited nullcline down in phase space. Similarly, as the activity level of the free neuron decreases, it provides less inhibition to the inhibited neuron, which shifts the inhibited nullcline up in phase space. The direction in which the nullclines shift are indicated with black arrows. The vector field for the inhibited configuration is indicated with blue arrows.*

the overall total input to $u_2$ in equation (2.1). This shifts the $u_2$-nullcline down (indicated with an arrow), causing $u_2$'s activity level to decrease. A decrease in $u_2$'s activity level corresponds to an increase in the total input level to neuron $u_1$, which raises the $u_1$-nullcline and promotes further increases in $u_1$'s activity level. These nullclines continue to shift until one of the neurons reaches the steep part of its nullcline (note the sigmoidal shape of $f$ in equation (2.2)), where small changes in the slow variable $a_{u_k}$ corresponds to large changes in the activity level $u_k$. This has a significant effect on the inhibition the neuron provides to its partner cell, which promotes a large shift in the partner cell's nullcline. The inhibited nullcline shifts up rapidly until its critical point lies to the right of threshold, and the free nullcline shifts down until its critical point lies below threshold, and the neurons track this activity, jumping between states.

Transitions between neurons have been classified previously [19, 71, 79] by the "escape" and "release" mechanisms. The escape mechanism occurs when the silent cell is able to

overcome the inhibition it receives and enter the active phase. The release mechanism occurs when the active cell controls the switch by shutting down and releasing the inhibited cell. In this model, dominance switches are triggered by the escape mechanism, when the suppressed population exhibits a significant increase in its response to a small change in total input. Conversely, the release mechanism occurs when the response to a small change in total input to the active population is significant. This response can be seen from the shape of the neuron's $f_T$ function, since this is directly related to the neuron's activity level. Consider the location of nullclines in phase space under constant levels of inhibition for two different drives in Figure 5. Under large drive choices (Figure 5A), nullclines are shifted far up in phase space, so small changes in inhibition significantly affect a silent neuron (see the position change between the pink and blue curves in that figure). Equivalent changes in inhibition to an active neuron (red and green curves) have little effect on the nullcline shape (which remains close to constant for all $a_k$). When a neuronal network exhibits nullclines in this configuration, oscillations occur via escape, since the suppressed population (and not the active population) has a large response to changes in total input.

When drive is smaller (Figure 5B), nullclines are shifted far down in phase space, where small changes in inhibition have little effect on a neuron in the silent configuration (see the shallow shapes of the blue and magenta curves). Conversely, it is now the active cell that has a significant response to changes in inhibition (note the drastic shift in the uninhibited red and green nullclines in Figure 5B). A network generating nullclines in this configuration produces transitions via the release mechanism.

When transitions occur via escape, drive increases cause an increase in oscillation frequency. Increasing the drive, or shifting the nullclines up in Figure 5A, has little effect on the active nullclines, but would allow a silent neuron to reach the sloped regime of its nullcline more easily, which promotes a faster transition. In the next section, we will discuss the choice of constant drives, time constants, and connections between neurons that we prescribed for the three configurations in our preliminary modeling, which were chosen so that oscillations occurred by escape transitions in order to meet one of the benchmarks.

18
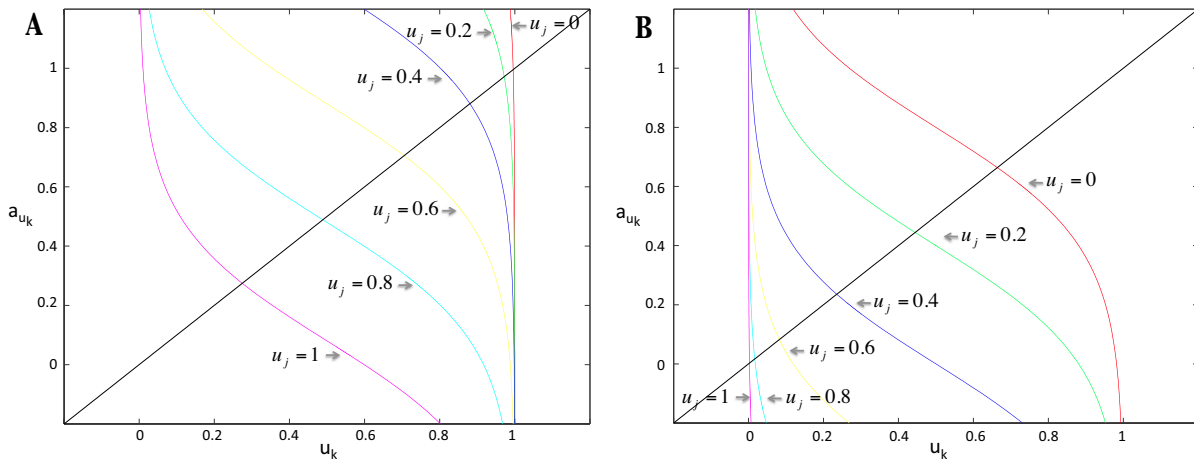
**Figure 5:** *Nullcline configuration in $(u_k, a_{u_k})$ phase space under constant levels of inhibition. (A) Alignment for large drive ($I_{u_k} = 1.25$). Inhibited nullclines (pink, blue) show a larger response to small changes in inhibition ($u_j$) than free nullclines (green, red), which remain shallow and close to 1 for almost all values of $a_{u_k}$. (B) Alignment for small drive ($I_{u_k} = 0.60$). Free nullclines show a larger response to small changes in inhibition than inhibited nullclines, which remain shallow and close to 0 for almost all values of $a_{u_k}$.*

## 2.3   INITIAL INVESTIGATION OF MODELS' ABILITY TO SUPPORT EXPERIMENTAL BENCHMARKS

In [32], we published specifically tuned parameters that could produce forward swim and caudal scratch rhythms in response to corresponding levels of constant stimulation for each of the different model structures. These parameter choices are indicated in Tables 2-4, and an example of the model output for one of the structures is in Figure 6.   We first considered the DCPG model which included two separate rhythmogenic modules that sent signals to common motoneuron targets but did not interact directly (see Figure 3C). By systematic exploration of relevant regions of parameter space, parameters were found that yielded the forward swim and caudal scratch rhythms separately (Benchmark 1), but for any such parameter set, this model was unable to reproduce the experimental responses to dual stimulation that we explored (Benchmarks 3-4). Specifically, when subthreshold swim plus scratch

19

| Postsynaptic neurons | Inhibition strengths from presynaptic neurons | | | | | | Current Injected | | |
| --- | --- | --- | --- | --- | --- | --- | --- | --- | --- |
| | $ke_1$ | $hf_1$ | $he_1$ | $ke_2$ | $hf_2$ | $he_2$ | $I_{swim}$ | $I_{scratch}$ | $\tau_k(ms)$ |
| $ke_1$ | 0.00 | 0.00 | 0.95 | 0.75 | 0.75 | 0.75 | $\{1.16^*,1.18\dagger\}\alpha$ | 0.00 | 1000 |
| $hf_1$ | 0.00 | 0.00 | 0.95 | 0.75 | 0.75 | 0.75 | $\{1.15^*,1.17\dagger\}\alpha$ | 0.00 | 1000 |
| $he_1$ | 0.50 | 0.50 | 0.00 | 0.75 | 0.75 | 0.75 | $1.24\alpha$ | 0.00 | 1000 |
| $ke_2$ | 0.64 | 0.64 | 0.64 | 0.00 | 0.85 | 0.75 | 0.00 | 0.74 | 1000 |
| $hf_2$ | 0.64 | 0.64 | 0.64 | 0.75 | 0.00 | 0.85 | 0.00 | 0.79 | 1500 |
| $he_2$ | 0.64 | 0.64 | 0.64 | 0.85 | 0.75 | 0.00 | 0.00 | 0.84 | 2000 |

**Table 2:** *Linked central pattern generator (LCPG) model parameter values. Each row gives values associated with a particular neuron, the identity of which is indicated in the leftmost column (see Figure 3 for notation). The constant $\alpha$ takes the value 1 for baseline rhythm-generating stimulation, is increased from 1 to represent stronger stimulation, and is decreased sufficiently far from 1 to effect subthreshold stimulation. ke, knee extensor interneuron; hf, hip flexor interneuron; he, hip extensor interneuron; $I_{swim}$, input inducing a swim rhythm; $I_{scratch}$, input inducing a scratch rhythm; $\tau_k$, time constant. \*Parameters giving a tonic subswim regime for reduced $\alpha$. †Parameters giving a subthreshold subswim output for reduced $\alpha$.*

| Postsynaptic neurons | Inhibition strengths from presynaptic neurons | | | | | | Current Injected | | |
| --- | --- | --- | --- | --- | --- | --- | --- | --- | --- |
| | $ke_1$ | $hf_1$ | $he_1$ | $i_1$ | $i_2$ | $i_3$ | $I_{swim}$ | $I_{scratch}$ | $\tau_k(ms)$ |
| $ke_1$ | 0.00 | 0.20 | 1.07 | -0.80 | 0.90 | 0.00 | $1.41\alpha$ | 0.32 | 1000 |
| $hf_1$ | 0.20 | 0.00 | 1.07 | 0.50 | -0.45 | 0.00 | $1.42\alpha$ | 0.30 | 1000 |
| $he_1$ | 0.62 | 0.62 | 0.00 | 0.00 | 0.40 | -0.60 | $1.40\alpha$ | 0.32 | 1500 |
| $i_1$ | 0.30 | 0.87 | 0.60 | 0.00 | 0.00 | 0.00 | 0.00 | 0.70 | 2000 |
| $i_2$ | 0.60 | 0.20 | 0.85 | 0.00 | 0.00 | 0.00 | 0.00 | 0.71 | 2500 |
| $i_3$ | 0.80 | 0.80 | 0.30 | 0.00 | 0.00 | 0.00 | 0.00 | 0.63 | 2500 |

**Table 3:** *Unitary CPG (UCPG) model parameters that give a tonic output when $\alpha$ is reduced. Format and notation are as in Table 2. $i_1$, $i_2$, $i_3$ are additional interneurons.*

| Postsynaptic neurons | Inhibition strengths from presynaptic neurons | | | | | | Current Injected | | |
| --- | --- | --- | --- | --- | --- | --- | --- | --- | --- |
| | $ke_1$ | $hf_1$ | $he_1$ | $i_1$ | $i_2$ | $i_3$ | $I_{swim}$ | $I_{scratch}$ | $\tau_k(ms)$ |
| $ke_1$ | 0.00 | 0.30 | 0.85 | -0.50 | 0.90 | 0.00 | $1.01\alpha$ | 0.52 | 1000 |
| $hf_1$ | 0.30 | 0.00 | 0.9 | 0.50 | -0.30 | 0.00 | $1.05\alpha$ | 0.45 | 1000 |
| $he_1$ | 0.60 | 0.60 | 0.00 | 0.00 | 0.25 | -0.30 | $1.10\alpha$ | 0.50 | 1000 |
| $i_1$ | 0.30 | 0.87 | 0.60 | 0.00 | 0.00 | 0.00 | 0.00 | 0.45 | 2000 |
| $i_2$ | 0.60 | 0.20 | 0.85 | 0.00 | 0.00 | 0.00 | 0.00 | 0.40 | 2500 |
| $i_3$ | 0.80 | 0.80 | 0.30 | 0.00 | 0.00 | 0.00 | 0.00 | 0.75 | 2500 |

**Table 4:** *UCPG model parameters that give a subthreshold output when $\alpha$ is reduced. Format and notation are as in Tables 2-3.*

stimulation was provided, a swim rhythm could not be obtained. With this form of dual stimulation, the input to each motoneuron was above threshold during the time intervals corresponding to its scratch activity, and these intervals could become prolonged but could not be converted to a swim rhythm. For some parameter choices, subthreshold swim stimulation could yield tonic activity in one or more motoneurons, as seen experimentally in some cases; in the resulting dual stimulation simulations, these motoneurons remained tonically active as well. With full swim and scratch dual stimulation, we found it difficult to produce any rhythm at all and could never produce a faster swim rhythm as seen experimentally; since the swim-producing module continued to produce a normal-frequency swim rhythm under this stronger form of dual stimulation, motoneuron activation at this frequency was maintained. Since the simple mechanisms underlying these failures represent characteristics of the DCPG network structure, not specific to any particular parameter choices, we concluded that a network without direct interactions among rhythmogenic modules is unlikely to produce our experimental results.

We next proceeded to simulate two alternative models, one with separate rhythmogenic modules linked by reciprocal inhibition (LCPG) and one with a single (unitary) network of cells that collaborate to produce both rhythms (UCPG) (see Figure 3). Both the LCPG and UCPG models, each with fixed connection strengths, were able to produce rhythms corresponding to caudal scratch and swim for particular choices of stimulation constants (Tables 2-4, see Figure 6 for an example).
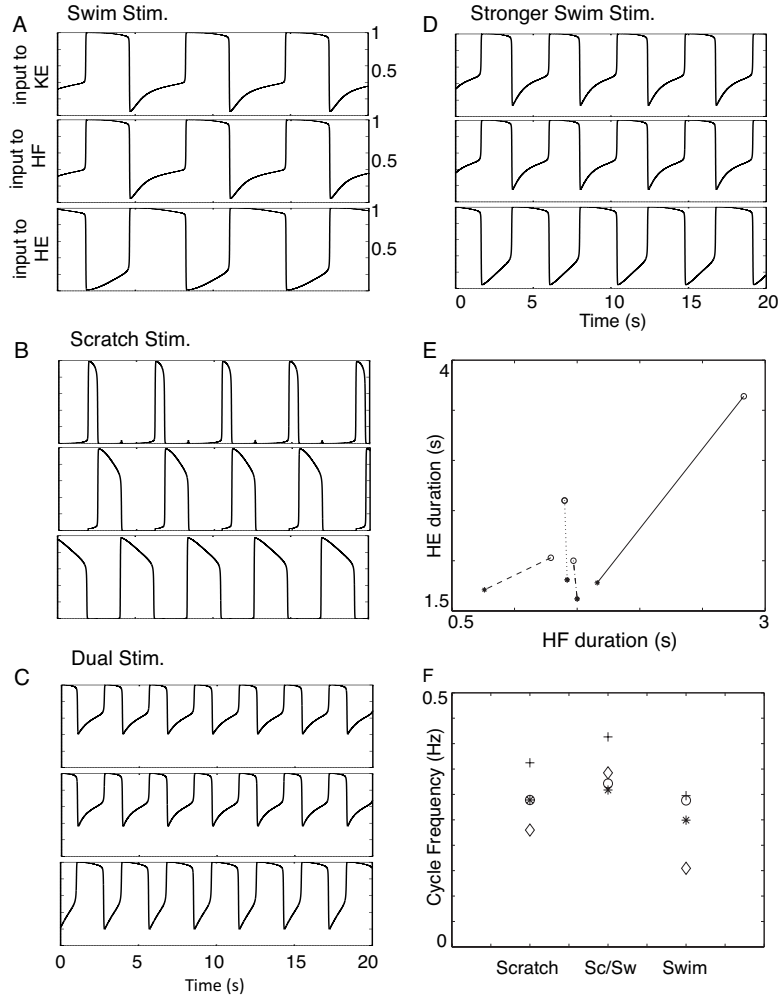
**Figure 6:** *Model simulations of rhythms. A-D: rhythms generated by the UCPG model (specifically, summed inputs to each motoneuron) with swim stimulation (A), scratch stimulation (B), dual stimulation (C), and stronger swim stimulation (D, $\alpha = 1.1$). In each panel, the top trace is the time course of input to the KE motoneuron, $\sum ke_k$, the middle trace is the input to the HF motoneuron, $\sum hf_k$, and the bottom trace is the input to the HE motoneuron $\sum he_k$. E: HE duration is plotted against HF duration for the swim (open circle) and dual stimulation (asterisk) rhythms for each of the models. Two parameter sets were chosen for each model (UCPG, solid and dashes segments; LCPG, dash-dotted and dotted segments). The swim and dual stimulation swim rhythms for each parameter set are connected with a line segment. F: rhythm frequencies for different parameter sets in the LCPG and UCPG models. Frequencies from the LinkedT set are denoted with circles; LinkedS frequencies are denoted with asterisks. Frequencies produced by the UnitaryT set are denoted with diamonds; UnitaryS frequencies are denoted with plus signs.*

During the swim rhythm, the activity of $KE$ and $HF$ are in phase, out of phase with $HE$. A general feature that we found was that to obtain an increase in swim frequency with stronger swim stimulation, the dominance switch between $ke/hf$ and $he$ had to operate via the escape mechanism (for more details, see the discussion in the previous section and [19, 71, 79]). The escape mechanism arises in our models when neurons receive near-saturation levels of total input while active, such that increasing the stimulus strength has little effect on active neurons but allows inhibited neurons to activate more easily, resulting in a rhythm with higher frequency (Figure 6D; see also [19]). Thus, we tuned both models to operate in the escape regime. See an example of the nullcline configuration in the $ke$ and $he$ phase spaces for dynamics generated under the parameter set indicated in Table 4 in Figure 7.

Under this tuning, during full dual stimulation, which activated all CPG neurons and thus evoked all associated interactions, both the LCPG and UCPG structures were able to produce a faster swim rhythm. Examples of this frequency increase for two parameter choices for each model are shown in Figure 6F. Interestingly, in the LCPG model, dual stimulation increased HF duration very slightly, in contrast to experimental results, whereas in the UCPG model, dual stimulation caused both HE and HF durations to decrease relative to normal swim (Figure 6E). Furthermore, dual stimulation applied in experiments elicited accelerated rhythms, and we found that dual stimulation in the UCPG model yielded a larger frequency increase than occurred with dual stimulation in the LCPG model. Although we have not fully explored all possible parameter choices in our models, these results describing changes in phase durations and overall rhythm frequency with dual stimulation represent evidence in favor of the UCPG model over the LCPG model.

A stronger argument in favor of the UCPG model emerged from our simulations combining subswim plus full scratch stimulation. Experimentally, subthreshold swim stimulation could lead either to all motoneurons remaining below threshold or to some motoneurons firing tonically [32]. We found two parameter sets that represent these dynamics for each of the LCPG and UCPG models. Both parameter sets elicited escape-based swim rhythms for each model at full swim stimulation ($\alpha = 1$). For one set, when the swim stimulation was maintained but its amplitude reduced (to an $\alpha < 1$ in the equations for all neurons), the swim rhythm was lost, but at least one motoneuron exhibited tonic activity (i.e., at
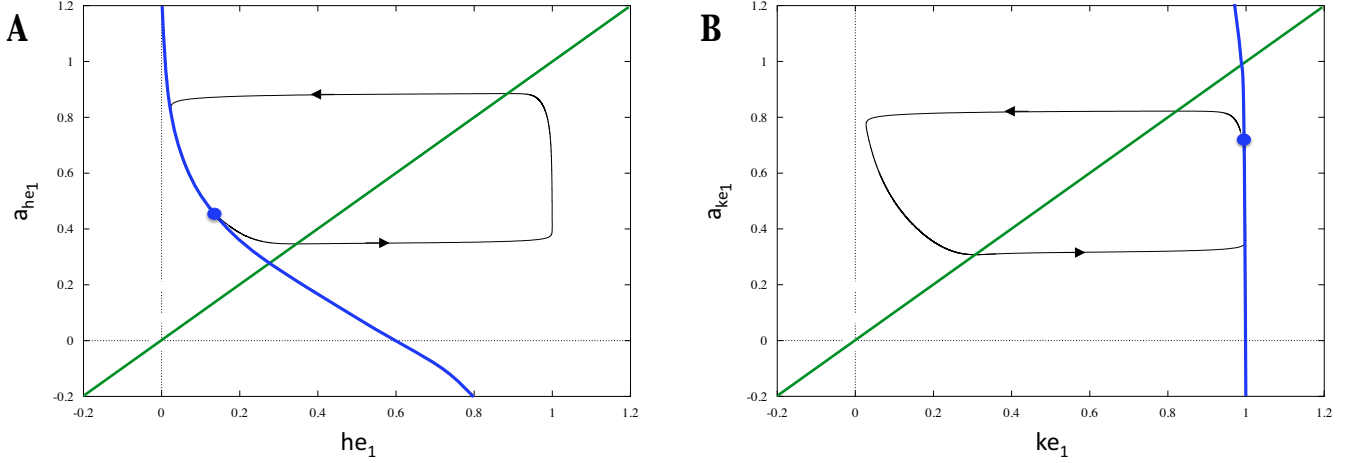
**Figure 7:** *Relevant curves in $he_1$ and $ke_1$ phase space under swim stimulation ($hf_1$ omitted for brevity since it displays similar dynamics to $ke_1$). From equation ([2.1](#)), the $a_{u_k}$-nullcline satisfies $a_{u_k} = u_k$ (shown in green), and the $u_k$-nullcline satisfies $a_{u_k} = (1/g)(\alpha I_{u_k} - \sum_{k \neq j} b_{u_k u_j} u_j - f_T^{-1}(u_k))$ (plotted in blue and calculated at the values of $(u_k, a_{u_k})$ indicated with blue dots), where $u_k \in \{ke_1, hf_1, he_1\}$. The solution trajectory is shown in black, with arrows indicating forward time. The $u_k$-nullclines shift up or down with changes in activity of other neurons. As the activity level of $he_1$ increases in (A), the $ke_1$-nullcline in (B) shifts down in phase space. Similarly, as the activity level of $ke_1$ decreases in (B), the $he_1$-nullcline in (A) shifts up in phase space. In the inhibited state, neurons move along the "sloped" part of the $u_k$-nullcline (as in A). In the active state, neurons move along the "shallow" part of the $u_k$-nullcline, where it is relatively constant (as in B). These nullclines have been configured so that the switch in dominance occurs due to a significant variation in the activity level of the suppressed neuron, which "escapes" from the inhibited state and forces the active neuron into the silent phase.*
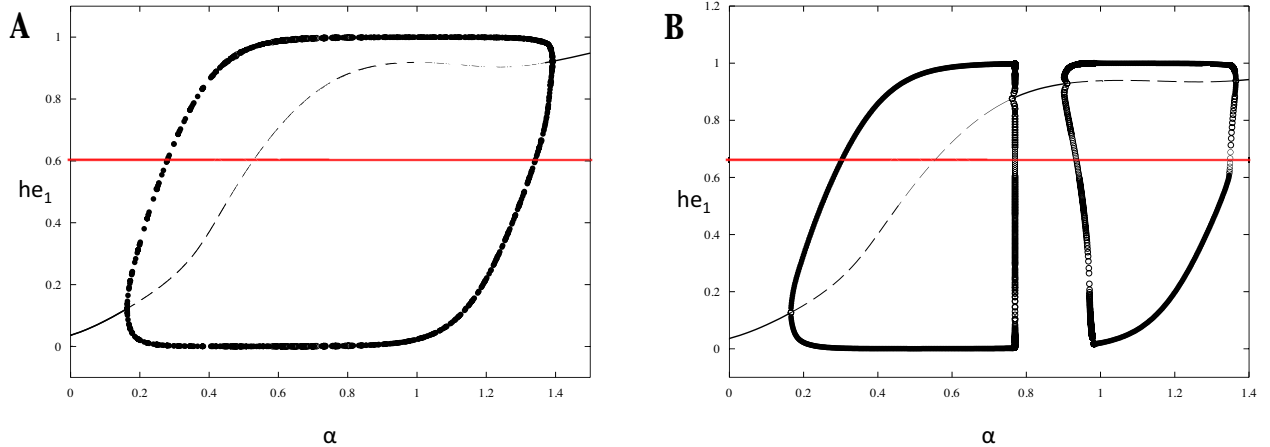
**Figure 8:** *Bifurcation diagrams for the activity level of $he_1$ against the swim stimulation strength $\alpha$ for parameter choices in the linked CPG configuration. Threshold ($\theta_{th} = 0.6$) is denoted with a red line. (A) The dynamics exhibited under the LinkedS parameter set yields oscillatory behavior as $\alpha$ is lowered until the oscillation amplitude decreases below threshold. (B) The dynamics under the LinkedT set exhibit a regime of steady state activity as the swim stimulus strength is lowered. As $\alpha$ is decreased from 1, the oscillations lose stability (we expect a complicated cascade of dynamics, see [16, 17]) until the system exhibits tonic activity near $\alpha = 0.9$.*

least one member of the CPG provided input to a motoneuron that was above the threshold $\theta$). We denoted these sets as the UnitaryT and LinkedT sets, corresponding to the unified and linked structures, respectively, where "T" indicates tonic activity. For the other set, a swim-like rhythm was preserved as swim stimulation amplitude was reduced ($\alpha < 1$) but eventually, for small enough $\alpha$, only subthreshold signals to the motoneurons were produced and hence no motoneuron activation occurred (see the description of $KE$, $HF$, and $HE$ in the previous section). We denoted these as the UnitaryS and LinkedS sets, where "S" corresponds to subthreshold activity. Using XPP, we generated the bifurcation diagrams for the two parameter sets in the LCPG configuration, see Figure 8. Notice that the LinkedT and LinkedS parameter sets differ only in the strength of the swim drive values to $ke_1$ and $hf_1$ (see Table 2), yet the dynamics produced by these sets were vastly different as the swim stimulus strength ($\alpha$) varied. In Figure 8A, stable oscillations were exhibited for a wide range of $\alpha$, continuing past the point when the amplitude of the oscillations were below threshold. In Figure 8B, however, oscillatory behavior was interrupted as $\alpha$ decreased, and $he_1$ exhibited tonic activity at a value of stimulus strength less than, but close to 1.

25

To obtain the regime of tonic activity, we slightly lowered the drive strength to both $ke_1$ and $hf_1$ (represented by $\beta$). Decreasing $\beta$ to a value less than 1 prevented those neurons from escaping, and $he_1$ was unable to release. Choosing parameters that strike a balance of inhibition that promotes these dynamics between neurons can be challenging because the neurons are directly connected, and thus every change in the activity level of a neuron updates the activity level of other cells in the network (see the discussion in the previous section). In some cases, we found it difficult to generate parameters where the three neurons had settled at stable steady states (where one or more of the neurons were above threshold) as the stimulus strength was decreased – oscillatory behavior often persisted as transitions via an escape mechanism were replaced by transitions via release as $\alpha$ was reduced, as in Figure 8A. Whether a parameter set generated steady state activity as the escape strength was decreased could be revealed on a two parameter bifurcation diagram. Using XPPAUT, we determined the locations of the Hopf bifurcations as the swim stimulation strength and the strength to $ke/hf$ varied, shown in Figure 9. For completeness, we present the entire trace in Figure 9A, but we zoom in on the relevant regime in Figure 9B. Inside this curve, parameters generated oscillatory behavior in the network, and outside of this curve, the network exhibited steady state activity. Indicated with a red line is the choice of $\beta$ for the LinkedS parameter set. We slightly decreased this strength for the LinkedT set, the value of which is represented with a blue line. Notice that the blue line intersects the Hopf curve at four distinct points, and the red line only two, indicating that the LinkedS set will have interrupted oscillations within that entire range of stimulus strength, but the LinkedT parameters will yield a brief region of tonic activity. By altering $\beta$, we can control the width of the respective oscillatory and tonic regimes with respect to swim stimulus strength, if we wish. However, as we indicated previously, not all parameter choices yield steady state activity as the stimulus strength is lowered (and hence, produce a two parameter bifurcation with this "bow tie" shape). The UnitaryS set produced a two parameter bifurcation diagram where no change in $\beta$ would result in a four Hopf intersection (see Figure 10). Looking at the dynamics in this space encouraged us to abandon attempts to modify the UnitaryS parameters to obtain a regime of tonic activity, as we did in the LCPG case. Instead, we sufficiently varied other parameters and analyzed the two parameter bifurcation diagrams
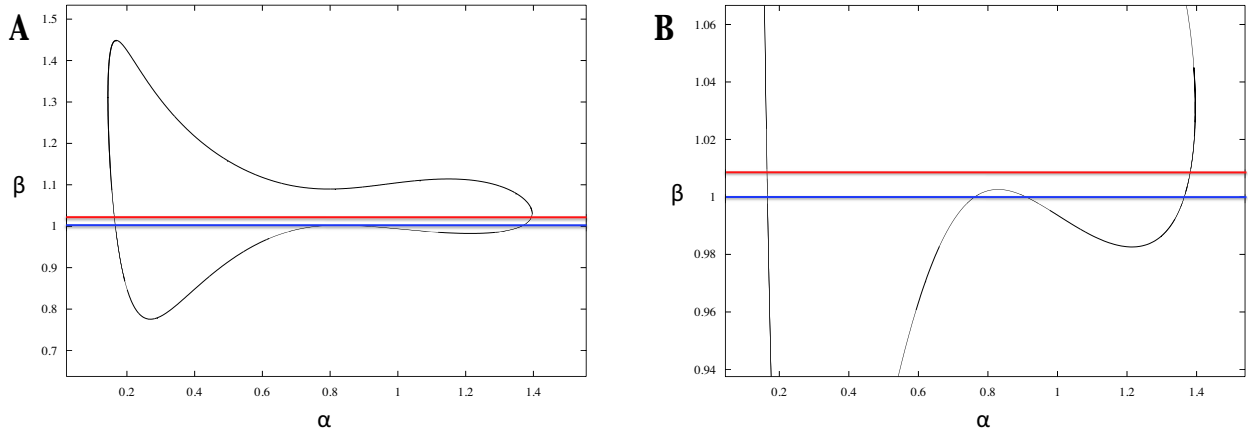
**Figure 9:** *Two parameter Hopf bifurcation diagrams of strength of input to $ke_1$ and $hf_1$ ($\beta$) against the overall swim stimulation strength ($\alpha$, which controls the strength of drive to all of the neurons) are plotted in black. The LinkedT $\beta$ value is indicated in blue and the LinkedS $\beta$ value in red. The entire Hopf curve is shown in (A), but zoomed into the relevant area in (B) to highlight that the LinkedT parameter set yields four Hopf bifurcations as $\alpha$ is varied, and the LinkedS choice yields only two.*

in each case until the shape of the Hopf curve indicated such a regime was attainable. We note that the UnitaryT parameter set yielded bistability between a steady state with $he_1$ tonic and $ke_1/hf_1$ silent and another with $he_1$ silent and $ke_1/hf_1$ tonic. When paired with scratch, both gave the same input to motoneurons.

When subthreshold swim stimulation produced tonic activity of at least one motoneuron and was applied with a full scratch stimulus, a swim-like rhythm in both models was evoked (UCPG dynamics shown in Figure 11A, LCPG dynamics shown in Figure 11C). This was not the case when subthreshold swim stimulation meant below-threshold inputs to motoneurons, however. To maintain uniformity, we chose the value of $\alpha$ so that the model produced the largest possible subthreshold motoneuron input (i.e., total input to at least one motoneuron was exactly at threshold, see Figure 11) in each of the models. When this stimulus was paired with a full scratch, the UCPG was able to generate a swim-like rhythm (Figure 11B). The LCPG model could not (Figure 11D). Although the output of the swim CPG neurons was below threshold, this module could still impact the scratch CPG through the inhibition be-
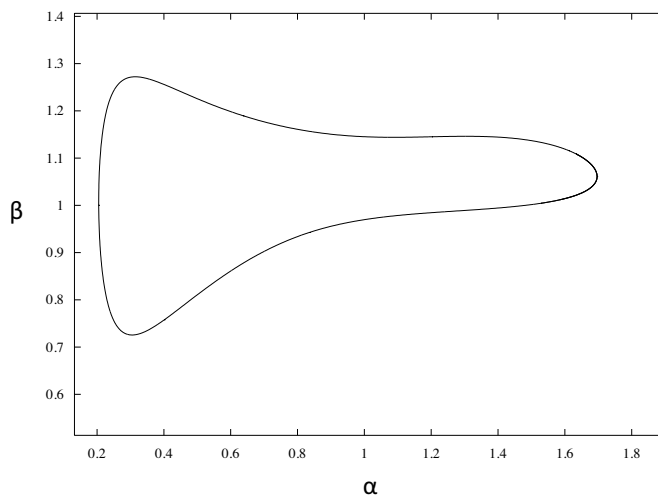
**Figure 10:** *Two parameter Hopf bifurcation diagram of the strength of input to ke/hf against swim stimulation strength for dynamics generated by the UnitaryS parameter set. Unlike in Figure 9, changing the strength of the input to ke and hf would not cause the model to exhibit a regime of steady state activity, due to the shape of the Hopf curve (a horizontal line drawn at any value of β intersects the curve in at most two points).*

tween the two CPG components. However, the inhibition within the scratch component was already strong enough to prevent co-activation of multiple neurons, and thus the additional weak inhibition from the subthreshold swim activity could not induce simultaneous firing of the $KE$- and $HF$-driving neurons, as needed for the swim rhythm to arise. Instead, a below-threshold swim stimulus together with a scratch input yielded a scratch rhythm, similar to that observed in the DCPG model under these stimulation conditions (Figure 11D). As in the DCPG case, this outcome appears to be a general property of the LCPG model, illustrating that, despite their nonlinearity, the segregated nature of the rhythmogenic circuits within this model prevents additional inhibition from subthreshold swim stimulation from overcoming the intrinsic tendency of the scratch CPG to generate scratch rhythms, in contrast to our experimental observations. These preliminary results favor the UCPG structure as the most likely to underlie the experimental results produced by our collaborators, a conclusion that was published in [32]. For the rest of this chapter, we will further investigate the capabilities of these two models by generating additional parameter sets able to support the benchmarks and compare the results from those sets with the preliminary
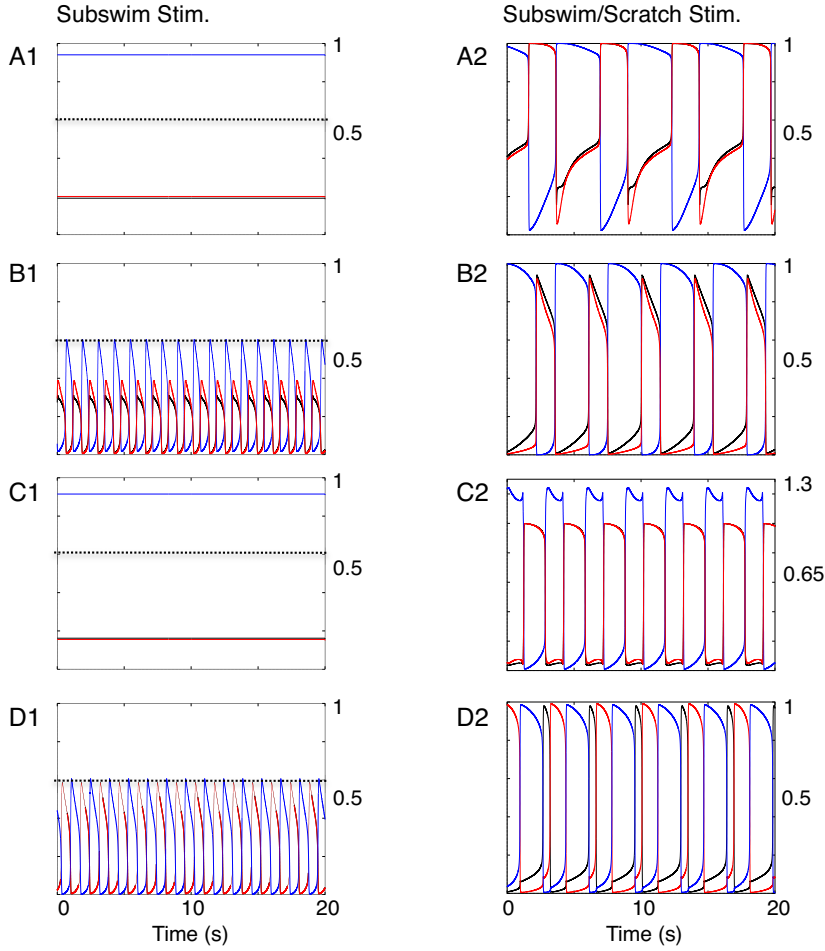
**Figure 11:** *Simulation results for subthreshold swim stimulation applied with scratch stimulation for 4 different parameter sets. The left column shows the inputs to the motoneurons for the subswim cases considered; black, red, and blue solid traces denote inputs $KE$, $HF$, and $HE$, respectively, and black dashed lines denote the motoneuron activation threshold, $\theta_{th} = 0.6$. Each case is paired with corresponding scratch stimulation, and the resultant inputs to the motoneurons are shown at right. A and B: UCPG model, C and D: LCPG model. A1 and C1: parameters were chosen ($\alpha = 0.85$) so that tonic activity in one motoneuron results when swim stimulation is lowered sufficiently. B1 and D1: the swim rhythm persists with decreasing amplitude, as swim stimulation is lowered until output is below threshold (B1, $\alpha = 0.3$, D1, $\alpha = 0.28$). The UCPG is able to produce a swim rhythm regardless of the type of subswim stimulation used (A2 and B2). The LCPG yields a swim rhythm when subswim includes tonic activity (C2) but exhibits scratch when parameter choices produce below-threshold activity in the swim module (D2).*

work we outlined above. In the next section we describe the numerical methods we used to generate parameter sets and evaluate the models' performance under these sets.

## 2.4 ALGORITHMS FOR GENERATING PARAMETER SETS AND ANALYZING MODEL RESULTS

As we discussed in the previous section, parameter sets for both the UCPG and LCPG models were found that fully supported Benchmarks 1-3. The final benchmark, regarding the output of the model under subthreshold swim plus scratch stimulation, differentiated the models. The LCPG was able to produce a swim rhythm (and hence, satisfy Benchmark 4) only when subswim produced tonic activity. The UCPG could match the benchmark when reduced swim stimulation produced either tonic activity or below threshold firing in the swim component. This result favored the unified structure as the architecture that best matched the dual stimulation experimental results. In addition, slight increases in $HF$ duration under dual stimulation in the LCPG configuration contrasted with experimental results, further indicating that the UCPG would be more likely to produce the results seen experimentally.

We wish to test the validity of that conclusion by generating collections of parameter sets for the UCPG and the LCPG structures that are able to satisfy the benchmark conditions. Since a 3-neuron network in both models generates swim, we will begin by producing 3-cell networks comprised of neurons described by equation (2.1) with randomly generated connection strengths, drive values, and time constants. Parameter sets able to generate either the scratch or swim pattern will be retained and used in later sections to form the foundation upon which we will build our UCPG and LCPG structures. In this section we will discuss the process we used for randomly generating sets for the 3-neuron network, how we determined whether the output of a network matched a swim or scratch rhythm, and how we calculated the duration of a particular rhythm. We present this discussion for the 3-neuron case, but the methods we describe extend naturally in later sections when we will discuss the generation of parameter sets for larger networks.

In the Wilson-Cowan neuronal model (equation (2.1)), each cell (population) receives a tonic drive ($I$), has a time constant associated with its slow feedback process ($\tau$), and receives and sends signals to other cells ($b$). We randomly generated these parameters (explicitly, $\{b_{ke_1 hf_1}, b_{ke_1 he_1}, b_{hf_1 ke_1}, b_{hf_1 he_1}, b_{he_1 ke_1}, b_{he_1 hf_1}, \tau_{ke_1}, \tau_{hf_1}, \tau_{he_1}, I_{ke_1}, I_{hf_1}, I_{he_1}\}$) for a 3-neuron network using a process called Latin hypercube sampling (all other parameters were

fixed at the values indicated in Section 2.2). We first designated a connection weight interval, time interval, and a drive interval within a neighborhood of the connection, time, and drive values we chose in our publication [32]. For each parameter, a *sample set* was generated by splitting its relevant interval into $n$ bins and then randomly selecting a value from each of these bins. This ensured coverage of the entire interval. We then formed a *parameter set* by randomly selecting a value for each of the parameters from their sample sets. Once a value was chosen for a particular parameter, it was removed from the parameter's sample set. We repeated this process until $n$ parameter sets were generated. We will refer to the collection of those sets as a *simulation*. See Figure 12 for an example.
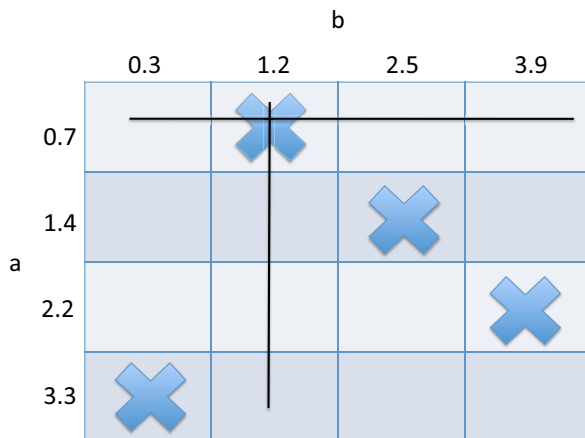


**Figure 12:** *Schematic of the LHS process on a two parameter toy example. Values for the parameters a and b are pulled from the interval* $[0, 4]$. *This interval is split into 4 bins and a value is randomly selected from each bin. In this example, a's sample set is* $\{0.7, 1.4, 2.2, 3.3\}$ *and b's sample set is* $\{0.3, 1.2, 2.5, 3.9\}$. *Once the first parameter set* $(a, b) = (0.7, 1.2)$ *is formed (pairings in the table are indicated with an "X"), those values are removed from consideration and the process is repeated. Lines indicate that in future selections, a cannot be selected from row 1 and b cannot be selected from column 2. The simulation is* $\{(0.7, 1.2), (1.4, 2.5), (2.2, 3.9), (3.3, 0.3)\}$.

Each parameter set was substituted into the 3-cell configuration and integrated in Matlab. We a priori identified neurons with those listed in Figure 3, thus, although a set might produce an output where three cells activated sequentially or two cells were out of phase with the third (as required for the scratch and swim patterns, respectively), the parameter set was not considered to have successfully generated scratch or swim unless our prescribed ordering matched the scheme described in Section 2.2. In addition, requirements on proper

duration and overlapping of the motoneurons provided more restrictions on whether a set was deemed successful. We conjecture that both of these conditions significantly reduce the number of satisfactory results obtained from random parameter generation.

The process for evaluating "successful" swimming or scratching rhythms proceeded as follows. First, the 3-cell ODE network was integrated with a particular parameter set and a transient was removed. Two preliminary conditions were checked – that the output of all neurons passed above and below the threshold, and that no neuronal output remained above threshold for longer than 90% of the time window. If the neurons passed both of these tests, we evaluated whether each one fired rhythmically. We identified the times when a neuron crossed threshold, and generated a vector comprised of the differences between those crossing times. Thus, entries in this vector indicated a neuron's active and silent durations. If the neuron was firing rhythmically, then all active durations should be equivalent to each other, and the same should be true of all of the silent durations. We checked that all of the odd entries in the vector were roughly equivalent, and did the same for the even entries. The period of each neuron could then be obtained by adding two adjacent vector entries. Since each neuron fired only once during the scratch and swim patterns, the period of each of the three neurons should be equivalent, and should equal the period of the overall rhythm. We checked to make sure the three neurons had periods with 100 ms of each other, and if this was the case, we set the rhythm period equal to the largest of these values.

If the sets satisfied the conditions above, we checked to see if they produced either the swim or scratch ordering and duration (we will omit the subscripts on $ke$, $hf$, and $he$ for this discussion) In either rhythm, $he$ must have the longest active phase – if that was the case, then we evaluated for the scratch requirements. First, we checked that $ke$ had a shorter active phase than $hf$, and that $ke$, $hf$, and $he$ fired sequentially. Next, we calculated the active overlap between each pair of neurons, and required that each pair was on together less than 30% of either of their individual active phase durations. For instance, if $ke$ was active for 1000 ms and $hf$ was active for 2000 ms; $ke$ and $hf$ could not be active together for longer than 300 ms. If the set fulfilled all of these requirements, we considered it a successful scratch. Otherwise, we evaluated the set against the swim requirements. First, we checked that $ke$ and $hf$ were active together longer than any other pair, active together more than

80% of $ke$ and $hf$'s individual active phase durations, and that the overlap between $ke$ and $he$ (and $hf$ and $he$) was less than 30% of either of their active phases. If these requirements held, the set was considered a successful swim. To check the amplified swim condition, the baseline swim input was increased by 10% and 15% (values that we considered in [32]) and the set was simulated. If the resulting rhythms were swims with faster periods than the original, then the parameter set supported Benchmark 2.

Deciding whether the dual stimulation rhythm was a success was more difficult, since it was only required to be faster than the scratch and swim rhythms, and could have a pattern that was a hybrid of the two. To evaluate the resulting dual stimulation rhythm, we implemented the first part of the process described previously, making sure the neuronal output passed above and below threshold and that the neurons were not active for longer than 90% of the time window. Next, we checked that they fired rhythmically as described earlier (where each of their active phases is the same length). We called neurons of this type *uniphasic*, meaning that they had a rhythm described by only one active duration and one silent duration. If this was not the case, we checked a second criterion, which allowed the neuron to repeat a pattern comprised of two active (and two silent) phases of different length, which permitted the neuron to fire twice within one cycle of its overall pattern. We referred to neurons of this type as *biphasic*. Sets with either of these properties were the only ones that we further evaluated for a faster rhythm under dual stimulation. We calculated the phase duration of each neuron, which was either the sum of one active plus one silent phase if the neuron was uniphasic or the sum of two active plus two silent phases if the neuron was biphasic. If the neurons were phase locked, the difference in their individual durations should be small, so we verified that that difference was less than 100 ms, and set the overall period of the pattern equal to the largest of these. At that point, we checked if the pattern had a larger frequency than either of the original scratch or swim frequency. We could also check to see if the resulting dual rhythm was a swim or scratch, using the procedure outlined earlier.

In this section, we described the method we used to randomly generated parameter sets for a 3-neuron network and how we automated the process of evaluating the network's performance. In the next section, we will discuss the implementation of the techniques we

have just described and indicate the successful parameter sets we obtained that generate swim or scratch in a 3-neuron network.

## 2.5   CLASSIFYING SETS THAT GENERATE FAVORABLE 3-NEURON NETWORK DYNAMICS

Now that we have introduced methods for producing parameter sets and composed algorithms for evaluating network output, we can test the performance of a 3-cell network for its ability to produce swim or scratch. A parameter set for a 3-neuron network is comprised of 12 parameters – six interconnectivity weights, three drive parameters, and three time constants. We chose sample sets for the six connection weights from the interval [0, 1], sample sets for the three drive parameters from [0.5, 1.5], and sample sets for the three time constants from [1000, 3000], values in a neighborhood of our published values. Running 10 simulations comprised of 10000 parameter sets each produced a total of 46 parameter sets that generated a swim rhythm with a frequency that increased as input was amplified up to 15% of the baseline. Each of these sets were tested to determine whether decreasing the swim input produced any tonic output, or if the CPG continued to oscillate until the neuron output was below threshold. None of these swims exhibited a region of tonic activity as the input was decreased. We will denote this grouping of 46 randomly generated swim parameter sets as the S collection (subswim stimulation produced subthreshold activity).

We tried clustering the S collection using the hierarchical toolbox in Matlab (pdist, linkage, and dendrogram functions), prescribing various numbers of clusters and trying both euclidean and city block metrics. We also attempted to cluster the sets using the kmeans toolbox. In either case, the clustering was poor, and we could not deduce any obvious property or mechanism that segregated the sets in various clusters. This may be because there are many different factors contributing to compensation in the total input term $I_{u_k} - \sum b_{u_k u_i} u_i$. For instance, if $I_{u_k}$ is large, then in order to suppress $u_k$ during its silent phase, $\sum b_{u_k u_i} u_i$ must be large also, but there are many ways to achieve this, namely that one or more of the $b_{u_k u_i}$ are large or one or more of the $u_i$ are saturated close to 1. Similarly, if $I_{u_k}$

is small, then in order for $u_k$ to remain active, $\sum b_{u_k u_i} u_i$ must be small as well, which can be achieved if $b_{u_k u_i}$ are all small, or if the other $u_i$ are all close to 0. If $I_k$ is some moderate value, though, then there are even fewer restrictions on parameters combinations.

Instead, we classified the sets based on a total input-based property, which we now describe. Recall that during the swim rhythm, $ke_1$ and $hf_1$ are in phase. As discussed in Section 2.3, in order for the swim rhythm to obtain a frequency increase from stimulation increases (Benchmark 2), dominance switches must occur via an escape mechanism. Unless the system was completely symmetric (that is, unless $ke_1$ and $hf_1$ had identical roles in the network), we presumed one of these neurons would be the first to activate, initiating the transition between the $he_1$ active phase and the $ke_1/hf_1$ active phase. Our classification was based on whether the parameters suggested that $ke_1$ or $hf_1$ controlled this escape mechanism. To determine this, we compared the relationship of $I_{ke_1} - b_{ke_1 he_1}$ to $I_{hf_1} - b_{hf_1 he_1}$ (see Figure 13A). If $he_1$ was large (close to 1) and $ke_1$ and $hf_1$ were small (close to 0), these two values approximated the total input to $ke_1$ and $hf_1$, respectively, during their silent phase. The larger value should indicate which neuron ($ke_1$ or $hf_1$) would reach regions where small changes in adaptation corresponded to large changes in activity level to initiate the transition process to the active phase. One cluster was comprised of sets that had $I_{hf_1} - b_{hf_1 he_1}$ greater than $I_{ke_1} - b_{ke_1 he_1} + 0.1$. Sets in this cluster should have the property that $hf_1$ controls the escape since the total input to $hf_1$ was sufficiently stronger than the total input to $ke_1$. We called this cluster the "$hf$ Dominant Cluster." Another cluster contained sets where $I_{hf_1} - b_{hf_1 he_1}$ was less than $I_{ke_1} - b_{ke_1 he_1} - 0.1$. In this cluster, the total input to $hf_1$ was sufficiently weaker than the total input to $ke_1$, so $ke_1$ should control the escape. We called this cluster the "$ke$ Dominant Cluster." The third cluster, the "Neither Dominant Cluster" was comprised of sets where $I_{hf_1} - b_{hf_1 he_1}$ was between $I_{ke_1} - b_{ke_1 he_1} - 0.1$ and $I_{ke_1} - b_{ke_1 he_1} + 0.1$. In this case, the neuron controlling the transition would be harder to distinguish.

Each of the sets were integrated to determine whether comparing these values was a good method of distinguishing which neuron was responsible for the transition. Almost all of the sets were "correctly" classified – that is, $hf$ activated first in most of the sets in the $hf$ Dominant Cluster and $ke$ activated first in most of the sets in the $ke$ Dominant Cluster. The outliers all had the property that either $b_{ke_1 hf_1}$ or $b_{hf_1 ke_1}$ was large, and thus the reduction
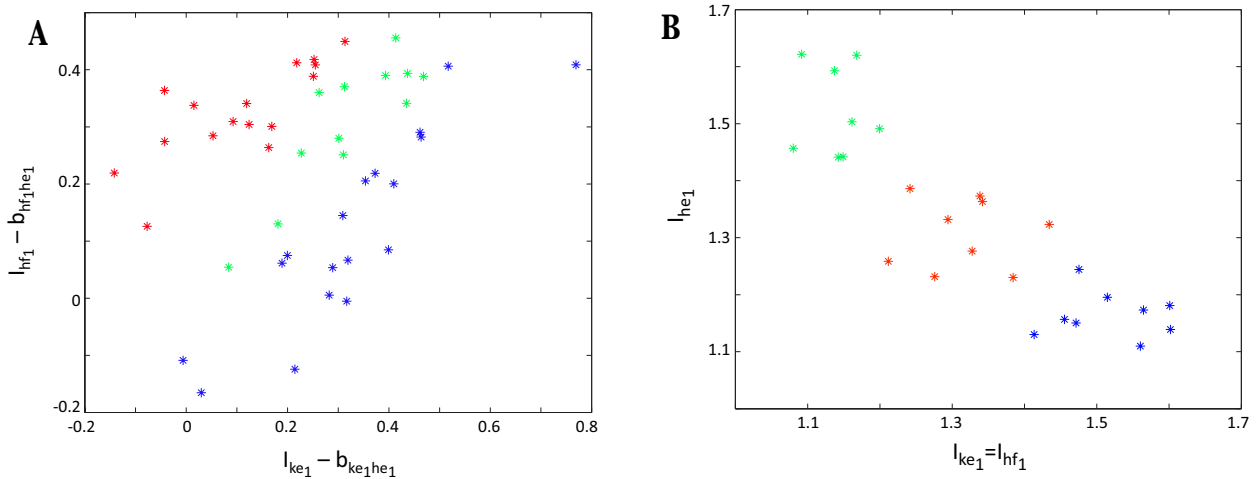
**Figure 13:** *Clustering of the 3-neuron parameter sets that generate swim. (A) The S collection is classified by comparing the total input to the in-phase neurons ($ke_1, hf_1$) when $he_1$ is near 1. The $hf_1$ Dominant Cluster is shown in red, the Neither Dominant Clusters is shown in green, and the $ke_1$ Dominant Cluster is shown in blue. (B) The T collection was clustered using hierarchical clustering methods, which formed three distinct groups, shown here on a plot of the drive to $ke_1$ and $hf_1$ against the drive to $he_1$. In those sets, $ke_1$ and $hf_1$ play identical roles in the network, so they receive the same drive value.*

was not a fair evaluation of the total input it received during that time, due to significant inhibition between $ke_1$ and $hf_1$. We attempted to use the means of each of these clusters for further study in either of the proposed structures, however, some did not satisfy the swim/amplified swim requirements. Instead, we hand selected two representatives from each cluster (choosing swims with different durations to be sure we represented the full range of possible dynamics) that we will use to produce UCPG and LCPG sets in later sections.

As we discussed in Section 2.2, for some parameter sets, escape-based oscillations were replaced by release-based oscillations as the swim stimulus was decreased. In random trials, we only found sets of this type, and were unable to generate parameter sets that produced tonic activity as the stimulus strength was decreased, despite many attempts. Since our searches proved fruitless, we employed an analytical argument to guide our search through parameter space. We simplified the swim network by assuming $ke$ and $hf$ perform identical roles in the network, which reduced the system to a 2-cell configuration. Replacing $f_T$ with

a piecewise-defined function, we composed arguments that ensured oscillations occurred via escape, and that as the stimulus strength was lowered, a tonic steady state by one of the neurons was attained. These arguments led to a collection of inequalities that we implemented to generate a tailored simulation. This produced parameter sets we denoted as the T collection, 27 sets where subswim stimulation produced tonic activity. For continuity, we delay the details of this analysis until Section 2.8.

The T collection was grouped into three clusters using the hierarchical clustering toolbox and the cityblock metric. These clusters were clearly distinguished (Figure 13). Sets in cluster 3 exhibited significantly larger drives to $he_1$ than to $ke_1$ and $hf_1$ (green dots in Figure 13). This caused compensation in other variables, namely the strengths of inhibition from $he_1$ to $ke_1$ and $hf_1$ was significantly smaller than in the other clusters, and the strength of inhibition from $ke_1$ and $hf_1$ to $he_1$ tended to be much larger in these sets than in the other clusters. Cluster 2 contained the sets where the drive to $ke_1$ and $hf_1$ was large (and the drive to $he_1$ small), and to compensate, the strength of inhibition from $he_1$ to these neurons was very large, and the strength of inhibition from these neurons to $he_1$ was the smallest (blue dots in Figure 13). Notice these clusters have opposite dynamics – in cluster 2, the dominant neurons are $ke_1$ and $hf_1$ versus $he_1$ dominant in cluster 3. Cluster 1 contained sets were the inhibition parameters and drives were somewhere in between these two extremes (red dots in Figure 13).

The simulations comprised of randomly generated parameters (described previously) were also tested to see if they satisfied the scratch rhythm conditions. However, they yielded only 5 scratch producing parameter sets. By generating sample sets for connection weights from an interval of [0.5, 1.5] (slightly stronger than the interval designated in the swim simulations) with the same number of simulations as described above, we found 48 sets capable of generating scratch. As above, these sets did not cluster nicely using any algorithms attempted. Unlike in the swim rhythm, which had constraints on the type of mechanism responsible for dominance switches, transitions in the scratch rhythm could occur due to many different mechanisms (release or escape). Thus, we did not attempt a classification of these sets (as we did with the S collection). Instead, we left this collection unclustered and hand selected four that represented a range of scratch durations to study further.

In this section, through a random search we found the S collection, sets that generated a swim rhythm and supported frequency increases as required by Benchmark 2. When the stimulus strength was lowered in these sets, network output remained oscillatory until amplitudes decreased below threshold. We clustered this collection by which of the two phase locked neurons ($ke$ or $hf$) triggered their transition to the active phase. Using a random search aided by analysis (see Section 2.8), we found the T collection, more sets that generated swim and met Benchmark 2. In these sets, tonic activity by one or more neurons was produced in the network when the stimulus strength was decreased. We clustered this collection using hierarchical clustering in Matlab. Finally, we found sets that evoked scratch, but only after searching in a regime of larger connection strengths than what we prescribed during the swim search.

While the LCPG and the UCPG have differing 6-neuron architectures, their commonality is that the activity of a 3-neuron subset alone produces swim. Thus, the swim collections we have generated in this section will form a foundation within the larger parameter sets that are required for the two models. For the LCPG structure, we will select a 3-neuron swim set and a 3-neuron scratch set and form the swim and scratch CPGs, respectively. Once we generate inhibitory connections between the two CPGs, we can immediately test that architecture for its ability to support the benchmarks regarding dual stimulation experiments. For the UCPG structure, we will designate a 3-neuron swim parameter set as the shared network and then supplement the framework with additional driver cells. Connections between the multifunctional and specialized neurons must be generated, as well as a scratch stimulus, or a set of constant drives for all 6 neurons (see Figure 3). Before we can test the dual stimulation benchmarks in that structure, we will need to find parameters that cause the 6-cell network to generate scratch. The following two sections describe this process, and its results, in detail.

## 2.6 LCPG RESULTS

Recall that the LCPG structure is comprised of a 3-cell network capable of swim linked to a 3-cell network capable of scratch (see Figure 3). In [32], we concluded that this structure was unlikely to have generated our collaborators' experimental results because it failed to support Benchmark 4 when subswim produced subthreshold firing. We conjectured that this was a general feature of the network structure and not dependent on parameter choices; that weak output from the swim CPG would be unlikely to disrupt the rhythmic activity in the scratch CPG, and thus under dual stimulation, the network would likely produce scratch. In addition, frequency increases under dual stimulation exhibited slight increases in $HF$ activity, contrary to experimental results. In this section, we test this conjecture by considering the performance of the LCPG structure using a large collection of parameter sets.

We can easily construct LCPG parameter sets by choosing a parameter set that generates swim in a 3-neuron network and another set that generates scratch in a 3-neuron network (from the previous section) and then creating connectivity between the two networks. Regardless of inter-CPG connectivity, this structure can already support Benchmark 1, since only one of the networks is stimulated during either of the rhythms. In the published sets, we minimized complexity by requiring every member from one CPG to inhibit every member in the other CPG with the same strength. We see no reason why that assumption should necessarily hold, so we generated a different sample set for each of the 18 connections between the swim and scratch CPGs over the interval [0,1] and formed parameter sets using the same Latin hypercube sampling procedure detailed previously. A simulation, in this case, consisted of 5000 parameter sets each of size 42, where 12 of the parameters comprised the connections within the swim network, 12 parameters comprised the connections within the scratch network, and 18 parameters represented interconnectivity between the CPGs.

We tested Benchmarks 3 and 4 using 12 swim sets paired with 4 scratch sets. First, the networks were simultaneously stimulated (that is, the swim network was given the swim stimulation and the scratch network was given the scratch stimulation). Those that produced a faster rhythm under dual stimulation were then tested for their ability to meet the final

benchmark, i.e. if a subthreshold swim stimulus plus full scratch stimulus yielded a swim output. In Table 5 we indicate the outcome of these experiments. In each block, the first entry corresponds to the number of pairings that resulted in LCPG output that was rhythmic with a larger frequency than either of the swim or scratch network periods alone. In almost all cases, the faster dual rhythm was either a swim or hybrid pattern (not shown). The connectivity sets that facilitated a faster dual rhythm were then further evaluated for their performance against Benchmark 4, under subswim plus scratch stimulation. In the second entry of each block, we indicate the number of connectivity sets that caused the network to produce scratch under subswim plus scratch stimulation. The third entry indicates the number of connectivity sets that caused the network to produce swim under this stimulation.

The upper half of the table exhibits results from pairing swims from the S collection with various scratches. Recall that under subswim stimulation, these sets evoked below threshold firing in the swim CPG. The lower half of the table exhibits results from pairing swims from the T collection with the same 4 scratches. In this case, the swim CPG exhibited some tonic activity as swim input was lowered. Recall that according to Benchmark 4, the desired output from subswim plus full scratch stimulation is a swim rhythm. When subswim produced below threshold firing (results from the S collection), subswim plus scratch stimulation almost always yielded scratches, and almost never a swim (in each entry L-M-N in the upper half of the table, N was almost always zero). Conversely, when subswim stimulation was defined as some tonic activity by one or more of the neurons and was paired with scratch (results from the T collection), the resulting rhythm was always swim, and never scratch (in each entry L-M-N in the lower half of the table, M was always zero) These simulations independently support the results presented in our publication, that the LCPG structure has difficulty generating a swim output under subswim plus scratch stimulation when subswim produces weak output in the swim CPG.

Pairings with particular sets produced poorer results than others, for instance, dual pairings with swim S3 produced fewer faster dual rhythms than pairings with any other swim in the S collection. Similarly, dual pairings with Scratch 3 were less likely to produce a dual rhythm with larger frequency than pairings with any other scratch. These two rhythms had the lowest and highest frequencies, respectively. These results might suggest that more

| | Scratch 1 (4325) | Scratch 2 (5376) | Scratch 3 (832) | Scratch 4 (4919) |
|---|---|---|---|---|
| **S collection** | | | | |
| *hf* Dominant Cluster | | | | |
| Swim S1 (3679) | 1549—438—0 | 1987—429—0 | 719—87—1 | 2268—889—0 |
| Swim S2 (5422) | 1234—373—0 | 1750—365—0 | 835—102—0 | 1622—639—0 |
| *ke* Dominant Cluster | | | | |
| Swim S3 (7770) | 954—376—0 | 986—289—0 | 539—73—0 | 911—449—0 |
| Swim S4 (6009) | 1545—442—0 | 1784—367—0 | 955—101—0 | 2003—678—0 |
| Neither Dominant Cluster | | | | |
| Swim S5 (5594) | 1136—294—0 | 1651—332—0 | 574—53—0 | 1462—487—0 |
| Swim S6 (3000) | 1081—201—0 | 1417—160—0 | 863—75—1 | 1515—331—0 |
| **T collection** | | | | |
| Cluster 1 | | | | |
| Swim T1 (7698) | 716—0—29 | 1114—0—311 | 374—0—2 | 850—0—88 |
| Swim T2 (5314) | 840—0—33 | 2188—0—588 | 255—0—1 | 1787—0—374 |
| Cluster 2 | | | | |
| Swim T3 (5217) | 934—0—72 | 1611—0—453 | 356—0—1 | 1667—0—429 |
| Swim T4 (8389) | 594—0—9 | 577—0—11 | 567—0—0 | 679—0—3 |
| Cluster 3 | | | | |
| Swim T5 (5791) | 658—0—40 | 979—0—86 | 126—0—1 | 679—0—54 |
| Swim T6 (5617) | 727—0—71 | 1617—0—183 | 80—0—0 | 1382—0—176 |

**Table 5:** *Linked CPG dual stimulation results. The period generated by each of the swim and scratch sets is indicated next to its name in parentheses (in ms). For an entry L-M-N, L indicates how many connectivity sets (out of a possible 5000) generate a dual rhythm that has a larger frequency than either the original swim or the scratch frequency (Benchmark 3). Those sets were retained and their output under subswim plus full scratch stimulus strength was evaluated (Benchmark 4). M indicates the number that produced scratch and N indicates the number that produced swim under this stimulation. The T collection was able to support Benchmark 4. The S collection was not.*

desirable pairings result from swim and scratch rhythms with similar frequencies. In the T collection, pairings with the lowest frequency swims (T1 and T4) produced fewer faster dual rhythms than other swims, although T5 produced poor results and had a frequency in the neighborhood of the scratches we were considering. It did not appear that a particular cluster in either of these collections performed better than the others. Instead, success might be attributed more to unidentified compatible characteristics within particular pairings.

Two S collection sets paired with one of the scratch sets managed to produce a swim under subswim plus scratch stimulation. In one of these pairings, mutual inhibition caused the swim CPG to produce a below threshold scratch-like output that summed with the scratch-like output from the scratch CPG to project a swim output to the motoneurons. In another pairing, the swim CPG produced below threshold anti-phase oscillations of $ke_1$ and $hf_1$, with $he_1$ completely suppressed. The scratch CPG in that case continued to produce a scratch-like rhythm, and the timing was aligned so that $hf_1$ bursts from the swim CPG occurred early in the $ke_2$ phase of the scratch CPG, and $ke_1$ bursts from the swim CPG occurred late in the $hf_2$ active phase, allowing above threshold output to $KE$ and $HF$ to overlap. In both cases, strategic alignment of bursts in the the swim CPG were crucial to elongating the input to $KE$ and $HF$ so that their activation was in phase.

We compiled the 3015 successful T pairings that satisfied all of the benchmarks and looked for significant correlations between the interconnectivity parameters. Many of the parameters were highly correlated with others (with a p-value less than 0.05). Since dual stimulation was more likely to yield swim than scratch under both full and reduced swim stimuli, we assumed that the swim CPG would more strongly inhibit the scratch CPG. This was true for the means of the inhibition parameters – inhibition from members of the swim CPG to members of the scratch CPG was larger than the means of the parameters in the reverse direction in all cases. Two of these means were particularly large – these corresponded to the strength of inhibition from $he_1$ in the swim CPG to $ke_2$ and $hf_2$ in the scratch CPG. Initially, we thought the bifurcation diagrams for the swims in the T collection could explain this result. In all of the sets we considered, as the swim stimulus decreased and oscillatory behavior was replaced with steady-state behavior, $he_1$ remained above threshold and $ke_1/hf_1$ remained below threshold (see Figure 14A). In some sets, however, as $\alpha$ continued to de-

crease, $he_1$ exhibited bistable states (both above and below threshold) as well as steady states solely below threshold (with $ke_1/hf_1$ exhibiting tonic steady state activity in those cases, see Figure 14B). The algorithm we used to determine which value of $\alpha$ produced tonic activity always chose $\alpha$ as the largest strength that gave steady state activity before oscillations occurred. Thus, in all of the pairings, the subswim strength we chose exhibited tonic activity from $he_1$ in the swim CPG. Initially, these observations led us to the (incorrect) conclusion
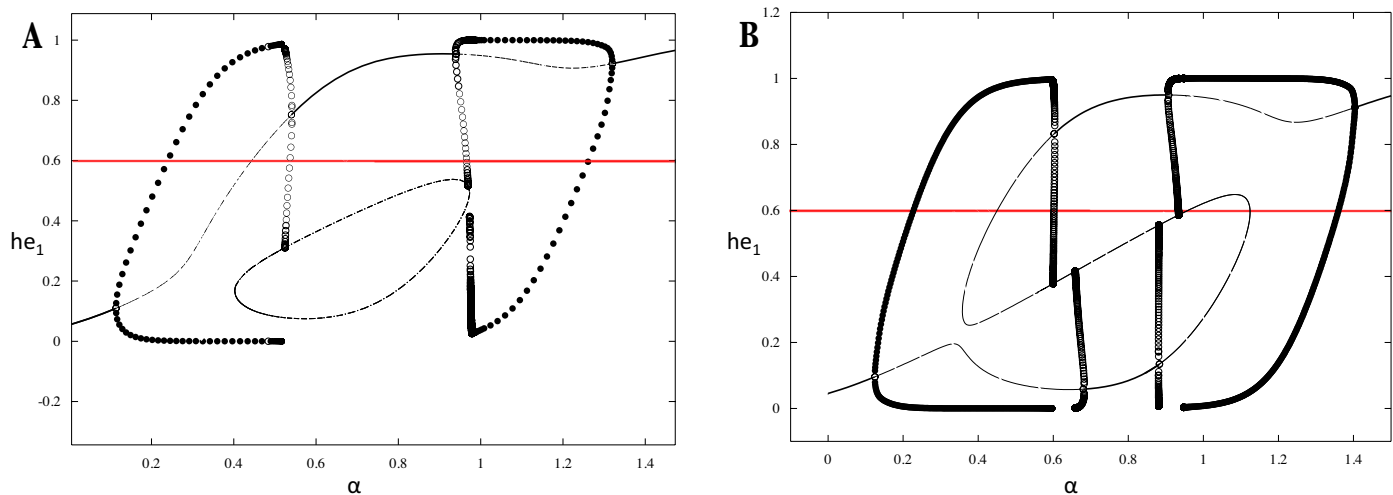


**Figure 14:** *Bifurcation diagrams for two of the T parameter sets. Stable and unstable oscillatory behavior indicated with closed and open circles, respectively. Stable and unstable steady states are indicated with solid and dashed lines, respectively. The threshold is indicated in red. (A) $he_1$ exhibits tonic steady state activity as the swim stimulus is decreases. (B) $he_1$ exhibits tonic activity, then bistability as the stimulus strength is lowered. As in the LinkedT dynamics, oscillations lost their stability as $\alpha$ decreased before steady state behavior was observed (see the caption comment in Figure 8).*

that parameter sets that successfully reproduced Benchmark 4 used the tonic activity in the swim CPG to provide additional inhibition to $ke_2$ and $hf_2$ in the scratch CPG, balancing the total input to those two cells so that they become active in phase, whereas previously they were not. We must emphasize, however, that the input to the motoneurons is a sum of the inputs from both the scratch and swim networks. Thus, no neuron in the swim network can continue to produce tonic activity under dual stimulation, or else the motoneuron it projects to will receive above threshold inputs, and will not produce a rhythmic pattern of any kind. Therefore, it is crucial that under dual stimulation, the scratch network provides

input to the swim network that is strong enough to perturb it back to something rhythmic (presumably, to a swim rhythm), in order for subswim plus scratch to yield swim. This conclusion, while counterintuitive, suggests that our favorable subswim plus scratch dynamics under this collection of swims relies on the fact that the subswim stimulation is close, in some sense, to the baseline swim stimulation. We tested this hypothesis by varying $\alpha$ farther from 1, and chose instead the mean value over the range of swim stimulation strength that produced steady state behavior. This choice of $\alpha$ significantly reduced the number of sets that produced swim under subswim plus scratch stimulation (and also did not increase the number of scratches resulting from this stimulus), supporting this hypothesis. We maintain the conjecture that the stronger inhibition strength to $ke_1$ and $hf_1$ balances the total input to those cells, but verification of this would need to be done on a case by case basis.

In [32], we noticed that the LCPG produced a faster dual rhythm with a slight increase in $HF$ duration, in contrast to experimental results. In that paper, the faster dual rhythms produced in all cases were swims, so it made sense to compare $HF$ and $HE$ duration under swim stimulation with $HF$ and $HE$ duration under dual stimulation. We will do the same here, only with the sets that produce a faster swim under dual stimulation *and* produce either a scratch rhythm (in the case of the S collection) or a swim rhythm (in the case of the T collection) under subswim plus scratch stimulation (as we did in [32]). In both collections, we found sets where frequency increases occurred through decreases in both $HF$ and $HE$ duration, decreases in $HF$ duration alone, and decreases in just $HE$ duration. The S collection most often sped up the dual rhythm by decreasing both $HF$ and $HE$ duration (see Figure 15A). The T collection, however, was equally likely to produce a faster dual swim by decreasing both $HF$ and $HE$ duration or decreasing $HE$ alone (see Figure 15B). Thus, in roughly half of the successful T collection LCPGs, slight increases in $HF$ occurred under dual stimulation, as in [32] and in contrast to experimental results. In the next section, we will investigate this property in the successful UCPG sets we generate. For now, we conclude that this property appears to be dependent on parameter choices and may not necessarily indicate a limitation of the LCPG structure.

Overall, these results support our conjecture in [32], that in the LCPG configuration, a swim CPG with weak output is unlikely to reliably influence and alter the scratch dynamics
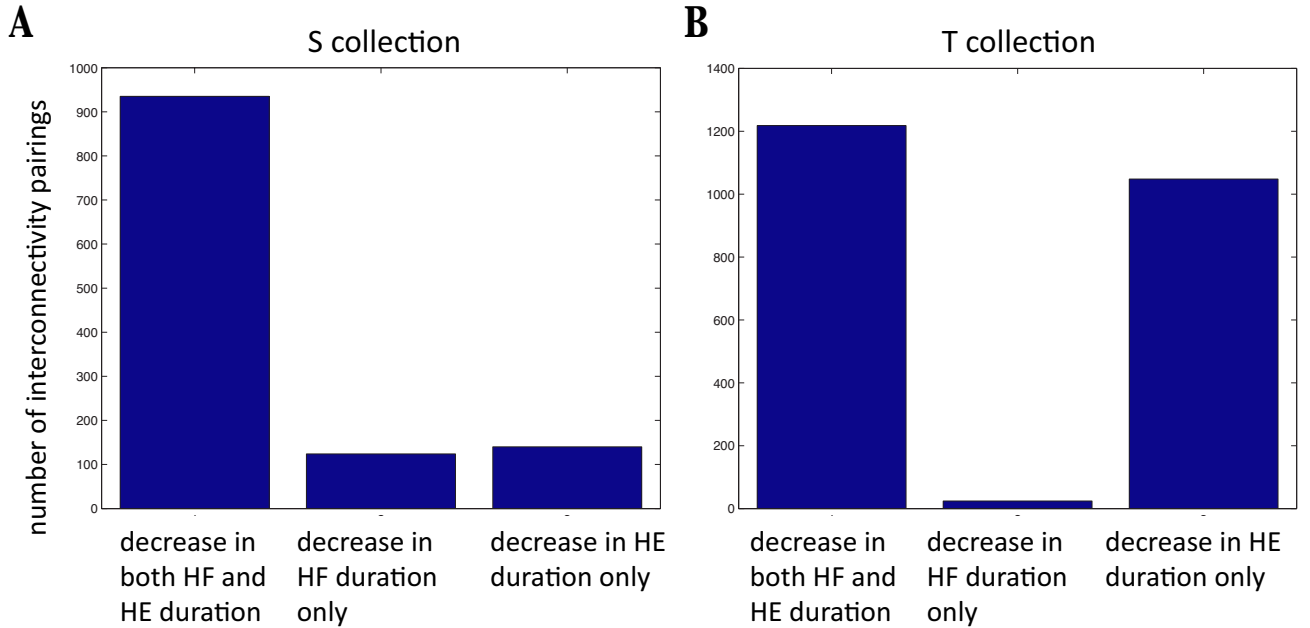
**Figure 15:** *Frequency increases exhibited under dual stimulation swims occur through decreases in HF or HE duration, or both. In (A), we considered S collection LCPGs that produced a faster swim under dual stimulation and a scratch under subswim plus scratch stimulation (as we did in [32]). The majority of connectivity sets produced a faster dual rhythm by decreasing both HF and HE durations. In (B), we considered T collection LCPGs that produced a faster swim under dual stimulation and a swim under subswim plus scratch stimulation (these sets support all of the benchmarks). Dual stimulation swim frequency increases were obtained through either (a) decreases in both HF and HE duration or (b) in HE duration alone. Roughly half of the time, frequency increases occur that cause an increase in HF duration, which contrasts with experimental results.*

in the scratch CPG to produce a combined swim output. The results from this section indicate that in addition, favorable subswim plus scratch dynamics produced by the LCPG likely occurs since the subswim stimulus strength is large, and close to that of the full swim

stimulus. In the next section, we will build parameter sets that fit the UCPG architecture and test those sets for their ability to support the benchmarks. Due to the structure of that model, we must first generate connections and drives that produce scratch in the full network before testing the benchmarks regarding dual stimulation. We will see that this adds significantly complexity to our search.

## 2.7   UCPG RESULTS

Because the units responsible for generating swim and scratch in the LCPG structure were distinct, that architecture could support Benchmark 1 regardless of the connectivity between the CPGs, i.e., we already had drive and connectivity parameters configured within each CPG so that the network was able to produce swim and scratch under different stimulations. In the UCPG structure, however, a subset of neurons is integral to both rhythms, producing swim under a particular stimulation and then generating scratch under a new stimulation (with contribution from additional neurons in the network). See Figure 16 for a detailed schematic of this architecture. We will refer to the 3-cell multifunctional network that participates in both scratch and swim as the "shared" network. We have already built 3-cell networks that produce swim under a particular stimulation (the S and T collections). To build a UCPG, then, we attempted to augment a swim-capable network with three additional neurons, and configure parameters so that the full network generated scratch under a new stimulation. This required 33 new parameters – 24 interconnectivity parameters (shown in red in Figure 16B), 6 scratch drive values (shown in blue in Figure 16B), and 3 time constants.

Recall the results of our 3-cell network trials from Section 2.4 – despite a massive parameter search, we only found approximately 100 sets that produced either of the rhythms we desired. This is important to keep in mind in Section 2.7.1, where we indicate our failed attempts to find parameters that produce scratch in the UCPG network. That discussion motivates our work in Section 2.7.2, where we step back from random searches to more closely analyze the dynamics present in the UnitaryS and UnitaryT sets. Observations from

46
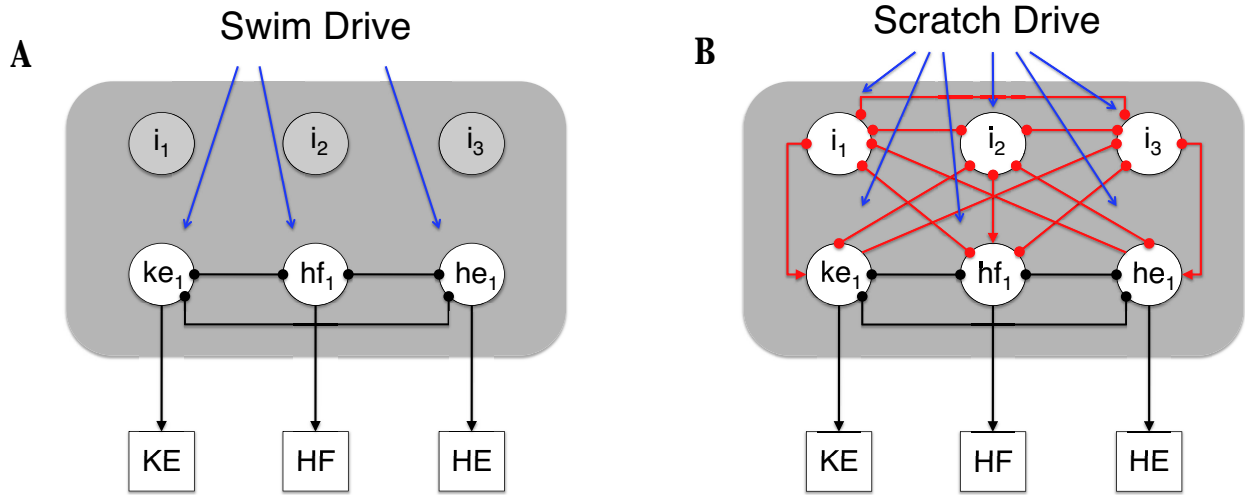
**Figure 16:** *Schematic of the UCPG under different stimulations. (A) During swim, only the shared network is activated ($ke_1, hf_1, he_1$). (B) During scratch, all 6 neurons are activated (the shared network receives a different set of drives than it does during swim, in (A)).*

the performance of the network under those sets suggests a different approach, described in Section 2.7.3, where we found parameter sets that support the benchmarks.

### 2.7.1 Preliminary attempts

As we alluded in the introduction, we attempted to find parameters that generated scratch in the 6-neuron configuration by augmenting a 3-neuron swim-capable network with three additional neurons, which required new connection, drive, and time constant parameters (connections and drives indicated in red and blue, respectively in Figure 16B). We kept the 6 connections within the shared network (shown in black in Figure 16B) fixed at values from the S and T sets and randomly generated the other values using the Latin hypercube sampling procedure, sampling from the intervals we indicated in Section 2.5. A simulation, in this case, consisted of 10000 parameter sets each of size 42, 30 parameters comprising the connections within the network, 6 constant drive parameters, and 6 time constants. Despite many attempts, we could not generate the other connections, time constants, and drives for the

network and cause it to produce scratch. We took cues from the published sets (Tables 3, 4) and chose a smaller drive interval in some simulations (instead of sampling from [0.5, 1.5], we sampled over [0.25, 0.75]), and in other simulations, we set all interconnectivity between the scratch-specialized neurons to zero. We also took cues from the randomly generated scratch sets (Section 2.4) and chose a larger connection interval in some simulations (we sampled excitatory and inhibitory strengths from [0,1.5]). In all of these trials, we only found a handful of sets that could produce scratch and swim under differing stimulations. In each case, some or all of the neuronal outputs were tonically active under dual stimulation.

We conjectured that by starting with a biased shared network (one whose connectivity facilitated swim dynamics under a particular stimulation), we were potentially hindering the search for scratch-capable UCPG sets. Abandoning these attempts, then, we attempted to find parameters that produced scratch from a 6-neuron configuration, instead of augmenting a 3-neuron swim network with 3 additional neurons. We implemented simulations where all of the connections shown in Figure 16B (along with 6 time constants) were randomly generated. In one simulation, we allowed neurons to inhibit or excite any other member of the CPG, but none of the sets produced scratch. We returned to the constraints shown in Figure 16B, prescribing excitatory connections from scratch-specialized neurons to partner neurons in the shared network, and made all other connections inhibitory. In a simulation of size 10000, we were able to produce three sets that generated scratch in the full network. We dissected the connectivity within the shared network from these sets (i.e. pulled the parameters corresponding to black connections in Figure 16B), and randomly generated a swim stimulation simulation of size 10000 for each of those networks (parameters for the blue drives indicated in Figure 16A). We found constant drive parameters that generated swim in the shared network with only one of these sets, but the swims they produced did not satisfy the amplified swim condition (Benchmark 2).

Instead of continuing to randomly search through parameter space, we generated localized sets around the published UCPG values. We formed parameter sets by pulling from a normal distribution with means as the parameters' published values and standard deviations as 5% of those values (so parameters that were identically 0 remained unchanged over all trials). A simulation of 5000 parameter sets was run with each of the two published sets,

| | UnitaryS | UnitaryT |
|---|---|---|
| Sets that do scratch | 2298 | 2118 |
| Sets that do scratch and faster swim | 541 | 46 |
| Sets that do scratch, faster swim, and dual is faster | 297 | 40 |
| Sets that do scratch, faster swim, dual is faster, and subswim + scratch is swim | 257 | 23 |

**Table 6:** *Results from a localized parameter search near the UnitaryS and UnitaryT sets. Sets were tested against the benchmarks in the order they are listed in the table.*

UnitaryS, the unified parameter set that under subswim generated below threshold activity, and UnitaryT, the unified parameter set that under subswim generated tonic activity. First we generated parameters around the connection and drive strengths that the neurons received during scratch. If the output satisfied the scratch criteria, new drives for those sets were generated in a neighborhood of the stimulation that the neurons received during swim. The amplified swim condition, dual stimulation, and subswim criteria were all tested and the results are indicated in Table 6, which shows that we were able to generate other parameter sets in a neighborhood of our published data that are also capable of meeting the benchmarks.

It is notable that many sets could not successfully generate swim and satisfy Benchmark 2 regarding swim frequency increases. Since we first varied the parameters and looked for scratch dynamics produced by the 6-cell network, it may be that the interconnectivity in the shared network now favored scratch dynamics (where $ke_1$, $hf_1$, and $he_1$ are all in antiphase), making it difficult for that network to produce swim under drives generated near the original swim stimulation. In addition, the published swim stimulation drive parameters were large (particularly in the UnitaryT parameter set), meaning the new randomly generated swim drives could be pulled from values far from those we published (since $\sigma$ depended on $\mu$), which may have affected the network's ability to produce swim dynamics.

At the very least, the parameter sets published in [32] are sufficiently robust so that the desired dynamics can be supported under perturbations, but without a better understanding of the mechanisms underlying rhythm generation in our original sets, it is difficult to identify why certain parameter sets do or do not produce favorable results. Taking a step back from

these methods, we will focus our efforts on an analysis of our published UCPG parameter sets. Through a better understanding of their dynamics, we aim to shed light on the best way to generate a collection of UCPG parameter sets we can study.

### 2.7.2 Analysis of the published UCPG sets

A rigorous analysis of how the UCPG network produces different patterns under various forms of stimulation is a challenging task, given that there are 45 free parameters (30 inter-connectivity strengths, 6 time constants, 6 scratch drives and 3 swim drives). Specifically, the large number of neurons in the system creates numerous combinations of possible transitions occurring in the scratch pattern alone. We will focus on understanding the UCPG's performance during scratch at the "crucial" transition, when $he_1$ leaves the active phase. During swim, both $ke_1$ and $hf_1$ activate together at this transition. During scratch, however, $hf_1$ is somehow suppressed and its activation is delayed so that all three neurons activate sequentially. We will reveal how the presence of scratch-specialized neurons alters the output of the shared network from the swim pattern to the scratch pattern in our published sets, and use these observations to motivate a new parameter search, detailed in Section 2.7.3.

Plotting the nullclines in phase space over time indicates how either parameter set is able to maintain inhibition to $hf_1$ during this key transition. In Figure 17, the top frame indicates the nullclines of $ke_1$, $hf_1$, and $he_1$ in blue, red, and green, respectively. In the bottom frame, the nullclines of their drivers are plotted in corresponding colors. The value of $(u_k, a_k)$ for the neurons at each time point is indicated with a star. Under the UnitaryT parameter set, neurons in the driver network activate in the order required for the scratch pattern and excite their partner cell in the shared network, suppressing the other neurons. At the crucial transition, $i_1$ activates prior to the end of $he_1$'s active phase, providing inhibition to $hf_1$ and excitation to $ke_1$, which delays the active phase of $hf_1$ relative to that of $ke_1$ (see Figure 17).

Activation of $i_1$ is not responsible for suppression of $hf_1$ at the crucial transition under the UnitaryS parameter set. In fact, the activity levels of $i_1$ and $i_2$ do not vary far from 0 at any point during the rhythm, as exhibited in the bottom frames in Figure 18. Instead, transitions occur primarily in the shared layer (see Figure 18, frames and colors configured

50
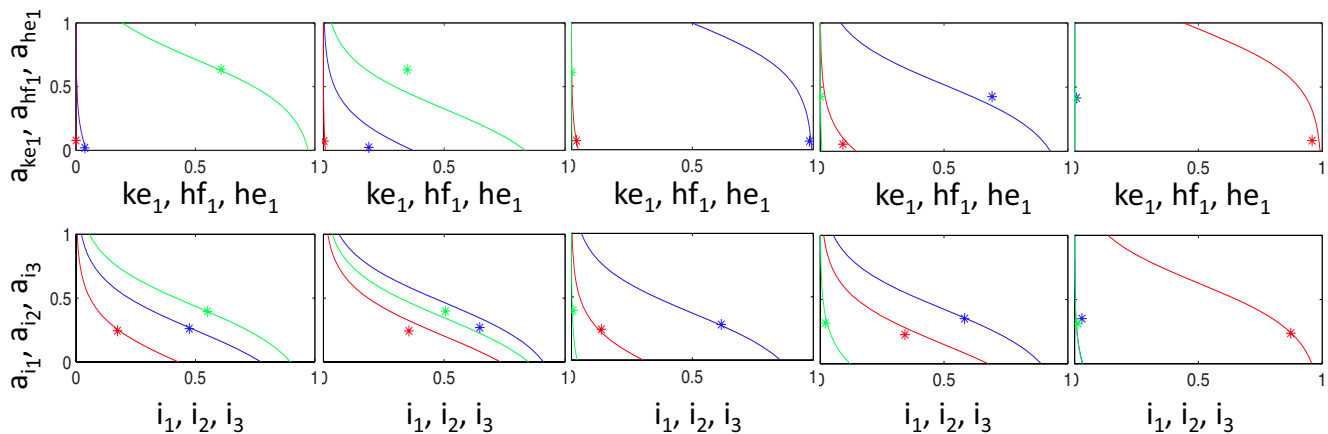
**Figure 17:** *Activation of neurons at five time points during the crucial scratch transition under the UnitaryT parameter set. In the top plot of each frame, the nullclines of $ke_1, hf_1$, and $he_1$ are plotted in phase space in blue, red, and green, respectively. The nullclines for $i_1, i_2$, and $i_3$ are plotted in the bottom plot with corresponding colors. In the first two frames, $he_1$ and $i_3$ leave the active phase, and parameters are configured so that $i_1$ enters the active phase first, exciting its partner cell $ke_1$ and suppressing $hf_1$ in the third frame. Eventually (transient not shown), $i_2$ recovers from inhibition in the fourth frame, and provides excitation to $hf_1$, which enters the active phase in frame 5. In this network, the driver cells $i_1, i_2$, and $i_3$ control the timing of transitions and provide excitation to their partner cells to facilitate scratch dynamics.*

with the same scheme described previously). As $he_1$ and $i_3$ shut down, $ke_1$ enters the active phase. $hf_1$ does not immediately activate for two reasons: first, the constant drive to $hf_1$ is smaller than the drive to $ke_1$, and second, $he_1$ provides less inhibition to $ke_1$ than it does to $hf_1$ (see Table 4). Also, although the activity level of $i_1$ is small, it provides additional inhibition to $hf_1$ during this transition. Since the overall inhibition to $hf_1$ is larger than the inhibition to $ke_1$, $hf_1$ remains suppressed at the crucial transition, but is able to gradually increase its activity level and enter the active phase as inhibition from $ke_1$ and $i_1$ wears off. These dynamics are facilitated due to the weak strength of the scratch stimulus. Under swim stimulation, the constant drive to the cells is very large, dominating slight differences in inhibition strength and allowing activation of $hf_1$ in spite of inhibition from $ke_1$. Under the weaker scratch stimulation, the strength of inhibition from other neurons have a significant
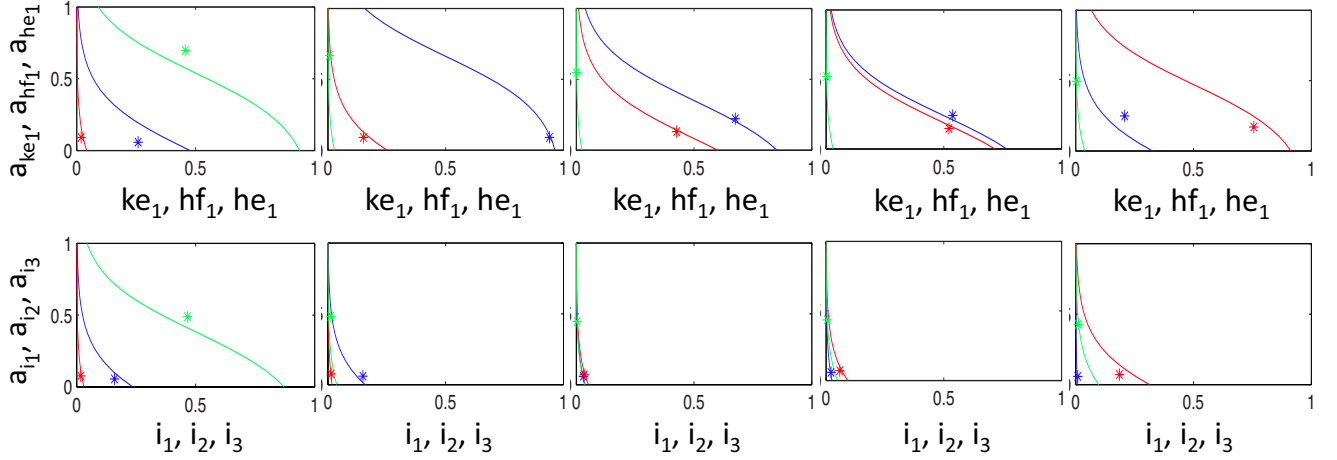
**Figure 18:** *Activation of neurons at five time points during the crucial scratch transition under the UnitaryS parameter set (correspondence between colors and neurons is the same as in Figure 17). In the first frame, $he_1$ and $i_3$ shut down, allowing $ke_1$ to enter the active phase in frame two (recall that threshold is at $\theta_{th} = 0.6$). Inhibition from $ke_1$ and $i_1$ keeps $hf_1$ suppressed for a transient (not shown) until $hf_1$ is eventually able to enter the active phase and suppress $ke_1$ over the last three frames.*

influence on the network dynamics, and $ke_1$ and $hf_1$ are able to activate in anti-phase.

Since the activity level of the scratch-specialized neurons was weak, we tested whether the shared network could act solely as a multifunctional network able to produce both swim and scratch under different stimulations. We integrated the 3-cell network with the drive it received during scratch and did not excite the additional scratch-specialized neurons. This network still maintained a swim-like rhythm under this stimulation ($ke_1$ and $hf_1$ were in phase together and out of phase with $he_1$), indicating that these scratch-specialized neurons were indeed necessary for producing scratch, highlighting the fact that a population need not produce extremely strong output to be important or impactful.

In conjunction with this phase plane discussion, we conducted a sensitivity analysis of the sets to ascertain the influence that certain parameters have on UCPG performance. We selected a parameter and generated a normal distribution around it by choosing $\mu$ equal to its

published value and $\sigma$ as 20% of that value. Fixing all of the other choices at their published values, we generated a large simulation where we replaced this particular parameter with choices from the normal distribution. For the UnitaryS set, the scratch rhythm was robust to changes in most parameters, but fairly sensitive to parameter changes in the strength from $he_1$ to $ke_1$ and to variations in the scratch drives (with particular sensitivity to changes in the drive to $ke_1$ and $hf_1$). In fact, sets where the drive to $ke_1$ was smaller than the drive to $hf_1$ were never able to produce scratch. That is, when we varied either the drive to $ke_1$ or the drive to $hf_1$, only sets that left the relationship where the drive to $ke_1$ was larger than $hf_1$ intact produced scratches. This was not surprising given our previous discussion that the scratch dynamics rely on the difference in drive to these two neurons (as well as the relative strengths of inhibition they receive).

Additionally, varying certain parameters in a particular direction (larger or smaller than the chosen value) was detrimental in certain cases. Sets were less likely to produce scratch when the inhibition strength from $he_1$ to $ke_1$ was increased, inhibition from $i_2$ to $ke_1$ was decreased, excitation from $i_3$ to $he_1$ was decreased, drive to $he_1$ was increased, drive to $i_2$ was decreased, or drive to $i_3$ was increased. The negative consequences of modifying parameters in a certain direction seemed clear for some of these cases, for instance, reducing the inhibition from $i_2$ to $ke_1$ might allow $ke_1$ to remain on during $hf_1$'s active phase (and thus the system would produce swim, not scratch). Other results appear to be conflicting, for instance, drive increases to $i_3$ are detrimental, which might lead to the conclusion that stronger $i_3$ output produces excessive excitation to its partner cell $he_1$. Note, however, that excitation increases from $i_3$ to its partner cell $he_1$ were *more* likely to produce scratches than decreases were. We are led to conclude that increases in drive to $i_3$ would detrimentally manipulate the inhibitory pathways to $ke_1$ and $hf_1$, potentially interrupting the delicate balance of total input they receive to promote anti-phase activity.

Unlike the UnitaryS dynamics, scratch behavior with the UnitaryT set was produced under driving input from the scratch-specialized neurons. Recall that the scratch-specialized neurons in our published sets were not interconnected, and could only impact each other through the shared neurons. Thus, the ability of the scratch-specialized neurons to activate in the scratch ordering was produced in conjunction with the shared network. This caused

the set to be significantly less robust to changes in parameters, as it was sensitive to variations in inhibition from $he_1$, $i_1$, and $i_2$ to $ke_1$, excitation from $i_3$ to $he_1$, inhibition to $i_1$ from $hf_1$ and $he_1$, inhibition to $i_2$ from $ke_1$ and $he_1$, and to all of the drive parameters, except for the input to $hf_1$. In particular, sets were less likely to produce scratch when the drive to $ke_1$, $he_1$, $i_2$, $i_3$ was increased, drive to $i_1$ was decreased, inhibition from $i_2$ to $he_1$ and $ke_1$ was decreased, inhibition from $i_1$ to $he_1$ and $ke_1$ was increased, excitation from $i_3$ to $he$ was decreased, excitation from $i_1$ to $ke_1$ was decreased, and inhibition from $he_1$ to $ke_1$ was increased. Also, see the results from Table 6, which provides further indication that this set was more sensitive to changes than the UnitaryS choice of parameters.

In this section, we discussed the mechanisms underlying oscillations in our published UCPG parameter sets and generated a sensitivity analysis that highlighted how changes in drive strength and interconnectivity affected the network's performance. The interconnectivity in this structure yields a complex environment where many competing factors are present, and in light of this discussion, it is perhaps not surprising that completely random connectivity sets were unlikely to yield favorable results, especially given the requirements on duration of activation as well as proper ordering. In the UnitaryS parameter set, relative interconnectivity and stimulus strengths to $ke_1$ and $hf_1$ were crucial to producing scratch. In the UnitaryT parameter set, the scratch rhythm was generated by the driver network, but these oscillations were facilitated through mutual inhibition between those cells and the shared network. In either case, the shared network utilized inhibition/excitation from neighboring cells to effectively alter its output under different stimulation.

Despite the fact that the UnitaryT set was less robust to parameter changes, the concept underlying its performance provided us with an an idea that suggested a new type of simulation. We had already unsuccessfully configured UCPGs where the shared network had inherent connectivity that promoted swim. Perhaps if the scratch-specialized neurons had an inherent connectivity that promoted scratch, they could drive the shared network to generate scratch as well. In the next section, we will align a scratch producing three cell network and a swim producing three cell network in the UCPG framework and attempt to generate connections between them that will enable the shared network to produce scratch under a particular stimulation, and meet the other benchmarks as well.

54

### 2.7.3 Scratch network drives a swim network to scratch in the UCPG

In the previous section, we saw that scratch was produced under the UnitaryT parameter set due to the sequential activation of scratch-specialized neurons, which excited their partner cells to activate in the proper ordering. This concept provided us with the idea to generate UCPGs where the shared network is supplemented with scratch-specialized drivers that are inclined to produce scratch in isolation, in the hopes that the network might produce scratch. We arranged the 3-neuron scratch and swim sets we generated in Section 2.5 in the UCPG configuration and randomly generated connections between the two networks (implementing excitatory connections from the drivers to their partner cells, and inhibitory values for all other connections). The scratch-specialized network was given the scratch drive it received when it performed scratch in isolation, and additional drives to the shared network were randomly generated and applied during scratch. We paired 9 of the swims (S1-S6 from Table 5 along with 3 additional choices, one from each cluster) with 10 scratches from the scratch collection (the 4 scratches from Table 5, and 6 more choices with varying durations), generating 5000 sets of connectivity parameters for each pairing.

These sets were tested for their ability to produce scratch, faster swim, and the dual requirement (Benchmarks 1-3). Of these, 648 performed the scratch rhythm, which was already a vast improvement from our previous attempts. 35 of those managed to produce a dual rhythm that was faster than either of the swim or scratch frequencies alone. Under subthreshold swim stimulation plus full scratch stimulation, 4 of those sets produced a swim rhythm. We investigated the mechanisms in these 4 sets, and found that 3 had the property that $i_1$ became active first relative to $i_2, ke_1$, and $hf_1$, which allowed it to excite $ke_1$ and suppress $hf_1$ at the crucial transition. In the last set, stronger inhibition from $i_3$ to $hf_1$ allowed $ke_1$ to become active first and suppress $hf_1$ briefly to produce the scratch rhythm. Note the similarity between these two mechanisms and those present in the published sets. In the UnitaryT dynamics, the driver cells activate first, exciting their partner neurons above threshold. In the UnitaryS dynamics, a slight difference in the total input to $ke_1$ versus $hf_1$ enabled the scratch rhythm to be produced.

Consider the former condition: assuming that at the crucial transition only $he_1$ and $i_3$

are active, then $i_1$ will activate first if its total input is greater than the total input to the other cells, $ke_1$, $hf_1$, and $i_2$. If $he_1$ and $i_3$ are near saturation (close to 1), this presents a condition we will call Property A, that $I_{i_1} - b_{i_1 he_1} - b_{i_1 i_3} > \max\{I_{ke_1} - b_{ke_1 he_1} - b_{ke_1 he_1},$ $I_{hf_1} - b_{hf_1 he_1} - b_{hf_1 i_3}, I_{i_2} - b_{i_2 he_1} - b_{i_2 i_3}\}$. The latter condition, that the overall inhibition is stronger to $hf_1$ than $ke_1$ produces Property B: $I_{ke_1} - b_{ke_1 he_1} - b_{ke_1 i_3} > I_{hf_1} - b_{hf_1 he_1} - b_{hf_1 i_3}$. We note that both of the published sets have these two properties, and all of the UCPG sets generated with the S collection that produced scratch, swim, and a faster dual rhythm had at least one of these two properties.

We also paired 9 of the swims in the T collection with the same 10 scratches (T1-T6 and three additional selections, one from each cluster). This generated 360 scratches, 19 of which produced a faster rhythm under dual stimulation. When the swim stimulus was reduced and tonic activity was paired with full scratch stimulation, none of these sets produced a distinguishable rhythm (either a scratch or a swim). Since the majority of the scratches produced from the S collection had Property A, we tailored a simulation so that we only tested parameters that satisfied this property. By doing so, we generated 4 sets that met all 4 benchmarks, including generating a swim when subswim (which in this case, produced tonic activity in the shared network) plus full scratch stimulus was applied.

In this section, we used ideas underlying the performance of one of our published sets to motivate a new search for UCPG parameter sets. This search generated 8 UCPG parameter sets that were able to support all of the benchmarks. 7 of the 8 sets had Property A, indicating that at the crucial transition, $i_1$ activated first to excite its partner cell and suppressed $hf_1$, so that $ke_1$ and $hf_1$ activated sequentially, and not in phase. The property is similar to the dynamics produced by the UnitaryT set. The last set exhibited dynamics similar to those produced by the UnitaryS set, where scratch was generated because the inhibition to $hf_1$ was slightly stronger than the inhibition to $ke_1$. Unlike the LCPG configuration, the ability of this structure to meet Benchmark 4 did not depend on the output of the swim network under subswim, since 4 of these sets produced below threshold activity under subswim and 4 produced tonic activity under subswim.

Further, in all of the sets that produced a faster dual rhythm that was a swim, we tested whether increases occurred due to decreases in $HE$, $HF$, or both, as we did with the

56

LCPG configuration. Unlike in that configuration (see Figure 15), all of these sets underwent frequency increases due to decreases in both $HE$ and $HF$ duration, which concurred with experimental results. These results support the conclusions we drew in [32], favoring the UCPG structure as the most likely to have produced our collaborators' results.

## 2.8 ANALYSIS OF A SIMPLIFIED MODEL HELPS OBTAIN SETS WITH DESIRABLE DYNAMICS

As we indicated in section 2.4, our attempts to randomly generate a T collection, parameter sets that generate a swim rhythm under full stimulation but tonic activity under subthreshold swim stimulation, were not fruitful. In this section, we describe the analytical arguments we used to constrain parameter space in such a way that produced 27 sets that meet this swim criterion. First, since $ke_1$ and $hf_1$ perform identically during the swim rhythm, we reduced the system and considered a 2-neuron model of the form:

$$\dot{w}_1 = -w_1 + f_T(\alpha J_1 - bw_2 - ga_1)$$
$$\dot{w}_2 = -w_2 + f_T(\alpha J_2 - cw_1 - ga_2)$$
$$\tau \dot{a}_1 = -a_1 + w_1$$
$$\tau \dot{a}_2 = -a_2 + w_2. \tag{2.3}$$

In this system, $w_1$ represented the dynamics of $ke_1$ and $hf_1$ and $w_2$ represented the dynamics of $he_1$. We sought parameters $\{b, c, J_1, J_2, \tau\}$ such that at full stimulation strength ($\alpha = 1$), the system produced antiphase oscillations and that under reduced stimulation strength (for some $\alpha < 1$), the system exhibited tonic activity in either $w_1$ or $w_2$. These sets could then be recast into the 3-neuron system by setting $b_{ke_1hf_1} = b_{hf_1ke_1} = 0$, $I_{ke_1} = I_{hf_1} = J_1$, $b_{ke_1he_1} = b_{hf_1he_1} = b$, $b_{he_1ke_1} = b_{he_1hf_1} = c/2$, and $\tau_1 = \tau_2 = \tau_3 = \tau$. These sets produce swim under full stimulation and tonic activity under reduced stimulation, which are the dynamics we desire in order to evaluate the performance of the models' under different types of subswim activity. Note that these sets will be of a particular form where $ke_1$ and $hf_1$ do not inhibit

57

each other and interact with $he_1$ equivalently. Since $\tau$ is large, $w_1$ and $w_2$ will be treated as fast variables, and $a_1$ and $a_2$ as slow variables (see discussion in Section 2.2).

Analysis on system (2.3) has been done extensively for the case when $b = c$ and $J_1 = J_2$ in [18]. In that paper, oscillations can devolve into winner take all activity as $\alpha$ varies, which are the precise dynamics we are trying to produce. The symmetry in the system produces oscillations where the active durations of $w_1$ and $w_2$ are equal (and vary identically with changes in input). Because the swim rhythm requires KE/HF and HE to have unequal active durations (see the description in Section 2.2), we will not prescribe the conditions that the neurons inhibit each other equally and receive the same constant input. This drastically complicates the analysis when $f_T$ is smooth.

As in [18], we first analyzed system (2.3) by approximating $f_T$ by a Heaviside function. The parameter constraints developed from this analysis depended strongly on that simplification. When we simulated sets constrained by the Heaviside analysis in the full system, we did not obtain all of the dynamics we were searching for. We omit the details of that analysis and instead present the arguments in the case where $f_T$ is approximated by a piecewise linear function. This analysis provides constraints on parameter space that yield antiphase oscillations under full input ($\alpha = 1$) and tonic activity for some $\alpha$ less than 1. These constraints are then used to produce potential parameter sets that can be evaluated for appropriate dynamics in the case where $f_T$ is smooth.

Consider the case where

$$
f_T(x) = \begin{cases} 1 & \text{if } x > A(m) = 1/(2m) + \theta; \\ m(x - \theta) + 1/2 & \text{if } B(m) \leq x \leq A(m); \\ 0 & \text{if } x < B(m) = -1/(2m) + \theta, \end{cases}
$$

where $m$ indicates the slope of the function. See Figure 19.

With this description of $f_T$, the $w_1$-nullcline is defined by

$$
w_1 = \begin{cases} 1 & \text{if } \alpha J_1 - bw_2 - ga_1 > A; \\ m(\alpha J_1 - bw_2 - ga_1 - \theta) + 1/2 & \text{if } B \leq \alpha J_1 - bw_2 - ga_1 \leq A; \\ 0 & \text{if } \alpha J_1 - bw_2 - ga_1 < B, \end{cases}
$$

58
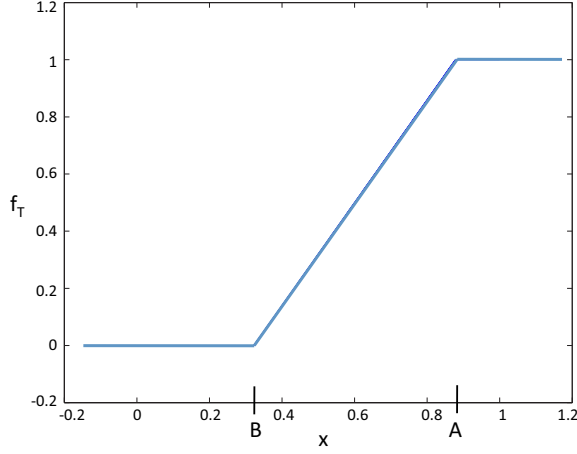
**Figure 19:** $f_T$ *against* $x$. *The function is zero when* $x$ *is less than* $B$, *sloped for* $x$ *values between* $B$ *and* $A$, *and one when* $x$ *is larger than* $A$. *Values shown for* $m = 1.8$.

or

$$w_1 = \begin{cases} 1 & \text{if } w_2 < w_2^l; \\ m(\alpha J_1 - bw_2 - ga_1 - \theta) + 1/2 & \text{if } w_2^l \le w_2 \le w_2^u; \\ 0 & \text{if } w_2^u < w_2, \end{cases} \qquad (2.4)$$

where $w_2^l = w_2^l(a_1) = (\alpha J_1 - A - ga_1)/b$ and $w_2^u = w_2^u(a_1) = (\alpha J_1 - B - ga_1)/b$. Analogously, the $w_2$-nullcline is defined by

$$w_2 = \begin{cases} 1 & \text{if } w_1 < w_1^l; \\ m(\alpha J_2 - cw_1 - ga_2 - \theta) + 1/2 & \text{if } w_1^l \le w_1 \le w_1^u; \\ 0 & \text{if } w_1^u < w_1, \end{cases} \qquad (2.5)$$

where $w_1^l = w_1^l(a_2) = (\alpha J_2 - A - ga_2)/c$ and $w_1^u = w_1^u(a_2) = (\alpha J_2 - B - ga_2)/c$. See Figure 20.

Assume that we initialize the system at the state $(w_1, w_2) = (1, 0)$. In this case, $a_1$ increases and $a_2$ decreases. This causes the $w_1$ nullcline to shift downward in $(w_1, w_2)$ space, and the $w_2$ nullcline to shift to the right, as shown in Figure 20. $w_1$ remains in the dominant state until the nullclines separate, which can occur in one of two ways. These configurations are shown in Figure 21. In Figure 21A, the $w_2$-nullcline has shifted far to the right, causing

59
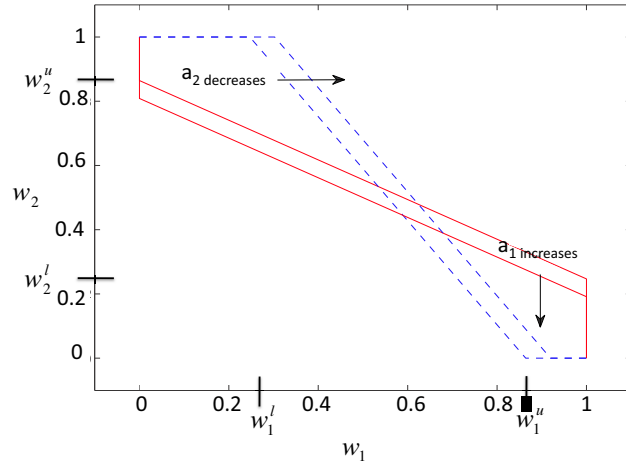
**Figure 20:** *Movement of the nullclines over time. Solid red curves indicate the $w_1$ nullcline, dotted blue the $w_2$ nullcline. $w_2^l$, $w_2^u$, $w_1^l$, and $w_1^u$ are indicated for the first time point.*
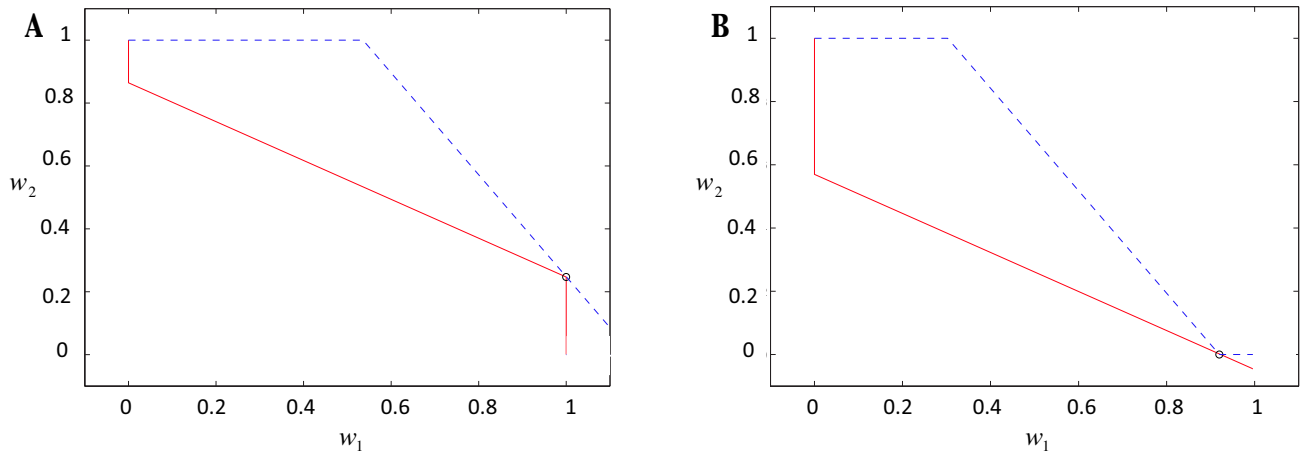


**Figure 21:** *Potential nullcline configurations plotted in the $(w_1, w_2)$ plane prior to a transition in fast time. The $w_1$-nullcline is solid red, the $w_2$-nullcline dotted blue and the state of the fast variables is denoted with a black circle. In slow time, the state with $w_1$ dominant shifts away from $(1,0)$ with: (A) increasing $w_2$ and (B) with decreasing $w_1$.*

the fast state to move with increasing $w_2$ from (1,0) to $(1, w_2^l)$. As $a_1$ and $a_2$ continue to grow and decay, respectively, this intersection point will vanish and the fast system will be attracted to (0,1). We call this "escape" because it is the firing rate of the inactive population that has increased to produce a dominance switch in the system. Alternatively, $a_1$ could have sufficiently decreased so that the $w_1$-nullcline has shifted as shown in Figure 21B. In that case, the fast state has moved with decreasing $w_1$ from (1,0) to $(w_1^u, 0)$ prior to the transition. We call this situation "release" since it is the firing rate of the active population that decreases to facilitate the jump. In the following, we determine the conditions necessary for a jump to occur through either of these mechanisms.

Starting with the escape configuration, let $t_{me}$ denote the time when the nullcline intersection point begins to move away from $(1, 0)$ with increasing $w_2$, and $t_e$ the moment of separation (when the nullclines are configured as shown in Figure 21A). $t_{me}$ occurs when the corner of the $w_2$ nullcline meets $w_1 \equiv 1$, or when $w_1^u = 1$. $t_e$ occurs when the corner of the $w_1$-nullcline intersects the sloped part of the $w_2$-nullcline, an intersection described by $w_2^l = m(\alpha J_2 - c - g a_2(t_e) - \theta) + 1/2$. Substituting in the definition of $w_2^l$, escape occurs when $a_1$ and $a_2$ satisfy a relationship described by $a_2 = -(1/g)(\frac{\alpha J_1 - A - g a_1 - b/2}{bm} - \alpha J_2 + c + \theta)$. This curve is plotted with a solid blue line in Figure 22 for parameters chosen near the published parameters (our published sets do not satisfy all of the assumptions implemented here).

In the release configuration, let $t_{mr}$ denote the time when the nullcline intersection point begins to move away from $(1, 0)$ with decreasing $w_1$, and $t_r$ the moment of separation (as shown in Figure 21B). $t_r$ occurs when the corner of the $w_2$-nullcline intersects the sloped part of the $w_1$-nullcline, an intersection described by $w_1^u = m(\alpha J_1 - g a_1(t_r) - \theta) + 1/2$. Using the definition of $w_1^u$, release occurs when $a_1$ and $a_2$ satisfy a relationship described by $a_2 = (1/g)(\alpha J_2 - B - cm(\alpha J_1 - g a_1 - \theta) - c/2)$. This release curve is plotted with a solid red in Figure 22.

The transition from $(0, 1)$ is completely analogous. In this case, $a_1$ decreases and $a_2$ increases, which causes the $w_1$ nullcline to shift up in the fast subsystem phase plane, and the $w_2$ nullcline to move to the left. For the escape mechanism, the fast state with $w_2$ dominant moves from $(0, 1)$ to $(w_1^l, 1)$ before the nullclines separate. In release, the fast state with $w_2$ dominant moves from $(0, 1)$ to $(0, w_2^u)$ before the nullclines separate. Using

61

the same line of analysis as in the previous case, the escape curve can be determined and satisfies $a_2 = -(1/g)(\alpha J_2 - A - cm(\alpha J_1 - b - ga_1 - \theta) - c/2)$. The release curve is defined by $a_2 = -(1/g)(\frac{\alpha J_1 - B - ga_1 - b/2}{bm} - \alpha J_2 + \theta)$. These curves are plotted with solid green and purple lines, respectively, in Figure 22.

Rewritten, the curves satisfy

$$\text{Escape from (1,0): } a_2 = \frac{1}{bm}a_1 + \frac{1}{g}(\alpha J_2 - c - \theta - \frac{\alpha J_1 - A - b/2}{bm}) \tag{2.6}$$

$$\text{Release from (1,0): } a_2 = cma_1 + \frac{1}{g}(\alpha J_2 - B - cm(\alpha J_1 - \theta) - c/2) \tag{2.7}$$

$$\text{Escape from (0,1): } a_2 = cma_1 + \frac{1}{g}(\alpha J_2 - A - cm(\alpha J_1 - b - \theta) - c/2) \tag{2.8}$$

$$\text{Release from (0,1): } a_2 = \frac{1}{bm}a_1 + \frac{1}{g}(\alpha J_2 - \theta - \frac{\alpha J_1 - B - b/2}{bm}) \tag{2.9}$$

While these equations do not readily identify optimal parameter choices for each of the parameters, we can see the effect of varying $\alpha$. Equations (2.6) and (2.9) contain a factor of $\frac{\alpha}{g}(J_2 - \frac{J_1}{bm})$. Parameters similar to our published sets cause this factor to be positive, so decreasing $\alpha$ shifts both of these curves down in phase space (compare the blue/purple solid curves with the blue/purple dashed curves in Figure 22). The other two equations contain the term $\frac{\alpha}{g}(J_2 - cmJ_1)$. Our parameter choices cause this factor to be negative, so decreasing $\alpha$ shifts the green and red curves in Figure 22 upwards. Thus, decreasing $\alpha$ shifts the escape curves outwards (away from center) and the release curves inwards (towards center). This indicates that decreasing $\alpha$ promotes transitions via a release mechanism.

Which parameter choices will guarantee escape? Starting from the fast state $(w_1, w_2) = (1, 0)$. Assuming $t_{me}$ is reached before $t_{mr}$, the dynamics of $a_1$ and $a_2$ satisfy

$$a_1(t) = 1 - (1 - a_1(0))e^{-t/\tau}; t \in [0, t_e]$$

$$a_2(t) = \begin{cases} a_2(0)e^{-t/\tau} & ; t \in [0, t_{me}] \\ \frac{[(-1-mg)a_2(t_{me}) + m(\alpha J_2 - c - \theta) + 1/2]e^{-(1+mg)(t - t_{me})/\tau} - m(\alpha J_2 - c - \theta) - 1/2}{-1 - mg} & ; t \in (t_{me}, t_e]. \end{cases} \tag{2.10}$$

The $a_1$ dynamics are simply defined since $w_1 = 1$ until the nullclines separate. The $a_2$ dynamics are piecewise defined since $w_2$ remains at 0 until $t_{me}$, and then increases according to the definition of the "sloped" part of the inhibited nullcline, that is $w_2 = m(\alpha J_2 - c -$

62
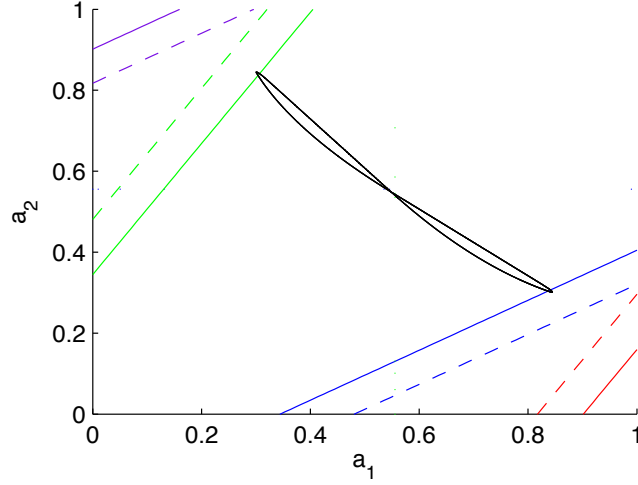
**Figure 22:** *Escape and release curves plotted in $(a_1, a_2)$ for two values of $\alpha$ (solid, $\alpha = 1$, dotted, $\alpha = 0.9$). The relationship between slow variables that triggers a transition in fast time by an escape mechanism is shown in green and blue. The relationship between slow variables that triggers a transition in fast time by a release mechanism is shown in purple and red. The solution trajectory is plotted in black.*

$ga_2 - \theta) + 1/2$. In the limit, $(a_1, a_2)$ approaches $(1, a_2^c)$ as $t \to \infty$ in slow time, where $a_2^c := (m(\alpha J_2 - c - \theta) + 1/2))/(1 + mg)$ (from equation (2.10)). With appropriate parameter choices, $a_2$ decreases monotonically in $a_1$, and thus escape will occur if $a_2^c \leq a_2^e$, where $a_2^e := (-1/g)((\alpha J_1 - A - g - b/2)/(bm) - \alpha J_2 + c + \theta)$ is the $a_2$ value where the escape curve intersects $a_1 \equiv 1$.

We use these arguments to constrain parameter space to ensure the trajectory intersects the escape, not the release curves. First, transitions by release initiate when $w_2^l = 0$ in the $(1, 0)$ case, or when $a_1 = (J_1 - A)/g$. By bounding parameters so that $(J_1 - A)/g > 1$, we can avoid transitions by release (with an analogous condition for the other transition). Next, we want $t_{me}$ (and the analogous time point in the other transition) to be attained, so we choose parameters so that $w_1^u = 1$ can be reached by bounding $0 \leq (J_2 - c - B)/g < 1$. We randomly choose $b$ and $c$ and then pull choices for $J_1$ and $J_2$ within these bounds. Next, we check to make sure the escape curve can be reached by the trajectory; that is, with those choices, $a_2^c \leq a_2^e$. If all of these conditions are met, we require one final condition.

63

Note that if an $\alpha$ exists such that $t_{me}, t_{mr}$ cannot be reached (i.e. if $(\alpha J_1 - A)/g > 1$ and $(\alpha J_1 - B - b)/g < 0$) then a transition cannot occur. We check to make sure an $\alpha < 1$ exists satisfying these conditions. This will ensure that some value exists such that lowering the swim stimulation will result in a steady state solution. If all of these conditions hold, we transform this "informed" candidate set into the full system (we described this process in the introduction to this section) and test for the swim, faster amplified swim, and tonic activity conditions, simulating them with the smooth formulation of S. Note that these are not sufficient conditions but merely guiding constraints for the type of activity we are looking for. Failure might occur due to the arguments' dependency on the piecewise nullcline shape, inability to meet the duration requirements, and so on. In spite of this, we obtain 27 sets that generate swim in a 3-neuron network. Increases in the drive strength lead to frequency increases, and decreases in the drive strength lead to steady state activity in one or more neurons. Thus, we now have sets that satisfy our tonic failure requirement, which proved elusive in completely random trials.

## 2.9   DISCUSSION

Computational model simulations support the hypothesis that networks responsible for scratch and swim rhythmogenesis interact directly. We found that both separate scratch and swim networks interacting through synaptic coupling (LCPG) and a unitary network with components that are necessary for both rhythms (UCPG) could match experimental results, but this performance required parameter tuning so that neurons became active by an escape mechanism, in which recovery from adaptation allowed them to overcome sustained inhibition from other neurons [19, 71, 79]. Under such tuning, uniformly increasing the drives to model neurons in a network accelerates the networks rhythmic activity [68, 73]. Based on the ability to recover a swim rhythm from combining scratch stimulation with a subthreshold swim stimulation that did not elicit CPG output, our simulations favor the possibility that common elements are involved in scratch and swim rhythmogenesis. Moreover, the conjecture that rhythm generation operates in an escape mode leads to a prediction that it should

64

be possible to independently modulate particular phase durations within each rhythm by variation of drives to specific neurons, which would yield maximal behavioral flexibility yet does not arise with other phase transition mechanisms [19].

We simulated models consisting of Wilson-Cowan equations [25], a rather general representation of the activity of interacting neurons. This modeling framework was used previously in studies of rhythm generation e.g., [68] and includes common features, such as a saturating function that converts changes in inputs into effects on activity and a simple form of adaptation. This model choice is appropriate, given the current lack of knowledge about the rhythmogenic neurons relevant to the activity patterns we investigated. By considering relatively simple model networks of three fundamentally distinct types, we provided general arguments for why rhythmic modules lacking direct interactions are unlikely to account for our experimental results and highlighted qualitative distinctions between the capabilities of two different forms of interacting rhythmic circuits. We also note that since a common modeling framework was used for scratch and swim CPG components, our results show that a tendency to shift toward swim-like outputs, away from scratch outputs, can emerge from the coupling properties of the relevant CPGs, rather than requiring distinct forms of intrinsic dynamics.

By varying the swim stimulation amplitude and frequency, we found that the type of dual-stimulation effect depended on the strength of the swim stimulation. Thus the level of excitation in the swim network may influence whether and how an intermediate motor pattern is produced. Related results have been obtained combining stimulation for two forms of scratching. Following a rostral scratch/pocket scratch blend, a sub- threshold pocket scratch stimulus can initiate pocket scratching; following rostral scratching, a suprathreshold pocket scratch stimulus can re-initiate rostral scratching [15]. This may also be analogous to the crayfish choice among feeding, escaping, or some intermediate behavior, which depends on food size [7]. Also, in the crustacean stomatogastric nervous system, increasing the robustness of one motor pattern can cause some neurons to switch gradually from one firing pattern to another through hybrid firing patterns [45]; a similar mechanism might underlie hybrid and intermediate motor patterns in turtles.

One limitation to this study is the qualitative nature of the benchmarks. The rhythms we

have considered are described by their ordering and relative durations, which requires that we also judge model performance according to these stipulations. Without a quantitative cost function, however, it is difficult to effectively compare the performance of various parameter sets. As it stands, we have build up a large collection of sets we consider unsuccessful for producing certain dynamics, but the degree to which they are unsuccessful is completely uncharacterized. Here, "failure" can mean many things, depending on the dynamics we are testing them for – the output could be not rhythmic, swim-like but not satisfy the rigid swim requirements, or scratch-like but not satisfy the rigid scratch requirements. It might be, for instance, that we have found many sets that produce 3-cell anti-phase activity, but the strict duration requirements do not consider them scratches.

It might be advantageous to deviate slightly from certain biological restrictions in future work. Requiring that the cells activate in a certain order, but with any relative duration, can still address the question of how networks contribute to produce a particular pattern. Alternatively, aiming to reproduce rhythms of a particular frequency (possibly based on averaged data from many animals under a certain stimulus strength) would allow quantitative comparisons of parameter performance based on a desired cost function. Finally, reducing the complexity of our current models by allowing inhibition to be a Heaviside function of the neuron activity would greatly facilitate analysis. However, we have seen that certain dynamics are facilitated by inhibition from weak neurons (recall that inhibition from $i_1$ was necessary to produce scratch under the UnitaryS parameter set, even though its activity level was small), so it would be interesting to see how that reduction would affect our work.

## 3.0   A DYNAMICAL SYSTEMS ANALYSIS OF A LOCOMOTOR MODEL

A certain network of neurons in the mammalian spinal cord can, in isolation, generate activity consistent with a locomotor rhythm [12, 28, 58] and has thus been dubbed the locomotor central pattern generator (CPG). In an intact animal, CPG outputs control limb movements through the activation of motoneurons that drive muscle activity, with muscle afferent signals to the spinal circuits forming a feedback control loop. Although this locomotor system has been the subject of extensive past work, fundamental open questions about its structure and dynamics remain. In this third chapter, we will introduce a neuromechanical locomotor model that can be used to study locomotion. Given a constant input, a group of neurons oscillates and drives the activity of a pendular limb, and afferent feedback from muscles closes the loop. This system operates through feedback control, exhibiting markedly different performances under the presence and absence of feedback. Changes in the constant input parameter (drive) controls the frequency of oscillations, and the model is able to exhibit stable gait over a wide range of drives. We will present a thorough analysis of this model, explaining how the presence of feedback influences the dynamics of the CPG, overriding an intrinsic oscillatory mechanism to produce oscillations at a particular relationship in the limb cycle. Using insights from this analysis, we reduce the model to a more tractable form and prove it exhibits a limit cycle, drawing conclusions about its uniqueness from constraints seen in the phase plane.

As a starting point in this endeavor, we first investigate how the model produces periodic oscillations. To this end, we use slow-fast decomposition analysis to understand the CPG dynamics without consideration of its effect on limb segment activity, contrasting its dynamics without afferent feedback, which can remain oscillatory given sufficient supra-spinal drive, to that observed when excitatory feedback from muscle afferents is incorporated, which

67

broadens the range of drive values over which oscillations occur (Section 3.2). This analysis yields different criteria for the existence of oscillations in either case, and illuminates why the model is more robust when feedback is present. Without feedback, analysis reveals that the intrinsic structure of a set of rhythm generator ($RG$) neurons within the CPG allows oscillations to occur through $RG$ escape for a sufficiently large supra-spinal drive. When feedback is present, however, oscillations occur through a different mechanism, namely the escape of CPG inhibitory interneurons ($In$) from the silent phase, which happens when feedback drives $In$ voltage above a certain threshold. We show that this threshold condition is met when a particular relationship between limb angle and velocity, which is independent of drive, is realized, and this observation allows us to identify transition curves in limb phase space that indicate where switches between the extensor and flexor activities produced by the CPG will occur.

Equipped with insights from this analysis, we propose a reduced model that maintains key model features and study conditions for the existence of stable periodic orbits in the reduced model setting (Section 3.3). To complete our existence argument, we use a novel version of the Melnikov function, adapted for discontinuous systems. Our analytical steps highlight the mechanism by which the oscillation can be lost if drive is reduced too far and also reveal the presence of a strong contraction in the phase space associated with the limb segment, which occurs during a particular phase of each locomotor oscillation. This work was published in [75] and [76], but has been modified for readability.

## 3.1   MODEL DESCRIPTION

This study focuses on a simplified neuromechanical model of locomotion originally proposed by Markin et al. [46], which we now describe. A schematic diagram illustrating model components and the connections between them is shown in Figure 23A.

The multi-level central pattern generator (CPG) consists of a half-center rhythm generator ($RG$) composed of flexor neurons ($RG$-$F$) and extensor neurons ($RG$-$E$) projecting to corresponding pattern formation neurons ($PF$), $PF$-$F$ and $PF$-$E$, and to inhibitory
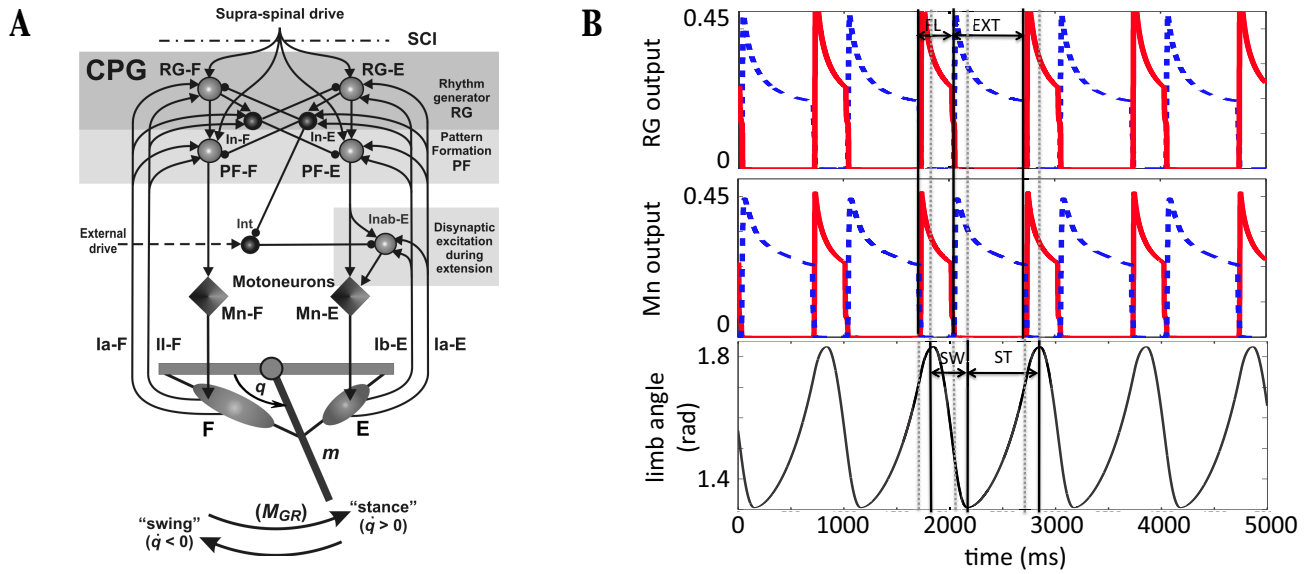
**Figure 23:** *Components and basic behavior of the neuromechanical model. (A) The two-level spinal CPG (comprised of $RG$, $In$, and $PF$ located in the top shaded rectangle) receives tonic supra-spinal drive and generates a basic locomotor rhythm providing alternating activation of flexor and extensor motoneurons ($Mn$-$F$ and $Mn$-$E$). All interneurons are represented by spheres (light: excitatory, dark: inhibitory) and motoneurons by diamonds. Excitatory and inhibitory synaptic connections are indicated by arrows and small circles, respectively. The motoneurons activate antagonistic muscles that drive a single-joint limb, and feedback from muscle afferents closes the loop. (B) Sample model activity shows the output of the rhythm generator neurons (RG, top), motoneurons (Mn, middle), and limb angle (bottom). Flexor related activity is plotted with a solid red line, with active phase duration indicated by the segment labeled FL, and extensor related activity is plotted with a dashed blue line, with active phase duration indicated by the segment labeled EXT. Note that flexor and extensor phases are shifted relative to swing and stance phases (SW and ST, bottom). (A) Modified from Markin et al. [46], with permission from the New York Academy of Sciences.*

interneurons $(In)$, $In$-$F$ and $In$-$E$, which mediate reciprocal inhibition between the flexor and extensor sides. The $RG$s and $PF$s receive a tonic drive $(d)$ that we refer to as supraspinal to indicate that biologically this signal originates outside of the spinal cord. Given sufficient supra-spinal drive to yield CPG oscillations, the $PF$ output induces alternating activity in flexor and extensor motoneurons $(Mn$-$F$ and $Mn$-$E)$, which correspondingly activate two antagonistic muscles, the flexor $(F)$ and extensor $(E)$, controlling a simple one-joint limb and providing continuously time-varying excitatory afferent feedback signals to the CPG. An additional circuit of interneurons $(Int$ and $Inab$-$E$ in Figure 23A) provides a disynaptic pathway from $PF$-$E$ to $Mn$-$E$ [1, 2].

Each neuron in the model is intended to represent a synchronized neural population, with the voltage drop across the membrane denoted as $V$ (voltage) and the synaptic output of that neuron calculated using the nonlinear transformation

$$f_C(V) = \begin{cases} 1/(1 + \exp(-(\frac{V - V_{1/2}}{k}))) & \text{if } V \geq V_{th}; \\ 0 & \text{otherwise,} \end{cases}$$

where $V_{1/2} = -30$ mV, $k = 3$ mV for $Mn$ and $k = 8$ mV for all other neurons, and $V_{th} = -50$ mV. This smooth gain function $f_C$ represents the strength of the output of a neuron or population, which scales heuristically with $V$. Based on the relation of its voltage to a threshold $V_{th} = -50$ mV, the state of a neuron is classified as either active (when $V \geq V_{th}$) or silent (when $V < V_{th}$). The $RG$, $PF$, and $Mn$ models incorporate some voltage-gated ionic currents. These currents in $RG$-$F$ and $RG$-$E$, in combination with the reciprocal inhibition between these neurons (via the inhibitory $In$-$F$ and $In$-$E$), define the rhythm generation in the CPG [65, 19]. The $RG$, $PF$, and $Mn$ dynamics are each described by a conductance-based system of two first order ordinary differential equations

$$\begin{aligned} C\dot{V}_i &= -I_{NaP}(V_i, h_i) - I_K(V_i) - I_{Leak}(V_i) - I_{SynE}(V_i) - I_{SynI}(V_i), \\ \dot{h}_i &= \frac{h_\infty(V_i) - h_i}{\tau_h(V_i)}, \end{aligned} \tag{3.1}$$

and the interneurons $(In$-$F$, $In$-$E$, $Int$, and $Inab$-$E)$ are each described by a single first order equation,

$$C\dot{V}_i = -I_{Leak}(V_i) - I_{SynE}(V_i) - I_{SynI}(V_i). \tag{3.2}$$

70

$V_i$ refers to the voltage drop across the membrane of neuron $i$, $C$ is the membrane capacitance, $I_{NaP}(V_i, h_i) = \bar{g}_{NaP} m_{NaP} h_i (V_i - E_{Na})$ is the persistent sodium current with instantaneous activation $m_{NaP} = 1/(1+\exp(-\frac{V_i+47.1}{3.1}))$ and slow inactivation $h_i$, $I_K(V_i) = \bar{g}_K m_K^4 (V_i - E_K)$ is the potassium current with instantaneous activation $m_K = 1/(1+\exp(-\frac{V_i+44.5}{5}))$, $I_{Leak}(V_i) = \bar{g}_{Leak}(V_i - E_{Leak})$ is the leak current, and $I_{SynE}(V_i)$ and $I_{SynI}(V_i)$ denote excitatory and inhibitory inputs to neuron $i$ given by

$$I_{SynE}(V_i) = \bar{g}_{SynE}(V_i - E_{SynE})(\sum_j a_{j,i} f(V_j) + c_i d + \sum_k w_{k,i} fb_k), \qquad (3.3)$$

$$I_{SynI}(V_i) = \bar{g}_{SynI}(V_i - E_{SynI}) \sum_j b_{j,i} f(V_j), \qquad (3.4)$$

respectively. Equations (3.3) and (3.4) incorporate various extracellular inputs: the output $f(V_j)$ from the neurons presynaptic to neuron $i$, the constant supra-spinal drive $d$, and the sensory feedback terms $fb_k$. $a_{j,i}$ is the weight of the excitatory input from neuron $j$ to neuron $i$, $b_{j,i}$ is the weight of the inhibitory input from neuron $j$ to $i$, $c_i$ is a factor scaling the drive $d$ to neuron $i$, $fb_k$ denotes the $k$th feedback signal, and $w_{k,i}$ is the weight of feedback $k$ to neuron $i$. The values of the weights are provided in Table 7, and details on the feedback terms are provided at the end of this section. In the current equations above, $E_j$ and $\bar{g}_j$ denote the reversal potential and maximal channel conductance, respectively, of current $j$. Parameter choices associated with these currents are: $C = 20$ pF, $E_{Na} = 55$ mV, $E_K = -80$ mV, $E_{SynE} = -10$ mV, $E_{SynI} = -80$ mV for all neurons; $E_{Leak} = -64$ mV for the $RG$, $PF$, and $Mn$ and $E_{Leak} = -60$ mV otherwise; $\bar{g}_K = 4.5$ nS, $\bar{g}_{Leak} = 1.6$ nS, $\bar{g}_{SynE} = 10$ nS, $\bar{g}_{SynI} = 10$ nS, $\bar{g}_{NaP} = 3.5$ nS for $RG$, $\bar{g}_{NaP} = 0.5$ nS for $PF$, $\bar{g}_{NaP} = 0.3$ nS for $Mn$. The terms $h_\infty = 1/(1 + \exp(\frac{V+51}{4}))$ and $\tau_h = \tau_{hmax}\cosh(\frac{V+51}{8})$ in equation (3.1) are the voltage-dependent steady state inactivation level and inactivation time constant, respectively, of the evolution of the persistent sodium inactivation term, where $\tau_{hmax}=600$ ms. We note that $Int$ receives a separate external drive of strength 0.18.

The limb segment controlled by the CPG, which we hereafter refer to simply as the limb, is tethered at a joint and able to move in an angular direction relative to that joint. The

| | Target neurons | | | | | | | | | |
|---|---|---|---|---|---|---|---|---|---|---|
| | $RG\text{-}F$ | $RG\text{-}E$ | $In\text{-}F$ | $In\text{-}E$ | $PF\text{-}F$ | $PF\text{-}E$ | $Mn\text{-}F$ | $Mn\text{-}E$ | $Int$ | $Inab\text{-}E$ |
| Excitatory Connections, $a_{j,i}$ | | | | | | | | | | |
| $RG\text{-}F$ | | | 0.41 | | 0.70 | | | | | |
| $RG\text{-}E$ | | | | 0.41 | | 0.70 | | | | |
| $PF\text{-}F$ | | | | | | | 1.95 | | | |
| $PF\text{-}E$ | | | | | | | | 1.30 | | 0.35 |
| $Inab\text{-}E$ | | | | | | | | 0.82 | | |
| Inhibitory Connections, $b_{j,i}$ | | | | | | | | | | |
| $In\text{-}F$ | | 2.20 | | | | | 6.60 | | | |
| $In\text{-}E$ | 2.20 | | | | | 6.60 | | | 2.80 | |
| $Int$ | | | | | | | | | | 0.55 |
| Feedback Connections, $w_{k,i}$ | | | | | | | | | | |
| $Ia\text{-}F$ | 0.06 | | 0.27 | | 0.19 | | | | | |
| $II\text{-}F$ | 0.0348 | | 0.1566 | | 0.1102 | | | | | |
| $Ia\text{-}E$ | | 0.06 | | 0.44 | | 0.10 | | | | 0.16 |
| $Ib\text{-}E$ | | 0.066 | | 0.484 | | 0.11 | | | | 0.176 |
| Drive Connections, $c_i$ | | | | | | | | | | |
| Supra-spinal drive, d | 0.08 | 0.08 | | | 0.40 | 0.40 | | | | |
| External drive, $d_{Int}$ | | | | | | | | | 0.18 | |

**Table 7:** *Synaptic connection weights in the neuromechanical model.*

limb motion can be described by a system of two first order equations

$$\dot{q} = v$$

$$I\dot{v} = K\cos(q) - bv + M_F(q, v, V_{Mn\text{-}F}, t) - M_E(\pi - q, -v, V_{Mn\text{-}E}, t) + M_{GR}(q), \qquad (3.5)$$

where $q$ is the angle the limb makes with the horizontal and $v$ is its angular velocity. $I$ is the moment of inertia of the limb with respect to the suspension point, $K\cos(q)$ is the moment of the gravitational force, $b$ is the angular viscosity in the hinge joint, $M_F$ and $M_E$ are the moments of the muscle forces, and $M_{GR}(q)$ is the moment of the ground reaction force, given by

$$M_{GR}(q) = \begin{cases} -M_{GRmax}\cos(q), & v \geq 0, \\ 0, & v < 0. \end{cases}$$

This term is nonzero only during the *stance phase*, when the limb is swinging counterclockwise ($v \geq 0$), and is set to zero during the *swing phase*, when the limb swings in the clockwise direction ($v < 0$). Time traces of the moments is shown in Figure 24. In equation (3.5), $K = 0.5mgl_s$ and $I = ml_s^2/3$, where $m = 300$g denotes the mass of the segment, $l_s = 300$mm
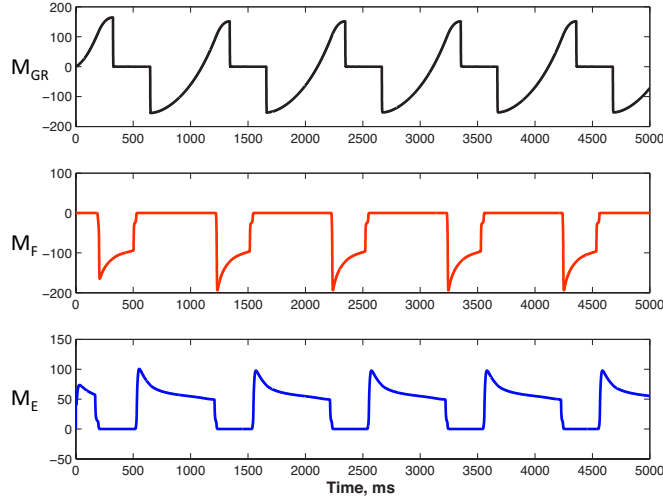
**Figure 24:** *Time courses of muscle moments. Top panel: moment of ground reaction, middle panel: moment of flexor force, bottom panel: moment of extensor force.*

denotes its length, $g = 0.0098$ mm$^2$/ms$^2$, $b = 18000$ g·mm$^2$/ms$^2$, and $M_{GRmax} = 585$N·mm.

The muscle moments are defined as $M_F = F_F h_F$ and $M_E = -F_E h_E$, where $F_F$ and $F_E$ refer to muscle forces and $h_F$ and $h_E$ denote the moment arms, the subscript indicating the flexor or extensor muscle. $F_E$ and $F_F$ are computed by $F = f_C(V)F_{max}F_l F_v$ where $f_C(V)$ is given in equation (3.1) and describes the output of $Mn$-$E$ or $Mn$-$F$, and $F_{max} = 72.5N$ and $37.7N$ for the flexor and extensor muscles, respectively. The muscle velocities are calculated as $v^m = vh_F$ for the flexor and $v^m = -vh_E$ for the extensor, where $v$ is the velocity of the limb and $h$ refers to muscle moment arms. The moment arm $h = (a_1 a_2 \sin(q))/L$ for the flexor muscle, where $L = \sqrt{a_1^2 + a_2^2 - 2a_1 a_2 \cos(q)}$ describes the muscle length. The same equations are used for the extensor muscle, with $q$ replaced by $\pi - q$. Here, $a_1$ denotes the distance between the suspension point and the muscle origin and $a_2$ denotes the distance between the suspension point and the muscle attachment to the segment, where $a_1 = 60$ mm and $a_2 = 7$ mm. $F_l = \exp(|\frac{l \cdot \beta - 1}{\omega}|^\rho)$ describes the force dependence on muscle length, where $\beta = 2.3, \omega = 1.6, \rho = 1.62$ and $l$ is the normalized muscle length corresponding to $F_l = 1$,

73

i.e. $l = L/Lopt$ for $Lopt = 68$ mm.

$$F_v = \begin{cases} \frac{b_1 - c_1 \cdot v^m}{v^m + b_1} & v^m < 0 \\ \frac{b_2 - c_2(l) \cdot v^m}{v^m + b_2} & v^m \geq 0 \end{cases}$$

describes the dependence of force on velocity, where $c_1 = 0.17$, $b_1 = -0.69$, $b_2 = 0.18$, and $c_2(l) = -5.34l^2 + 8.41l - 4.7$.

Muscle afferents provide length/velocity-dependent (type $Ia$ from both muscles and type $II$-$F$ from the flexor) and force-dependent (type $Ib$-$E$ from the extensor) feedback to the CPG through additional excitation to the homonymous neurons. The nonlinear feedback from the extensor and flexor muscle afferents provides excitatory inputs to $RG$, $In$, $PF$, and $Inab - E$ that control the timing of phase transitions at the $RG/In$ level and the excitability of the $PF$ neurons. Sensory feedback from the extensor muscle also accesses the additional $Int/Inab$-$E$ circuit yielding a net excitation of $Mn$-$E$ during extension (see Figure 23A). The feedback equations are derived from Prochazka [53, 54] as:

$$Ia = k_{IaV} v_{norm}^{\rho_v}(q, v) + k_{dIa} d_{norm}(q) + k_{EMG_{Ia}} f_C(V_{Mn}) + C_{Ia};$$

$$Ib\text{-}E = k_{Ib} F_{norm}(V_{Mn\text{-}E});$$

$$II\text{-}F = k_{dII} d_{norm}(q) + k_{EMG_{II}} f_C(V_{Mn\text{-}F}).$$

$v_{norm}$ denotes the normalized muscle velocity ($v^m/L_{th}$), $d_{norm}$ is the normalized muscle lengthening: $(L - L_{th})/L_{th}$ if $L \geq L_{th}$, 0 otherwise, with $L_{th} = 59$mm, and $F_{norm}$ is the normalized muscle force: $(F - F_{th})/F_{max}$ if $F \geq F_{th}$ and 0 otherwise, with $F_{th} = 3.38$ N. As mentioned above, the function $f_C(V)$ given in equation (3.1) describes the output of the motoneurons, while the remaining terms in the feedback functions are constants that take the values $\rho_v = 0.6$, $k_{Iav} = 6.2$, $k_{dIa} = 2$, $k_{EMG_{Ia}} = 0.06$, $C_{Ia} = 0.26$, $k_{Ib} = 1$, $k_{dII} = 1.5$, and $k_{EMG_{II}} = 0.06$. Linear combinations of feedback terms are fed into each side of the model: $Ia$-$F$ and $II$-$F$ feedbacks to the flexor side and $Ia$-$E$ and $Ib$-$E$ to the extensor side. In equation (3.1), we denote the feedback to neuron $i$ as $\sum_k w_{k,i} fb_k$, which we will henceforth abbreviate as $FB_i$. For extensor neurons,

$$FB_i = w_{Ia\text{-}E,i} Ia\text{-}E + w_{Ib\text{-}E,i} Ib\text{-}E \tag{3.6}$$

74

for $i \in \{RG\text{-}E,\ PF\text{-}E, In\text{-}E,\ Inab\text{-}E\}$. For flexor neurons,

$$FB_i = w_{Ia\text{-}F,i}Ia\text{-}F + w_{II\text{-}F,i}II\text{-}F \tag{3.7}$$

for $i \in \{RG\text{-}F,\ PF\text{-}F,\ In\text{-}F\}$.

Figure 23B shows an example of the time course of activity of $RG$ and $Mn$ for both the flexor and extensor sides, and the corresponding limb angle. Note that a switch in which side of the CPG is active, and hence a switch between flexor and extensor activation, does not instantaneously change the direction of motion of the limb. Since the definition of stance and swing phases is based on the direction of limb motion (and correspondingly the presence or absence of ground reaction force), these phases are shifted relative to the $F$ and $E$ phases. Thus, we can define eSwing, eStance, fSwing, and fStance subphases (which will be important in later sections), where in each subphase name, the first letter denotes the active motoneuron ('f' for flexor, 'e' for extensor) and the subsequent string indicates whether the limb is in the swing or stance phase. One cycle through these phases defines a locomotor cycle in the model. Without feedback, the limb is considered to be immobilized, so when feedback is absent, we will define the duration of the "fictive locomotor cycle" by the period of the CPG oscillations, formed by a single extensor and flexor phase (see Figure 26A).

Figure 25 shows the time course of $Ia - E, II - F$, and $Ib - E$ feedback along with $RG$ activity. It is important to note that the feedback to a neuron increases during its silent phase and decreases during its active phase, with the exception of force-dependent $Ib\text{-}E$ feedback, which is only active when $RG\text{-}E$ is. This information will be utilized in Section 3.2, where the dynamic mechanisms underlying oscillations in the model (e.g., Figure 23B) are described. Figure 26 illustrates the dependence that the flexor, extensor, and overall locomotor cycle phase durations have on supra-spinal drive when feedback is absent (Figure 26A) and present (Figure 26B). In the absence of afferent feedback (also known as the fictive locomotion state), frequency increases are obtained by an equivalent decrease of both flexor and extensor durations. When afferent feedback is present, however, the limb oscillates and frequency increases occur through a decrease in stance phase duration only, with the swing phase duration remaining relatively constant. In addition, the presence

75
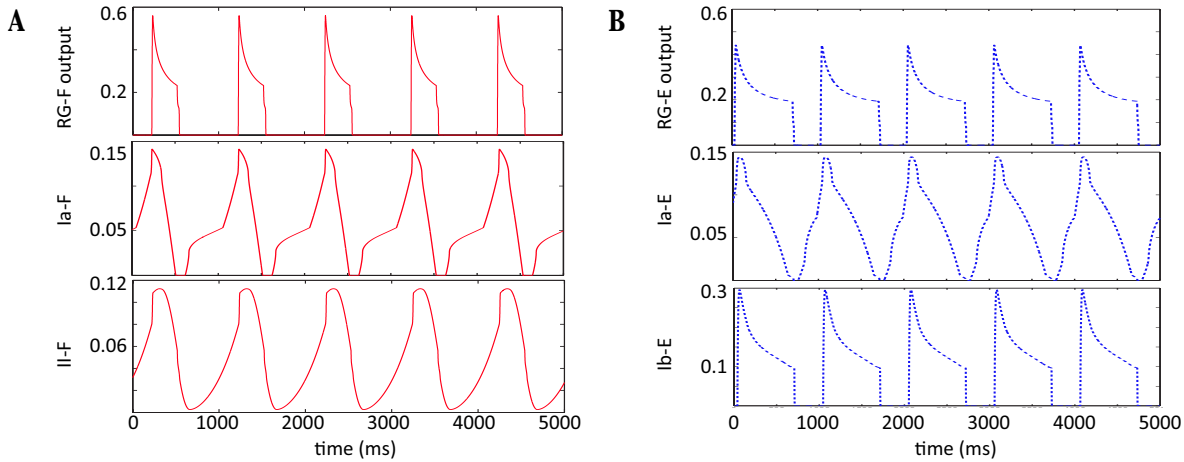
**Figure 25:** *Time courses of RG output ($f_C(V)$) and feedback activity. (A) RG-F, Ia-F, II-F output (red solid) in top, middle, and bottom panels, respectively. Feedback signals Ia-F and II-F are fed to flexor neurons, increasing while RG-F is inactive and decreasing while RG-F is active. (B) RG-E, Ia-E, Ib-E output (blue dashed) in top, middle, and bottom panels, respectively. Feedback signals Ia-E and Ib-E are fed to extensor neurons. Similarly to the flexor side, Ia-E increases while RG-E is silent and decreases while RG-E is active. Ib-E is force-dependent and is only active during the active phase of RG-E.*

of feedback increases model robustness, since the CPG oscillates over a wider range of supraspinal drive, compared to the case when feedback is absent. In the lower half of Table 1, we present a list of terms that are commonly used in this chapter.

## 3.2 CPG MECHANISMS DIFFER IN THE MODEL WITH AND WITHOUT FEEDBACK

Given sufficient drive, model neurons in this system form a CPG, able to produce rhythmic alternation of extensor and flexor components in absence of feedback. In the open loop configuration, drive changes vary the CPG output frequency by symmetric changes in both flexor and extensor durations. When limb feedback is incorporated, however, the model exhibits an asymmetric output where limb frequency is controlled by changes in

76
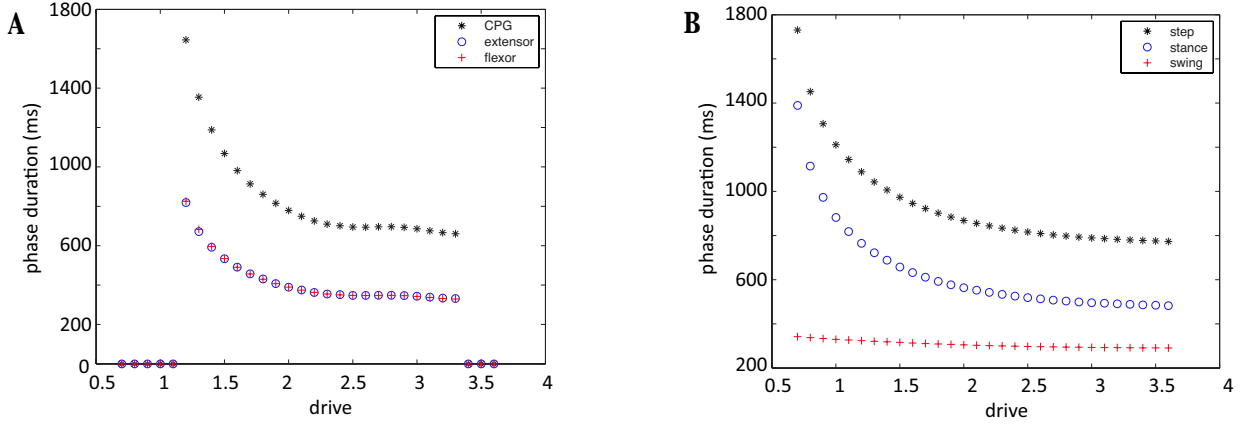
**Figure 26:** *Control of the locomotor speed by a supra-spinal drive applied identically to both half-centers in (A) absence and (B) presence of feedback. In the literature, the stance phase is considered synonymous with the extensor phase (similar for the swing and flexor phases). (A) In the absence of feedback, extensor (blue circles) and flexor (red plus signs) phase durations sum to the CPG cycle period (black stars) and change identically as drive varies. (B) In the presence of feedback, step cycle duration (black stars) instead varies asymmetrically with drive, exhibiting decreases in the duration of the stance phase (blue circles), at a relatively constant swing duration (red plus signs). In addition, the CPG oscillates over a wider (particularly lower) range of drives, compared to the model without feedback.*

the stance phase duration only (corresponding to variations in extensor duration alone, see Figure 26). As a first step towards explaining the asymmetric response to drive changes exhibited in the closed-loop configuration, we begin by analyzing the activity of the CPG's rhythm generator, which is comprised of *RG*s described by system (3.1) and *In*s described by equation (3.2). Because the persistent sodium inactivation time constant $\tau_h(V)$ is large over the relevant voltage range (see Section 3.1 for details), system (3.1) is essentially of the form $\dot{V} = F(V, h, I(t)), \dot{h} = \epsilon G(V, h)$, where $\epsilon$ is a small parameter and $I(t)$ denotes time-dependent excitatory/inhibitory input from other neurons and feedback. A dynamical system in this form is called a slow-fast system, because $h$ evolves on a much slower timescale than $V$ due to the size of $\epsilon$. Before discussing the interactions of two neurons with these dynamics, in Section 3.2.1 we will first consider the dynamics of a single neuron described by slow-fast equations with a fixed input $I$. We will see that the activity of this neuron can be completely determined from the location of intersection of its nullclines in the $(V, h)$ phase plane. Once we understand the dynamics of a single neuron receiving a fixed input, we can

analyze how our set of connected neurons coordinate their activity to generate a model oscillation when feedback is absent (Section 3.2.2) and when feedback is present (Section 3.2.3), such that the levels of input to the neurons varies in time. By illustrating the details of these mechanisms, we can explain how the model is able to oscillate at a wider drive range when feedback is present, and why strengthening this feedback supports an increase in locomotor frequency.

### 3.2.1  Intrinsic dynamics of model $RG$s

Consider system (3.1) as $\dot{V} = F(V, h, I), \dot{h} = \epsilon G(V, h)$, where $I$ is some fixed constant and $\epsilon$ is a small positive parameter. Due to the small size of $\epsilon$, $h$ is expected to evolve much more slowly than $V$ except where $|F|$ is small. When such a separation of timescales is present, the nullclines of the system are particularly helpful for understanding its dynamics, as we will explain below. The $V$-nullcline consists of the set of $(V, h)$ that satisfy $\dot{V} = F(V, h, I) = 0$. Given the definition of $F$, when the $V$-nullcline is a drawn in the $(V, h)$ phase plane, $F > 0$ above this curve and $F < 0$ below this curve (for an example, see Figure 27). Under certain input strengths, the $V$-nullcline exhibits a cubic shape (see Figures 27A and 27B), composed of three (left, middle, and right) branches. The left and middle branches meet at a local maximum, which we will refer to as the left knee, and the middle and right branches connect at a local minimum, which we refer to as the right knee. The $h$-nullcline (the set of $(V, h)$ that satisfy $\dot{h} = G(V, h) = 0$) is also important. When drawn in the phase plane, the $h$-nullcline is a non-increasing sigmoid, with $G > 0$ below and $G < 0$ above this curve.

When a neuron is described by a model with dynamics on two disparate timescales, we can simplify the analysis of its behavior by reducing the full system to two subsystems, each on its own timescale. First we consider the limit where $\epsilon$ goes to 0 and obtain the fast subsystem (FS): $\dot{V} = F(V, h, I), \dot{h} = 0$. Solutions for the fast subsystem have $h$ fixed as a constant with flow determined by the dynamics of $V$. If we instead perform a change of variables and let $\tau = \epsilon t$, and *then* let $\epsilon$ go to 0, we obtain the slow subsystem (SS): $0 = F(V, h, I), h' = G(V, h)$, by using the chain rule and canceling $\epsilon$ in the $h$ equation (′ denotes differentiation with respect to $\tau$). Solutions to the slow subsystem lie on the $V$-nullcline and flow according to
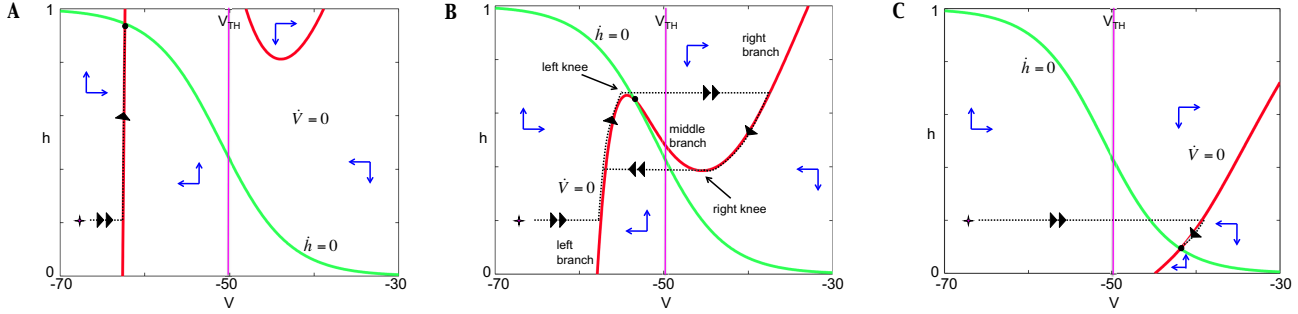
**Figure 27:** *Neuron activity for three different levels of input. In each panel, the $V$-nullcline is shown in red, the sigmoid shaped $h$-nullcline in green. The location of their intersection determines the activity of the neuron. The trajectory is shown with a thick black dotted line from an initial condition indicated by a star. Threshold is indicated with a magenta vertical line, located at $V = V_{th}$=-50 mV. Double arrows indicate motion on the fast timescale, single arrows on the slow timescale. Blue arrows indicate the direction of the vector field, and the black dot indicates the critical point for the system in each case. (A) The neuron remains at a silent state for all time when the nullclines intersect on the left branch of the $V$-nullcline. (B) When the nullclines meet on the middle branch of the $V$-nullcline, periodic activity can occur since both knees are accessible. (C) Tonic activity results from the configuration in which nullclines intersect on the right branch of the $V$-nullcline.*

the dynamics of $h$, with $V = V(h)$ such that $F(V(h), h, I) = 0$. This evolution occurs on a much slower timescale than that of the fast subsystem due to the change of time variable. An approximate solution to the full system is formed as an appropriate concatenation of solutions of the fast and slow subsystems, where the subsystem to be solved at a particular time depends on the solution's location in phase space at that time. Indeed, consider an initial condition starting away from the $V$-nullcline. Since $F(V, h, I) \neq 0$, i.e. the conditions of (SS) are not satisfied, the dynamics of the system are described by (FS). According to this subsystem, $h$ is fixed and $V$ evolves toward a stable critical point of (FS). As can be seen by examination of the vector field (Figure 27), each point on the left and right branches is a stable critical point of (FS), since $\dot{V} > 0$ for $V$ below the left branch and $\dot{V}$ switches sign each time a branch is crossed. In the limit as $t \to \infty$, $F(V, h, I) = 0$ is satisfied and (SS) can be solved to obtain the next segment of the solution.

Overall, the activity of each neuron depends completely on the location of the intersection between the $V$ and $h$ -nullclines, which is a critical point of the full system. Figure 27 shows

nullcline configurations for input values that cause the nullcline intersection point to lie on: the left branch of the $V$-nullcline in Figure 27A, the middle branch in Figure 27B, and the right branch in Figure 27C. Consider an initial condition in the lower left corner of the phase plane as shown in Figure 27A. Since $F(V, h, I) \neq 0$, the trajectory approaches the nearest stable critical point of (FS), which lies on the left branch of the $V$-nullcline. From this critical point, the dynamics of (SS) yield a trajectory that travels up the left branch of the $V$-nullcline, since $h' > 0$ in this region. As time increases, this trajectory approaches a point $(V_s, h_s)$ that satisfies $F(V_s, h_s) = 0, G(V_s, h_s) = 0$, namely a critical point of the $(V, h)$ system that lies below the activation threshold. This neuron will remain in this silent state for all time.

If instead the nullcline is configured as in Figure 27B, the trajectory would again follow first the (FS) then the (SS) dynamics until it travels slightly above the left knee of the $V$-nullcline. At that time, the (SS) conditions are not met (once we leave the $V$-nullcline, $F(V, h, I) \neq 0$), so $V$ evolves to a stable state with fixed $h$ according to (FS). This point lies on the right branch of the $V$-nullcline, so as $t$ increases the trajectory crosses activation threshold and enters the active state. The trajectory evolves according to (SS) with decreasing $h$ on the $V$-nullcline since it now lies to the right of the $h$-nullcline. An analogous transition to the silent phase occurs when the trajectory reaches the right knee of the $V$-nullcline. With this configuration a neuron is an intrinsic oscillator, since it spends time in both the silent and active phases. The existence of a relaxation oscillator in this case can be proven rigorously using the Poincaré-Bendixson theorem.

Finally, Figure 27C shows a nullcline configured with the critical point lying on the right branch of the $V$-nullcline. From the starting point shown, the trajectory immediately jumps across synaptic threshold to the right branch of the $V$-nullcline according to (FS) and evolves in a direction of decreasing $h$ according to (SS). In this case, however, the trajectory encounters a critical point of the full system. This state lies above activation threshold, thus the neuron remains in an active state for all subsequent time.

This discussion details the possible activity patterns of a single neuron with a fixed input, but in system (3.1), the neurons receive input from sources that vary in strength over time, which means that their nullclines are constantly evolving. For instance, a neuron that

is stuck in the silent regime can become active if it receives sufficiently strong excitation (or conversely, sufficiently weak inhibition) to lower its $V$-nullcline and shift the critical point from the left to the middle branch. Analogously, a neuron with a tonic nullcline configuration could evolve to the silent phase if its excitatory input decreases sufficiently, raising the nullcline so that the neuron can access the right knee [62].

When coupled neurons generate a rhythm through a combination of intrinsic dynamics and coupling-induced nullcline adjustments, we can distinguish different classes of transition mechanisms by which different neurons become active or silent. For instance, a transition might occur via an inhibited cell reaching its left knee and "escaping" from the silent phase. Once it becomes active, it may inhibit previously active cells, possibly forcing them to become silent. This transition mechanism is denoted as escape. Conversely, if an active cell reaches its right knee, then it can jump down from the active to the silent phase. Once it crosses below synaptic threshold, it "releases" the silent cell from inhibition (allowing the inhibited cell to become active). This transition mechanism is denoted as release [80, 72, 19].

In the following sections, we discuss the different mechanisms causing transitions in the CPG in the case when feedback is absent and the case when it is present.

### 3.2.2 Without feedback, CPG transitions occur through $RG$ adaptation and escape

Our simulations show that oscillations in the CPG without feedback occur via escape controlled by $RG$. Details of the transition from $RG\text{-}E$ silent to $RG\text{-}E$ active are shown in Figure 28, and the $F$ transition is analogous. In the top panel of each figure, the dynamics of $RG\text{-}F$ and $RG\text{-}E$ are tracked in phase space. In the bottom panel of each figure, the corresponding voltages of $In\text{-}F$ and $In\text{-}E$ are indicated. Since feedback is absent, the voltage of $In$ is completely slaved to the activity of $RG$; it remains at a silent rest state of equation (3.2) given by the leak reversal potential when $RG$ is silent but is excited above threshold after $RG$ becomes active. Also, without feedback, the only time-varying input to $RG$ comes from inhibition from $In$.

Starting from its position in Figure 28A, the $h$ variable of $RG\text{-}F$ decreases in slow time.
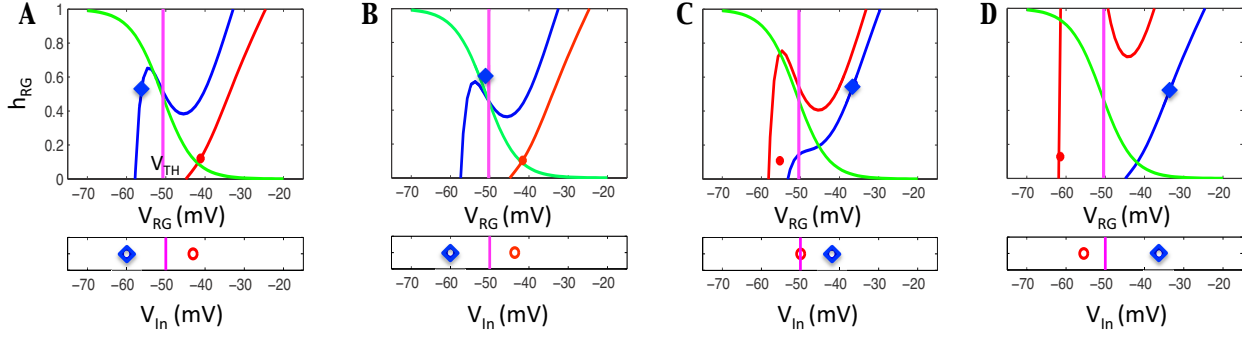
**Figure 28:** *Frame by frame depiction of the escape mechanism for the model without feedback. In the top boxes RG-F and RG-E positions are plotted at various timepoints with their relevant nullclines in $(V_{RG}, h_{NaPRG})$ space. The corresponding voltages of In-F and In-E are tracked in the lower boxes. For all neurons and V-nullclines, red indicates flexor and blue indicates extensor, the h-nullcline is shown in green, and the voltage threshold is indicated in magenta. (A) Inhibition from In-F decreases over time, lowering RG-E's V-nullcline until the left knee can be reached. (B) RG-E hits the knee and jumps across threshold. (C) Excitation from RG-E pushes In-E across threshold. In-E begins inhibiting RG-F which raises RG-F's V-nullcline, causing RG-F to jump below threshold. This decreases excitation to In-F, which also begins to fall below threshold. (D) RG-F and RG-E have switched dominance, as have In-F and In-E.*

Due to the slope of the $V$-nullcline, the voltage of $RG\text{-}F$ decreases, which weakens the excitation from $RG\text{-}F$ to $In\text{-}F$ and correspondingly reduces the inhibition from $In\text{-}F$ to the $RG\text{-}E$ (see equations (3.3),(3.4) for relevant synaptic currents). This reduction in inhibition is a form of adaptation that facilitates phase transitions (e.g., [19]). During this time, $RG\text{-}E$ travels up its inhibited $V$-nullcline (which lowers as the output from $In\text{-}F$ decreases) until it reaches the left knee of the relevant $V$-nullcline. The rest of the dynamics shown in Figure 28B-28D occur on the fast timescale. In Figure 28B, $RG\text{-}E$ escapes and jumps toward the right branch, exciting its corresponding $In\text{-}E$ as it crosses the synaptic threshold. The newly active $In\text{-}E$ provides partial inhibition to the opposing $RG\text{-}F$, causing a change in its $V$-nullcline. Due to this change, $RG\text{-}F$ ends up below the right knee of the $V$-nullcline and jumps to the left branch of its nullcline, crossing below the synaptic threshold as it does so (Figure 28C). Without excitation from $RG\text{-}F$, $In\text{-}F$ falls below threshold as well and stops inhibiting $RG\text{-}E$. As the fast time $t \to \infty$, $RG\text{-}F$ is fully inhibited from $In\text{-}E$ (Figure 28D). This sequence represents one half-cycle, from the onset of $RG\text{-}F$ activation to

the onset of $RG$-$E$ activation, after which the neurons evolve on the slow timescale again. We note that with no feedback, for all drives considered [46], the first derivative of the nullcline of the active $RG$ neuron is always positive, so transitions by pure intrinsic release, in which an active neuron reaches a right knee and falls silent on its own, cannot occur.

The transitions by adaptation-facilitated escape seen in the absence of feedback lead to a decrease in phase durations when excitation, i.e. drive, is increased [74, 68]. Since both transitions, $E$ to $F$ and $F$ to $E$, occur via this mechanism, we expect both the flexor and extensor durations to decrease as drive is increased as shown in Figure 26A. Furthermore, this transition mechanism limits the range of drives that produce oscillations. If drive is too small, the critical point for the inhibited nullcline will lie on the left branch, and the silent neuron will be unable to complete a transition to become active. Thus, the observation that transitions occur by $RG$ escape has allowed us to identify the bifurcation event underlying the loss of oscillations with reductions in drive in the CPG without feedback.

Given this insight, we can now address the following question: Assuming that one $RG$ is active and the other silent, for which drives will the system oscillate? As outlined above, we must determine the equation for the inhibited nullcline, and locate the position of the critical point for the $(V, h)$ system, to answer this question. To do this, we fix drive, and in the absence of excitatory feedback, the active $RG$ nullcline is completely determined. We compute the steady state of this neuron, which corresponds to the minimum inhibition level that it indirectly provides to the opposing $RG$. If the inhibited $V$ and $h$ nullclines intersect on the left branch of the $V$-nullcline for this inhibition value obtained at this particular drive, then the neuron will be unable to escape.

Using the implicit function theorem, we find an explicit equation $h = h_c(V)$ for the inhibited $RG$ nullcline under the drive and inhibition pairing we described above and solve $h_c(V) = h_\infty(V)$ to find an expression for the voltage of the critical point, $V_{ip}$, where $h = h_\infty(V)$ is the equation for the $h$-nullcline. Separately, we calculate the voltage of the left knee, which satisfies $h_c'(V) = 0, h_c''(V) < 0$, where $\prime$ denotes differentiation with respect to $V$. We will denote this as $V_{lk}$. Then, if $V_{ip} < V_{lk}$, the intersection point lies on the left branch of the $V$-nullcline, which prohibits escape. We find that the silent $RG$ can begin to escape for inhibition and drive pairings larger than $d = 1.13$, which concurs with Figure 26A, where

oscillations are seen for $d$=1.2 and larger.

For very large drives, on the other hand, the oscillations in the CPG break down in a different manner. As drive is increased, the inhibited $RG$ nullcline can become sufficiently lowered such that almost the entire nullcline lies to the right of the synaptic threshold, $V_{th}$. Thus, the active periods of $RG$ begin to overlap, which represents the loss of a coordinated oscillation.

We also note that for relatively large drives, $PF$ can escape prior to the transition at the $RG$ level, and the $PF$ $V$-nullclines can move above synaptic threshold, such that $PF$ can remain active for the entire oscillation cycle. However, this does not affect our definitions of phase durations, since these are calculated based on $RG$ activity in this no-feedback case, nor does it affect limb dynamics, since the limb is considered as immobilized in this case.

### 3.2.3 Presence of feedback induces CPG oscillations through $In$ escape mechanism and defines important system transition curves

The dynamics becomes more complicated when the CPG neurons receive excitatory input from sensory feedback. This feedback depends nonlinearly on the position and velocity of the limb as well as the output of the motoneurons, which makes it difficult to pinpoint whether a transition based on the intrinsic dynamics of an $RG$ may be possible. Further, since feedback is also fed to $In$, their states are no longer slaved to $RG$ activity. In fact, we observe that as feedback increases, each $In$ can cross threshold independently of the $RG$ that excites it, which results in oscillations featuring a different transition mechanism than in the previous case. We show details of this mechanism, from $RG$-$E$ silent to $RG$-$E$ active, in Figure 29, and again, the opposite transition is analogous.

Comparing Figure 28A with Figure 29A, we can see that adding excitatory feedback to the system has the net effect of raising the position of the inhibited $V$-nullcline. This outcome may seem counterintuitive, since simply receiving more excitation should lower the silent neuron's $V$-nullcline; however, the strength of the inhibition the silent neuron receives is also stronger, since increasing excitation to the active neuron allows it to inhibit the silent neuron more strongly. The effect of this stronger inhibition, despite the stronger excitation

84

from feedback signals, is that the $V$-nullcline for the silent $RG\text{-}E$ is higher in the feedback case than in the case without feedback, for the same drive value. Hence, the $RG\text{-}E$ equations have a critical point in the silent phase, on the left branch of their $V$-nullcline, while the $RG\text{-}F$ equations have a critical point in the active phase, on the right branch of their $V$-nullcline, as illustrated in Figure 29A. Given this situation, without any change in input, the $RG$ will become deadlocked at steady states, unable to trade dominance, for the same drive value shown in Figure 28. Crucially, however, $In\text{-}E$ integrates sufficient input from excitatory feedback that it can cross the synaptic threshold and begin to inhibit $RG\text{-}F$ on its own (Figure 29B). This inhibition raises the $RG\text{-}F$'s $V$-nullcline, such that its voltage drops on the fast timescale, which reduces the voltage of $In\text{-}F$ (Figure 29C; note that the rise in $In\text{-}E$ inhibitory output is not dependent on a change in $RG\text{-}E$ up to this time). This change updates the $RG\text{-}E$ nullcline, since the inhibition it receives from $In\text{-}F$ is reduced, and eventually the nullcline lowers such that $RG\text{-}E$ can reach the left knee and jump to the right branch. As it passes through threshold, $RG\text{-}E$ provides additional excitation to the already active $In\text{-}E$ (Figure 29B). During this transition, $In\text{-}F$ shuts down completely, so $RG\text{-}E$ converges to the right branch of the uninhibited nullcline, and $RG\text{-}F$ settles on the left branch of the fully inhibited nullcline (Figure 29D).

Note that in this case, the active $RG$ neuron receives more positive input (drive plus feedback) than in the case without feedback, and hence again, a departure from the active phase by the active $RG$ neuron and associated release of the silent neuron cannot occur without some other event initiating the transition first. In some cases, the active $In$ may reach low enough voltages that the inhibitory signal to the silent side may become significantly sub-maximal. Still, while this reduction in inhibition may facilitate switching, in the end it is the escape of the silent $In$ that causes the full dominance switch.

Now that we have identified what event is responsible for each transfer of dominance in the CPG, we can understand the range of drives over which oscillations occur by exploring how and when that event occurs. For the silent $In$ to become active, it must cross the activation threshold. Since its corresponding $RG$ is silent when it first escapes, the only excitation it receives is from feedback, which increases throughout the inactive phase of a neuron as noted in Section 3.1. The level of excitation required for $In$ to cross threshold can
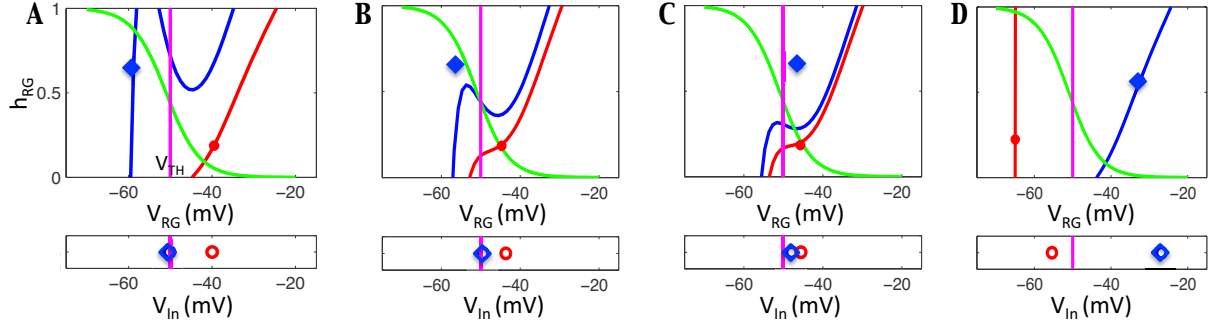
**Figure 29:** *Frame by frame depiction of the In escape mechanism when feedback is present in the model. In the top boxes RG‑F and RG‑E positions are plotted at various timepoints on their relevant nullclines in $(V_{RG}, h_{NaPRG})$ space. The corresponding voltages of In‑F and In‑E are tracked in the lower boxes. For all neurons and V‑nullclines, red indicates flexor and blue indicates extensor, the h‑nullcline is shown in green, and the voltage threshold is indicated in magenta. (A) Feedback increases excitation to In‑E, allowing it to reach threshold independently from RG‑E. (B) In‑E begins to inhibit RG‑F, which raises the RG‑F's V‑nullcline(red). This change causes the voltage of In‑F to decrease, yielding less inhibition to RG‑E and thus lowering RG‑E's V‑nullcline (blue). (C) RG‑E is now able to jump to the right branch, crossing threshold and further exciting In‑E as it does so. (D) RG‑F falls below threshold after receiving full inhibition from In‑E. Without excitation from RG‑F, In‑F falls below threshold as well.*

be obtained by solving for the steady state of silent $In$ and setting this value equal to $V_{th}$. The steady state satisfies:

$$V_{In\text{-}silent}^{ss} = (\bar{g}_{Leak}E_{Leak} + \bar{g}_{syn_E}E_{syn_E}FB_{In\text{-}silent})/(\bar{g}_{Leak} + \bar{g}_{syn_E}FB_{In\text{-}silent}),$$

where $FB_{In\text{-}silent}$ denotes the summed feedback to the inactive $In$. A simple calculation determines that with our model parameter values, $V_{In\text{-}silent}^{ss} = V_{th}$ when $FB_{In\text{-}silent} = 0.04$. We denote this critical value as $FB_{crit}$, and we note that although the feedbacks fed to the extensor and flexor sides differ (and thus, how this value is reached differs), $FB_{crit}$ is independent of side. For convenience, equations (3.6),(3.7) are repeated here. For extensor neurons:

$$FB_i = w_{Ia\text{-}E,i}Ia\text{-}E + w_{Ib\text{-}E,i}Ib\text{-}E \tag{3.8}$$

for $i \in \{RG\text{-}E, PF\text{-}E, In\text{-}E, Inab\text{-}E\}$, and for flexor neurons,

$$FB_i = w_{Ia\text{-}F,i}Ia\text{-}F + w_{II\text{-}F,i}II\text{-}F \tag{3.9}$$

86

for $i \in \{RG\text{-}F, PF\text{-}F, In\text{-}F\}$.

Feedback terms depend on limb angle ($q$) and velocity ($v = \dot{q}$), governed by equation (3.5), as well as motoneuron output. However, $FB_{In\text{-}silent} = FB_{crit}$ is an equation that depends only on $q$ and $v$. Indeed, except during CPG transitions, all flexor neurons ($RG\text{-}F$, $In\text{-}F$, $PF\text{-}F$ and $Mn\text{-}F$) are inactive together. Thus, when $In\text{-}F$ is silent, $Mn\text{-}F$ is silent, so when calculating the feedback to $In\text{-}F$ during its silent phase, the terms in $Ia\text{-}F$ and $II\text{-}F$ that depend on $Mn\text{-}F$ are zero. The situation is analogous for the extensor side. Therefore, we can use equations (3.6),(3.7) (repeated above) to construct curves in limb phase space that indicate where the transitions in the CPG occur. We define the sTance Transition Curve as

$$TTC = \{(q, v) : v \geq 0, FB_{In\text{-}F} = FB_{crit}\}. \tag{3.10}$$

This curve is the collection of points in $(q, v)$ space where the voltage of $In\text{-}F$ reaches threshold and inhibits $RG\text{-}E$, initiating the switch from $E$ to $F$ dominance, which occurs midway through the stance phase. Similarly, the sWing Transition Curve

$$WTC = \{(q, v) : v \leq 0, FB_{In\text{-}E} = FB_{crit}\} \tag{3.11}$$

describes the set of points where the analogous switch from $F$ to $E$ dominance occurs in the swing phase. These two curves define vital switching manifolds for the system (which will be discussed in more detail in the next section). They are precisely determined, although there is a small delay from the time when an $In$ escapes to the time that this transition is transmitted via the corresponding $Mn$ and manifested in the forces acting on the limb, which we explain in the following remark.

**Remark 1.** *For each motoneuron voltage variable $V$, we also define a variable $x$ with $x' = f(V) - x$. Following Markin et al. [46], we use $x$ rather than $f(V)$ for defining transitions between eStance and fStance and between fSwing and eSwing (including for plotting transition curves in Figure 47A), for plotting motoneuron outputs (Figure 23A), and for computing average Mn outputs. The use of $x$, which slightly lags $f(V)$, contributes to the small time differences between the dominance switches of the In used to define the TTC and WTC and the times defined for the transitions from eStance to fStance and from fSwing to eSwing, as*

87

*mentioned in Section 3.2. A second factor in this difference is that there is a delay from In escape to the corresponding RG activation that drives Mn outputs. These time differences are all small and do not appear to affect the behavior of the model.*

Since the CPG and feedback operate in a closed loop, it is difficult to prove rigorously that phase transitions in the presence of feedback occur via $In$ escape for all drives. For larger drives, for instance, the inhibited $RG$ might have access to its left knee, but the inhibited $In$ could cross threshold first (or vice versa). Without knowing the time course of the feedback, we cannot determine which mechanism occurs first. We observe numerically that the $In$ always reaches synaptic threshold before the $RG$ can escape. We note that, as in the case without feedback, oscillations in the CPG persist until drive is very large, and break down when the active periods of $RG$ begin to overlap.

Since the $In$ escape transition mechanism does not depend on any particular nullcline configuration, as was needed for $RG$ escape in the case without feedback, feedback broadens the range of drives over which oscillations can occur, particularly for lower drives. Provided that the feedback strength to the $In$ is sufficiently large, the system will oscillate. We will return to the issue of what can cause oscillations to be lost in the presence of feedback, for example as occurs as drive is reduced, using an analysis of limb dynamics subject to $Mn$ outputs.

Finally, previous modeling work has proposed that stronger feedback signals should code for faster locomotor oscillations [34, 83]. The fact that an escape mechanism underlies CPG phase transitions in the model that we consider suggests that augmenting feedback signals in this model might speed up its oscillation frequency, by facilitating this escape (as opposed to models with release-based transitions, in which stronger positive inputs help sustain the dominant units and delay transitions) [74, 68, 19]. The result of such augmentation is complicated, however, by the fact that feedback signals also affect motoneuron outputs and hence limb dynamics, particularly transitions between stance and swing, which occur at different times from extensor/flexor transitions in the full model. It turns out that stronger feedback signals yield stronger motoneuron outputs, which speed up these stance/swing transitions and the associated epochs in the limb phase plane, enhancing the frequency increase expected from the CPG. The mechanisms responsible for these effects will be discussed. The

88

upshot of this analysis is that the CPG and limb responses to strengthened feedback provide complementary increases in the locomotor oscillation frequency in the model that we consider, as illustrated in Figure 30.
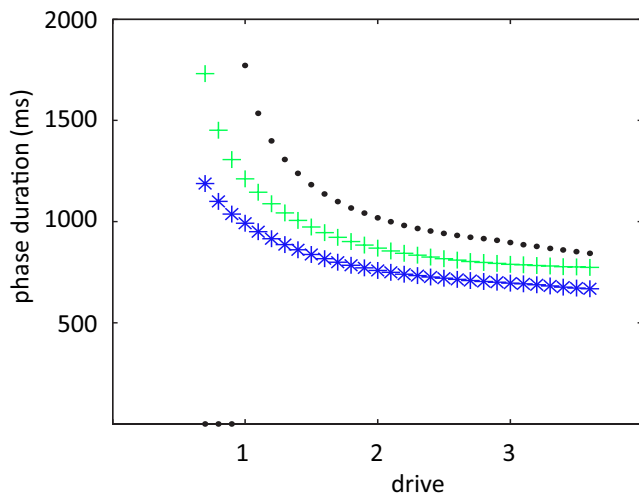


**Figure 30:** *Control of locomotor speed by supra-spinal drive for different feedback strengths. Green plus signs indicate step duration at normal strength, black dots and blue stars indicate step durations where feedback was set at 90 and 110 percent of baseline feedback strength, respectively. Increasing feedback strength increases limb frequency, most notably at lower drive values.*

We make one final note: we again observe that for relatively large drives, the extensor pattern formation ($PF\text{-}E$) neuron is able to intrinsically escape prior to the switch between $RG\text{-}F$ and $RG\text{-}E$. Its voltage, however, remains just slightly above threshold, so although it sends signals to $Mn\text{-}E$, they are weak, and full motoneuron activation does not occur without the $In\text{-}E$ escape outlined above. Furthermore, this $PF\text{-}E$ escape plays no role in the phase asymmetry shown in Figure 26; indeed, we have verified numerically that if we reduce the parameter that controls the strength of the input to $PF$, we can suppress this $PF\text{-}E$ activity yet retain full anti-phase $Mn$ output, without qualitatively affecting the asymmetric phase response to changes in supra-spinal drive (Figure 26B).

## 3.3 REDUCED MODEL RETAINS KEY MODEL FEATURES AND EXHIBITS A PERIODIC SOLUTION

In Section 3.2.3, we showed that the model CPG can exhibit half-center oscillations through different escape mechanisms depending on whether or not feedback is present. These mechanisms can be understood in terms of a separation of timescales and the consideration of nullclines for components of the CPG. We would now like to characterize the conditions under which stable periodic oscillations can occur in the presence of feedback as well as the dynamic mechanisms that shape these oscillations, which will be critical in understanding the asymmetric response to drive.

### 3.3.1 Rapid transitions can be used to distinguish four locomotor phases

We can visualize behavior of the model limb, governed by equation (3.5), in a phase space where limb velocity is plotted against angle. A locomotor cycle corresponds to a trajectory moving clockwise in $(q, \dot{q} = v)$ phase space. Positive velocity, leading to an increase in $q$, corresponds to periods when the ground contact force is present, which is denoted as the stance phase. A rapid change in which side of the CPG is dominant, and hence in $Mn$ activity, translates to a rapid change in the right hand side of equation (3.5), based on the force terms that depend on the motoneuron outputs. Eventually, such a change can cause the velocity of the limb to change sign, and in the model the ground reaction force instantaneously activates/deactivates when this happens, to simulate the onset/offset of ground contact.

Changes in CPG dominance and in ground reaction force partition limb motion into four distinct phases, such that within each phase, the limb behaves in a continuous manner, and at each transition, the limb acceleration is discontinuous. We denote each of the four phases by their dominant muscle (flexor or extensor), and the presence/absence of the ground reaction force (stance/swing) to obtain the notation eStance, fStance, fSwing, and eSwing. The eStance phase is characterized by an active $Mn\text{-}E$ and positive limb velocity, hence the additional force from ground contact is present. This phase begins when the limb trajectory

crosses from below to above the $q$-axis and is terminated when $RG\text{-}F$ turns on. As described in Section 3.2.3, we can define a curve in the limb phase plane such that when the limb trajectory hits this curve, the extensor component of the CPG becomes inactive and the flexor component activates. This definition can be made because the transition within the CPG occurs through an escape of $In\text{-}F$ from its silent phase, causing it to shut down $RG\text{-}E$ and $In\text{-}E$ and hence allowing $RG\text{-}F$ to activate. This escape occurs when the feedback to $In\text{-}F$ reaches a critical value $FB_{crit}$. Thus, the duration of the eStance phase depends on how quickly the feedback to $In\text{-}F$ reaches $FB_{crit}$, or how quickly the TTC is reached. The fStance phase is characterized by an active $Mn\text{-}F$ and positive limb velocity, so again, the ground reaction force is present here. This phase begins when $RG\text{-}F$ becomes active at the TTC and ends when the limb trajectory crosses the $q$-axis from above to below. The fSwing phase is characterized by an active $Mn\text{-}F$ and negative limb velocity, so the ground reaction force is absent. This phase begins when the limb trajectory crosses from above to below the $q$-axis and ends when $RG\text{-}E$ turns on. This transition occurs at another curve in the $(q, v)$ plane, the sWing Transition Curve or WTC, which is defined analogously to the TTC, using the feedback to $In\text{-}E$. Thus, the duration of fSwing depends simply on how long it takes the feedback to $In\text{-}E$ to reach $FB_{crit}$. The final phase, eSwing, is characterized by an active $Mn\text{-}E$ and negative limb velocity, again with no ground strike force present. This phase begins when $RG\text{-}E$ becomes active at the WTC and ends when the trajectory crosses from below to above the $q$-axis.

In Figure 31, we vary the drive and mark the onset of each of the phases in $(q, v)$ space. Green circles mark the onset of fStance, magenta plus signs the onset of fSwing, black dots the onset of eSwing, and red stars the onset of eStance. The onset of fStance and eSwing are slightly delayed relative to the transition curves, as explained in Remark 1. Note that the amplitude of the orbit increases as drive is increased, despite the fact that the step duration decreases.
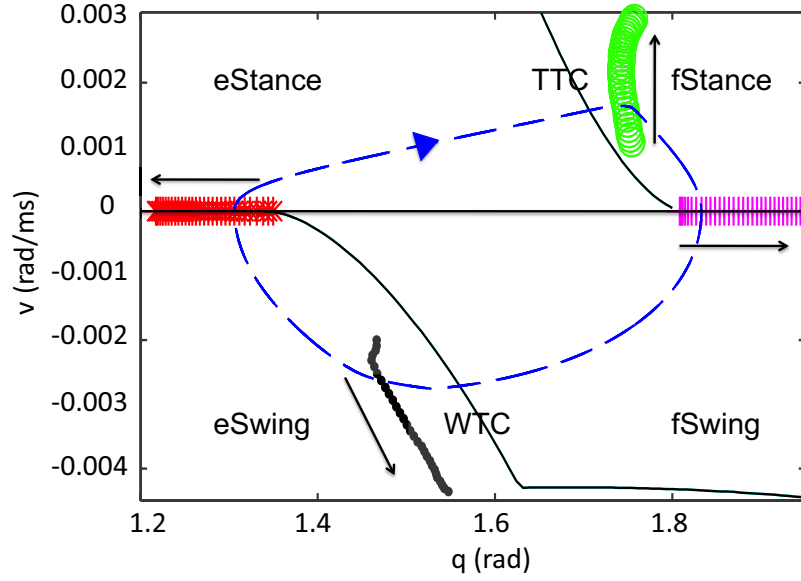
**Figure 31:** *Transitions between phases are marked over a range of drives. The solid arrows indicate the direction of increasing drive. Green circles denote the onset of fStance, magenta plus signs the onset of fSwing, black dots the onset of eSwing, and red stars the onset of eStance (onset of fStance and eSwing drawn when the relevant motoneuron output increases above 0.2, following [46]). The right hand side of the limb equation (3.5) changes in a discontinuous manner at each of these transitions. A sample trajectory (for drive=1.4), which evolves in the clockwise direction as time advances, is plotted with a blue dashed line for reference, and the transition curves are plotted in black. Notice that the CPG transitions lie close to the TTC and WTC, respectively, though they are shifted due to the brief transient the model exhibits between phases (see Remark 1).*

### 3.3.2   Outline of the model reductions

Now that we have described the phases involved in each oscillation cycle, we would like to establish conditions under which such oscillations occur and are stable. Indeed, model simulations suggest that the limb quickly settles to a pattern that appears stable under perturbations. We next undertake a mathematical analysis of the existence of this solution, with additional comments on its uniqueness and stability. Constructing a mathematical proof of the existence of the solution, while somewhat technically involved, can provide a practical understanding of what dynamic features contribute to the emergence of the rhythm, while considering the uniqueness and stability of the solution gives information about whether other rhythms might co-exist with expected locomotor oscillations and how the oscillation will respond to perturbations, including variations in drive strength. In fact, the complicated dynamics present in the full model equation (3.5) prohibits us from using dynamical systems techniques to analytically establish such results about this system, so we first implement certain simplifications to the model based on our earlier observations in Section 3.2. As we will discuss, the simplifications we will implement reduce the system to four continuous subsystems, and which subsystem rules the dynamics at a given time depends on which region of phase space the limb trajectory lies in. One key reduction is that we replace the time-dependent motoneuron output with constant values. This completely determines the right hand side of the pendulum dynamics, reducing the system to just two dimensions ($q$ and $v$), which allows us to utilize classical theorems from dynamical systems theory. We are able to construct an existence argument, which is mostly analytical but also relies on a few numerical observations, for a periodic oscillatory solution of the resulting reduced model. This result is attained by applying a version of the the Poincaré-Bendixson Theorem (generalize for discontinuous systems) to the flow of our hybrid system. Before we can utilize this theorem, however, we must constrain our trajectory in a compact region, which we obtained using a Melnikov argument. This argument is itself of mathematical interest, in that it requires the adaptation of Melnikov theory for a discontinuous system. In this section, we outline the reductions we implemented before we present the argument for existence.

First, we replace all inhibitory output terms in the model with a multiple of a Heaviside

step function,

$$H(V) = \begin{cases} 0.3944 & \text{if } V \geq V_{th}; \\ 0 & \text{if } V < V_{th}. \end{cases} \tag{3.12}$$

The factor 0.3944 was determined numerically from the original system by computing the time-average of the $f(V)$ values over all inhibitory neurons and using the obtained value for $f(V)$ in the equations for inhibitory synaptic currents. Second, we include sensory feedback only to $In$. Under these changes, the input to $RG$ is completely determined; drive, as always, is a constant, and each $RG$ neuron either receives inhibition or does not, depending on the state of the opposing $In$. Thus, unlike the full model in which the time-dependent inputs move the nullclines of each $RG$ around in its two-dimensional phase space, the nullclines for each $RG$ are now fixed in phase space except for abrupt jumps that occur when inhibition turns on or off. Maintaining the feedback to the $In$ preserves the escape transition mechanism discussed in Section 3.2.3, provided that the parameter that scales the drive to $PF$ is slightly reduced (to prevent these neurons from becoming active independently from $RG$ for large drives). Finally, we alter the outputs of the motoneurons so that for a fixed drive, they are of a constant value, namely the time-averaged motoneuron output from the full model oscillation, within each phase. We denote these constant values by $m_{eSt}$, $m_{fSt}$, $m_{fSw}$, and $m_{eSw}$, respectively. Although we do not explicitly include it in our notation, these values increase with drive strength, reflecting the fact that in the full model, $RG$ activation increases with drive, leading to a larger motoneuron output.

By fixing the motoneuron outputs, the right hand side of equation (3.5) is completely determined, and thus, from an initial condition, the position of the limb can be obtained at any time. Figure 32 shows a comparison of motoneuron output for the original and reduced models for drive strength $d = 1.4$.

We call the model that results from these alterations the *reduced model* and note that it preserves the important phase asymmetry feature seen in the original model (Figure 33). For each fixed drive, the limb dynamics of the reduced model is governed by four continuous
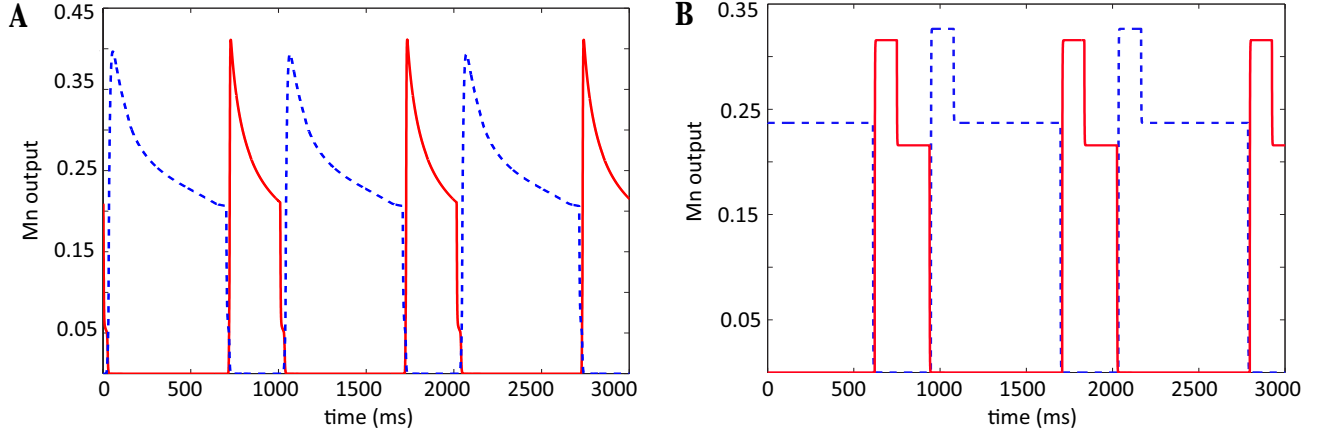
**Figure 32:** *Motoneuron output generated by the original model (A) and reduced model (B) for drive strength $d = 1.4$. Red solid curves correspond to $Mn\text{-}F$, blue dashed to $Mn\text{-}E$. In the reduced model, motoneuron output is fixed at a different value in each phase, for each drive.*

subsystems, one per phase,

$$I\ddot{q} = K\cos(q) - b\dot{q} + M_E(q, \dot{q}, m_{eSt}) - M_{GRmax}\cos(q), \qquad \text{(eStance)}$$

$$I\ddot{q} = K\cos(q) - b\dot{q} + M_F(q, \dot{q}, m_{fSt}) - M_{GRmax}\cos(q), \qquad \text{(fStance)}$$

$$I\ddot{q} = K\cos(q) - b\dot{q} + M_F(q, \dot{q}, m_{fSw}), \qquad \text{(fSwing)}$$

$$I\ddot{q} = K\cos(q) - b\dot{q} + M_E(q, \dot{q}, m_{eSw}), \qquad \text{(eSwing)} \qquad (3.13)$$

where we recall that $M_{GRmax}$ denotes the amplitude of the moment of the ground reaction force, $M_{GR}(q)$.

We now introduce notation to encode the discontinuities in system (3.13). Define

$$\{A\} = \begin{cases} K/I & \text{if swing;} \\ (K - M_{GRmax})/I & \text{if stance,} \end{cases} \qquad (3.14)$$

$$\{m\} = \begin{cases} m_{eSt} & \text{if eStance;} \\ m_{fSt} & \text{if fStance;} \\ m_{fSw} & \text{if fSwing;} \\ m_{eSw} & \text{if eSwing,} \end{cases} \qquad (3.15)$$

95
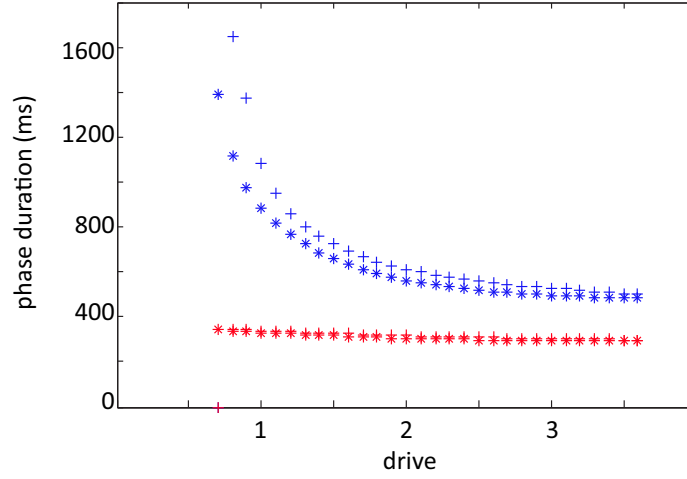
**Figure 33:** *Reduced model preserves phase asymmetry as drive is increased. Stance and swing phase durations for the original model are shown in blue and red stars, respectively. Stance and swing phase durations for the reduced model are plotted in analogous colors with plus signs.*

and

$$\{M\} = \begin{cases} M_E/I & \text{if } Mn\text{-}E \text{ is active;} \\ M_F/I & \text{if } Mn\text{-}F \text{ is active.} \end{cases} \tag{3.16}$$

With these definitions, we will use the shorthand

$$\ddot{q} = \{A\}\cos(q) - b\dot{q}/I + \{M\}(q, \dot{q}, \{m\}) \tag{3.17}$$

to denote the drive-dependent system of equations in (3.13). The brackets indicate that the function/constant within takes a value that depends on the limb's location in phase space. When we work within a certain phase, however, we will specify those terms explicitly for clarity.

### 3.3.3 Oscillations in the CPG component

We showed that in the absence of feedback, switching between flexor and extensor activation within the CPG occurs through the escape of the suppressed $RG$. In contrast, when feedback is present, each dominance switch is initiated when excitatory feedback sufficiently increases the voltage of the silent $In$ so that it can activate by escape and shut down the active $RG$ on the opposite side of the CPG (Section 3.2). For our reduced model to be consistent with the assumptions made in defining it, it is important that the transitions still occur through $In$ escape, so we next verify that this is the case. Given that the system is in a state with one side active and the other suppressed, we first determine whether or not the silent $RG$ could escape and initiate a phase transition. We can apply the approach used in Section 3.2.2; however, in the reduced model, inhibition from the active $In$ takes the same value regardless of drive. Thus, in this case, there exists a unique drive value that causes the $V$ and $h$-nullclines for the inhibited $RG$ to intersect precisely at the left knee of the $V$-nullcline. For drive values smaller than this value, the intersection point lies on the left branch, and an escape transition initiated by the $RG$ is not possible. Therefore, if we restrict our drive set to drives below this level, the transitions for the reduced system cannot occur through an $RG$ mechanism, and are guaranteed to occur via $In$ escape. As we did in Section 3.2.2, we find an explicit equation $h_c(V, d)$ for the $RG$ $V$-nullcline inhibited with the strength indicated in equation (3.12), and we solve $h_c(V, d) = h_\infty(V)$ to find a drive-dependent expression for the voltage of the silent critical point, $V_{ip}(d)$. Separately, we calculate the drive-dependent voltage of the left knee, which satisfies $h_c'(V, d) = 0, h_c''(V, d) < 0$, where $\prime$ denotes differentiation with respect to $V$. We will denote this voltage as $V_{lk}(d)$. Then, the drive that satisfies $V_{ip}(d) = V_{lk}(d)$ is the unique value where the left knee intersects the sigmoid. This value exceeds the largest drive value considered for the original model, which is the range of drives that we also use for our reduced model.

Next, it is easy to see that the transition cannot occur via $RG$ release, in which the active $RG$ reaches the right knee of its $V$-nullcline. Indeed, in the reduced model, the active $RG$ receives no inhibition or feedback, and these conditions cause it to have a stable critical point on the right branch of its $V$-nullcline, preventing release. In theory, the active $In$ could

release the silent neurons and cause a transition, but this mechanism was never observed in the full model, and the input from $RG$ to $In$ and feedback strength are similar in the reduced model, again preventing this mechanism from arising. Thus, in the reduced model, the CPG switch always occurs through the $In$ escape mechanism.

### 3.3.4   Existence and stability of a periodic solution for the reduced model

In this subsection, we give a dynamical systems argument to explain the mechanisms through which the existence of a periodic solution comes about in the reduced model, if the supra-spinal drive is sufficiently large. We will consider what happens for smaller drives in Section 4.1. From a mathematical point of view, rigorously establishing existence and stability of physically observed solutions is an important check of the validity of a model and may contribute to an understanding of the constraints on model parameters needed to maintain this validity. Moreover, as discussed earlier, these steps will allow us to better understand how oscillations may be altered or even lost under perturbations such as changes in drive strength and will also yield insights that will help us to explain the asymmetric phase response to changes in drive, as presented in Section 4.1.

If we can constrain our flow in a compact region without critical points, a generalization of the Poincaré-Bendixson Theorem (applied to discontinuous systems) will establish the existence of a periodic orbit. To form this compact region, we will replace the moments of the muscle forces with constant values that generate a special closed orbit. We will then perturb the system away from these values and show that the closed orbit breaks in such a way so that the flow of the system is constrained within a compact region. The latter step uses a dynamical systems technique known as Melnikov theory. We must adapt this theory in a novel way, however, to handle the discontinuity present in model system (3.17). Finally, since this method only applies under small perturbations, we implement a homotopy argument that ensures this alignment is maintained up until the true reduced model is recovered. The use of Melnikov theory requires that certain assumptions hold. We will first review these assumptions and then show that system (3.17) can be molded to fit them.

Let us assume that $x = (q, v)$ satisfies a system of equations of the form $\dot{x} = f(x) + \epsilon g(x, t)$, where $f, g$ are continuous functions and $g$ is $\theta$-periodic in $t$, such that when $\epsilon = 0$, a homoclinic orbit $\gamma_0$ of this system originates from a saddle point $x_0 = (q_0, v_0)$. Denote the unstable manifold of $x_0$ as $W^u(x_0) = \{p \in D \,|\, \lim_{t \to -\infty} p \cdot t = x_0\}$ and the stable manifold as $W^s(x_0) = \{p \in D \,|\, \lim_{t \to +\infty} p \cdot t = x_0\}$, where $D = \{(q, v) \,|\, q \geq q_0\}$. By this choice of $D$, we select the manifold branches that lie in a particular half-plane relative to the critical point (later, it will become clear that this half-plane is the domain we care about for our system). Assume that $\gamma_0 = W^u(x_0) \cap W^s(x_0)$. Fix a point $p^* \in \gamma_0$ and consider a transversal $\Sigma$ to the flow that passes through this point, at time $t_0$. Suppose that $x_0$ perturbs to a saddle point $x_\epsilon$ for $\epsilon$ sufficiently small, and let $h^u(\epsilon) = W^u(x_\epsilon) \cap \Sigma$ and $h^s(\epsilon) = W^s(x_\epsilon) \cap \Sigma$, where $x_\epsilon$ denotes the critical point of the system for a fixed value of $\epsilon$. Although $h^u(0) = h^s(0) = p^*$, we do not expect this intersection to persist as $\epsilon$ is increased. See Figure 34 for an illustration.
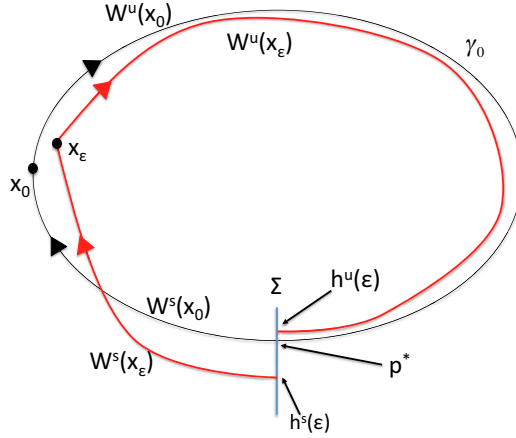


**Figure 34:** *A general schematic of the set-up for the existence argument. We wish to show that as $\epsilon$ is increased from 0, the homoclinic perturbs as indicated in red, so that trajectories are trapped in forward time within the region bounded by the unstable and stable manifolds of $x_\epsilon$. Arrows indicate flow in the forward direction.*

The Melnikov function

$$\mathcal{M}(t_0) = \int_{-\infty}^{T} e^{-\int_{t_0}^{t} \nabla f(\gamma_0(s)) ds} f(\gamma_0(t)) \wedge g(\gamma_0(t), t + t_0) \, \mathrm{d}t \qquad (3.18)$$

99

provides an expression that indicates how $h^u(\epsilon)$ and $h^s(\epsilon)$ perturb for $\epsilon$ sufficiently small; traditionally, $T = \infty$ [30], but we will discuss $T$ for our model below. If this expression is negative, then as $\epsilon$ is increased from 0, the homoclinic orbit splits such that $W^u(x_\epsilon)$ lies on the inside of $W^s(x_\epsilon)$, as shown in Figure 34. If the expression is positive, then the opposite holds. Ultimately, we would like to prove that the flow for our reduced system (3.17) from an appropriate set of initial conditions is trapped in a compact region in phase space in forward time and hence, with some additional arguments, yields a periodic orbit. We intend to verify this by showing that an appropriate Melnikov function (3.18) is negative, but first, we need to cast our reduced system in the form described above and adapt some of the definitions involved to apply to our discontinuous system.

We introduce the new system

$$
\begin{aligned}
\dot{q} &= v \\
\dot{v} &= \{A\}\cos(q) + \{M^*\} - bv/I + \epsilon(\{M\}(q,v,\{m\}) - \{M^*\}),
\end{aligned}
\qquad (3.19)
$$

where $\{A\}$, $\{M\}$, and $\{m\}$ were previously defined when we introduced the reduced system (3.17), and

$$
\{M^*\} =
\begin{cases}
M^*_{eSt}/I & \text{if eStance,} \\
M^*_{fSt}/I & \text{if fStance,} \\
M^*_{fSw}/I & \text{if fSwing,} \\
M^*_{eSw}/I & \text{if eSwing}
\end{cases}
\qquad (3.20)
$$

is another piecewise constant function that is chosen to approximate $\{M\}(q,v,\{m\})$ in each of the four phases. System (3.19) is equivalent to system (3.17) for $\epsilon = 1$. The following arguments will require drive $d$ to be sufficiently large, as we shall discuss. For associated numerical illustrations, we chose the $\{m\}$ values corresponding to $d=1.4$.

System (3.19) is of the form $\dot{x} = f(x) + \epsilon g(x)$, where $f(x) = (v, \{A\}\cos(q) + \{M^*\} - bv/I)$ and $g(x) = (0, \{M\}(q,v,\{m\}) - \{M^*\})$. While the reduced system is recovered when $\epsilon = 1$, for $\epsilon = 0$, we have a system where the entire muscle moment is replaced by a fixed value in each phase. However, the functions $f$ and $g$ in system (3.19) are not continuous, whereas the Melnikov function is defined for continuous systems. Fortunately, the construction and

100

interpretation of the Melnikov function generalize immediately to the piecewise continuous system (3.17) that we consider, once we adapt the definition of the Melnikov function accordingly, as we now explain.

Let $x_0$ be the saddle critical point where the $v$-nullcline corresponding to the eStance phase intersects the $q$-nullcline ($q$-axis) in the $\epsilon = 0$ system. Note that $x_0$ is not a critical point for the other phases. By choosing an appropriate $\{M^*\}$, we can construct a closed orbit of system (3.19) that begins with the unstable manifold $W^u(x_0)$, which is of interest because the limb trajectory of the full model is in close proximity to this manifold in the eStance phase for small drives (see Section 4.1).

Once we choose $M^*_{eSt}, M^*_{fSt}$, and $M^*_{fSw}$, the value of $M^*_{eSw}$ is fully determined as the unique value that returns the orbit to $x_0$. Interestingly, because $x_0$ is not a critical point of system (3.19) in the eSwing phase, the orbit that we are following reaches $x_0$ in finite time, at a time that we denote by $T$. We will assume that values of $\{M^*\}$ can be found such that this closed loop orbit exists, and this is the major assumption of our argument. In practice, this value can be found if drive is not too small. The violation of this assumption for smaller drive is discussed in Section 4.1.

Denote the orbit formed from this choice of $\{M^*\}$ as $\gamma_0$ and choose a vertical segment near the WTC, which we call $\Sigma$, to which the flow of (3.19) is transverse (i.e., a local transversal). In this case, since our argument will depend on very small changes in the right hand side of equation (3.19), we do not ignore the transient between the time the trajectory hits the WTC and the time when the eSwing phase actually begins, as we indicate in Remark 1. We account for this transient by marking the place on $\gamma_0$ where the eSwing phase begins and using the vertical line through this point as our transversal $\Sigma$. For $\epsilon = 0$, we can refer to the segment of $\gamma_0$ from $\Sigma$ to $x_0$ as $\tilde{W}^s(x_0)$, although it does not fit the definition of a stable manifold.

To establish results for system (3.17), which is recovered for $\epsilon = 1$, we next wish to check how $\gamma_0$ perturbs as $\epsilon$ is increased from 0. First, we verify that for each $\epsilon \in (0, 1]$, system (3.19) has a critical point $x_\epsilon = (q_\epsilon, 0)$ that is a saddle, converging to $x_0$ as $\epsilon \to 0^+$, in the

eStance phase. For each $\epsilon$, such a critical point exists if there is a solution $q$ to

$$\epsilon = \frac{-(K - M_{GRmax})\cos(q) - M_{eSt}^*}{M_E(q, 0, m_{eSt}) - M_{eSt}^*}. \tag{3.21}$$

Since the critical point $x_0 = (q_0, 0)$ exists with $\epsilon = 0$, we can write $M_{eSt}^* = -(K - M_{GRmax})\cos(q_0)$. Substituting this expression back into equation (3.21) and dividing on top and bottom by $(K - M_{GRmax})$, we obtain

$$\epsilon = \frac{\cos(q_0) - \cos(q)}{\cos(q_0) + N(q)} \tag{3.22}$$

for $N(q) = M_E(q, 0, m_{eSt})/(K - M_{GRmax})$. The quantity in the denominator of (3.22) is positive for $\epsilon = 0$ and $q = q_0$, but $N(q_0)$ is itself negative, since $K - M_{GRmax}$ is negative while $M_E$ is positive. If we increase $q$ from $q_0$, which lies between $0$ and $\pi/2$, then the numerator of (3.22) grows from $0$ while $M_E(q)$ is observed numerically to grow as well. Hence, the denominator of the right side of equation (3.22) becomes less positive as $q$ increases toward $\pi/2$. Thus, the right hand side expression increases past $1$, which implies that there is a solution $q_\epsilon$ to equation (3.21) for each $\epsilon \in (0, 1]$, as desired.

Next, we check that $x_\epsilon = (q_\epsilon, 0)$ is a saddle point for all $\epsilon \in (0, 1]$. For a two dimensional system of ordinary differential equations, a critical point is a saddle provided that the determinant of the linearization at that point is negative. Linearizing system (3.19) yields a matrix with determinant $(K - M_{GRmax})\sin(q_\epsilon) - \epsilon \frac{dM_E(q_\epsilon, 0, m_{eSt}^*)}{dq}$. The coefficient of the sine term is always negative and, as we just used to establish the existence of the critical points, numerical results show that $\frac{dM_E(q_\epsilon, 0, m_{eSt}^*)}{dq}$ is positive for $q \leq \pi/2$, which holds for $x_\epsilon$ for $\epsilon \in (0, 1)$. Thus, the critical points $x_\epsilon$ are indeed saddle points.

Now, fix $\epsilon > 0$ small. Since $x_\epsilon$ is a saddle point, it has an unstable manifold, defined with respect to the eStance component of the flow of (3.19). Since the $v$-component of $x_\epsilon$ is zero, we can define $\tilde{W}^s(x_\epsilon)$ as the trajectory of the eSwing component of (3.19), taken in backwards time, connecting from $x_\epsilon$ to $\Sigma$. We aim to show that $W^u(x_\epsilon)$ perturbs to the inside of $\tilde{W}^s(x_\epsilon)$ when $\epsilon$ is increased from zero, similarly to what is shown for $W^u(x_\epsilon)$ and $W^s(x_\epsilon)$ in the schematic illustration in Figure 34. If we denote the intersections of $W^u(x_\epsilon), \tilde{W}^s(x_\epsilon)$ with the transversal $\Sigma$ by $h^k(\epsilon) = (h_q^k(\epsilon), h_v^k(\epsilon)), k \in \{u, s\}$, then this means that we require $h_v^u(\epsilon) \geq h_v^s(\epsilon)$, since $\Sigma$ is vertical. In our notation, this relationship occurs if the function

102

$\mathcal{M}(t_0)$ in (3.18) is negative, where $T - t_0$ denotes the time of passage of $\tilde{W}^s(x_\epsilon)$ from $\Sigma$ to $x_\epsilon$.

For system (3.19), $\mathcal{M}(t_0) = \int_{-\infty}^{T} e^{-(b/I)(t-t_0)} v(\{M\}(q, v, \{m\}) - \{M^*\}) dt$. This expression splits into four integrals, and since the limb trajectory $\gamma_0$ actually reaches $x_0$ at a finite forward time $T$ due to the discontinuous nature of the system, only the eStance integral is evaluated over an infinite time interval. Until this point, we have assumed that we have chosen $\{M^*\}$ such that a closed orbit $\gamma_0$ exists with $\epsilon = 0$. We now place an additional constraint on our choice of $\{M^*\}$: we wish to choose $\{M^*\}$ such that the integrand in each of these integrals is strictly negative. The existence of such a choice is a sufficient, although not necessary, condition for the splitting to occur as desired. Next, we show that we can select values of $M^*_{eSt}$, $M^*_{fSt}$, $M^*_{fSw}$, and $M^*_{eSw}$ that achieve this condition, such that $\mathcal{M}(t_0) < 0$ indeed holds. During the stance phase, $v$ is positive, so we wish to choose $M^*_{eSt}$ larger than $M_E(q, v, m_{eSt})$ in eStance and $M^*_{fSt}$ larger than $M_F(q, v, m_{fSt})$ in fStance. During eSwing and fSwing, we would like to make the opposite choice, setting $M^*_{eSw}$ smaller than $M_E(q, v, m_{eSw})$ in eSwing and $M^*_{fSw}$ smaller than $M_F(q, v, m_{fSw})$ in fSwing, since $v$ is negative during these phases.

To determine whether making such a choice is possible, we require knowledge of the values that $M_F$ and $M_E$ take in phase space. Specifically, we need to find the maximum of $M_E$ in eStance and $M_F$ in fStance, and the minimum of $M_F$ in fSwing and $M_E$ in eSwing. We could run into a circular argument here, because the values of $M_E$ and $M_F$ for $\epsilon \in (0, 1)$ depend on the system trajectory, which depends on $\{M^*\}$. However, by differentiating the relevant equations, one can show directly that $dM_E/dv \leq 0$ in eStance and eSwing, and $dM_F/dv \leq 0$ in fStance and fSwing. Thus, the maximum value of $M_E$ in eStance and $M_F$ in fStance, and the minimum value of $M_F$ in fSwing and $M_E$ in eSwing, all occur when $v = 0$.

Therefore, to obtain bounds on their possible values, we only need to evaluate $M_E$ and $M_F$ over $q$ values between 0 and $\pi$, which are constraints built into the model, with $v = 0$. Numerically, we observe that the maximum of $M_E$ for the eStance vector field occurs near $\pi/2$ and is equal to 58.11, the maximum of $M_F$ for fStance occurs at the upper boundary at $\pi$ and is equal to 0, the minimum of $M_F$ for fSwing occurs near $\pi/2$ and is equal to -101.67, and the minimum of $M_E$ for eSwing occurs at 0 and is equal to 0.

In light of these results, we choose $M_{eSt}^* \geq 59$ and $M_{fSw}^* \leq -102$, and we restrict our possible range of $M_{eSw}^*$ to consist of negative values. The bound in fStance is poor since $M_F$ needs to be sufficiently negative in order for the trajectory to reach the $q$-axis to complete the fStance phase. That is, while $M_{fSt}^* > 0$ would be needed to satisfy $M_{fSt}^* \geq M_F(q, v, m_{fSt})$, this choice would prevent us from constructing the homoclinic we desire in system (3.19) with $\epsilon = 0$. We show in our analysis that any trajectory that completes the fStance phase and intersects the $q$-axis must remain at angles below the angle associated with the critical point of system (3.19) during its passage through fStance. Thus, we would like to use the angle of the fStance critical point for system (3.19) to provide a better bound for $M_F$. Note, however, that the fStance critical point satisfies

$$\epsilon(q_\epsilon) = \frac{-(K - M_{GRmax})\cos(q_\epsilon) - M_{fSt}^*}{M_F(q_\epsilon, 0, m_{fSt}) - M_{fSt}^*}, \tag{3.23}$$

a relationship that depends on the choice of $M_{fSt}^*$.

To avoid circularity, we proceed in the following way. We fix an angle $\hat{q}$ and determine $M_F(\hat{q}, 0, m_{fSt})$. We choose this value, call it $\hat{M}_F$, and use it in place of $M_{fSt}^*$ in the fStance form of system (3.19) to compute the $q$-value of the fStance critical point as $\epsilon$ varies between 0 and 1. We check that the angle associated with each of these critical points is less than $\hat{q}$, and thus we conclude that the trajectories of (3.19) with $M_{fSt}^* = \hat{M}_F$ maintain $q < \hat{q}$ throughout fStance. Since $M_F(q, v)$ attains its maximum at $v = 0$ for each fixed $q$, and since $M_F(q, 0)$ is a increasing function of $q$, we can use $\hat{M}_F$ as an upper bound for $M_F(q, \dot{q}, m_{fSt})$ in system (3.19) for all $\epsilon$. The particular $\hat{q}$ we chose satisfied $M_F(\hat{q}, 0, m_{fSt}) = -94.7$, which allows us to choose any $M_{fSt}^* > \hat{M}_F = -94.7$. See Figure 35 for an illustration of these relationships.

Figure 36 shows the homoclinic for the $\epsilon = 0$ case along with $W^u(x_\epsilon)$ and $\tilde{W}^s(x_\epsilon)$ for $\epsilon = 0.01$ and $\epsilon = 0.1$ with the indicated choices of $\{M^*\}$. Notice that for $\epsilon > 0$ sufficiently small, the unstable manifold $W^u(x_\epsilon)$ is trapped inside of the invariant curve $\tilde{W}^s(x_\epsilon)$, as desired. While this alignment of manifolds holds for small $\epsilon$, recall that our reduced model is equivalent to system (3.19) with $\epsilon=1$. As $\epsilon$ grows, higher order terms not accounted for in the Melnikov function could become significant. Thus, we use an alternative comparison approach to consider the effect of increasing $\epsilon$ and show that the direction of splitting is
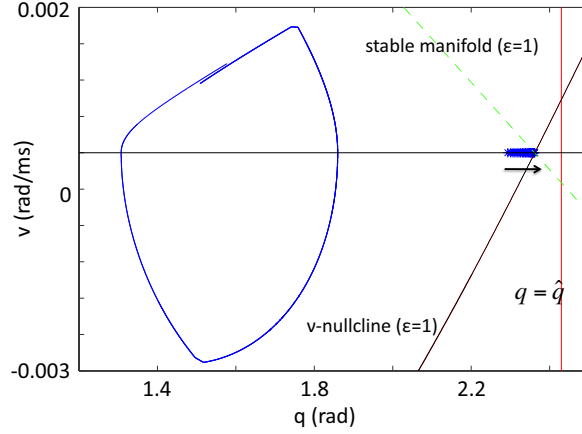
**Figure 35:** *Relationship between the critical points for system (3.19) and the angle upper bound,* $\hat{q}$*. The critical points are plotted as blue asterisks on* $\{v = 0\}$ *with an arrow indicating the trend in their location as* $\epsilon$ *increases, and the line* $\{q = \hat{q}\}$ *is indicated in red. The* $q$ *and* $v$*-nullclines are plotted as black solid lines, and the stable manifold is a green dashed line for the* $\epsilon = 1$ *system; these intersect in the rightmost critical point. For reference, the limit cycle for the* $\epsilon = 1$ *system is plotted. In order to transition to the fSwing phase, the* $q$*-values on the limit cycle in fStance must be bounded above by the* $q$*-coordinates of the fStance critical point.* $\hat{q}$ *was chosen as an upper bound of these bounds, so that* $\hat{M}_F$ *is an upper bound of* $M_F(q, v, m_{fSt})$*.*

maintained for all $\epsilon$ up to 1. The desired manifold alignment corresponds to the inequality $h_v^u(\epsilon) > h_v^s(\epsilon)$, which refers to the relative positions of the intersections of these manifolds with the transversal $\Sigma$. We would like to show that this alignment is preserved as $\epsilon \uparrow 1$. A sufficient condition for this result is that that for $\epsilon_1 \leq \epsilon_2$, $h_v^u(\epsilon_2) \geq h_v^u(\epsilon_1)$ and $h_v^s(\epsilon_2) \leq h_v^s(\epsilon_1)$ both hold, so we now try to establish these inequalities.

We have already established that the $q$-coordinates of the critical points $x_{\epsilon_2}$ and $x_{\epsilon_1}$ satisfy $q_{\epsilon_2} > q_{\epsilon_1}$ for $\epsilon_2 > \epsilon_1$, so that $W^u(x_{\epsilon_2})$ lies to the right of $W^u(x_{\epsilon_1})$ in a neighborhood of $x_{\epsilon_1}$ and $x_{\epsilon_2}$ for $\epsilon_2 > \epsilon_1$. Moreover, we can see that this orientation is preserved for the duration of the eStance phase. Indeed, if the two manifolds were ever to touch, as would have to occur to allow $q_{\epsilon_2}(t) < q_{\epsilon_1}(t)$ to result, then $\dot{q}_2 = \dot{q}_1$, and then $0 \leq \dot{v}_2 \leq \dot{v}_1$, since $\dot{v}_2 - \dot{v}_1 = (\epsilon_2 - \epsilon_1)(M_E(q, v, m_{eSt}) - M_{eSt}^*)/I$. Because we have chosen $M_{eSt}^*$ to exceed the largest possible value that $M_E(q, v, m_{eSt})$ could take along a relevant trajectory of system (3.19) in eStance, we know that this expression is negative. Thus, $\dot{v}_2 < \dot{v}_1$ at the intersection
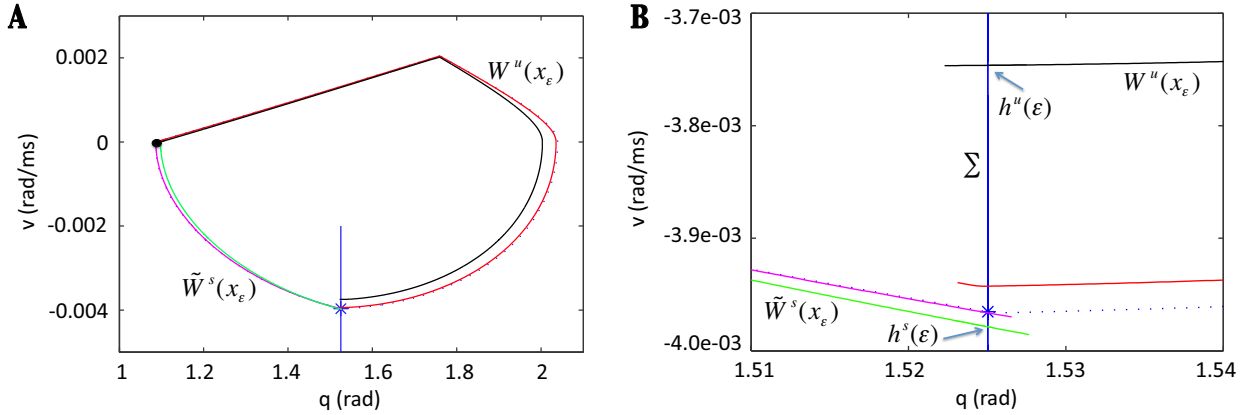
**Figure 36:** *Key structures for the Melnikov argument for $\epsilon$ = 0.01 and 0.1 with $\{M^*_{eSt}, M^*_{fSt}, M^*_{fSw}, M^*_{eSw}\}$ = $\{67, -90, -100, -2.25\}$. (A) The closed orbit $\gamma_0$ for system (3.19) with $\epsilon = 0$ is plotted with a blue dotted line, along with the manifolds $W^u(x_\epsilon)$ {red, black} and $\tilde{W}^s(x_\epsilon)$ {pink, green} for system (3.19) with $\epsilon \in \{0.01, 0.1\}$. The transversal $\Sigma$ is chosen as a vertical line (blue) through the point where eSwing begins on $\gamma_0$ (indicated with a blue star), and the saddle point is indicated with a black dot. (B) Zoomed view of (A) near the intersection of $\gamma_0$ and invariant manifolds with $\Sigma$, showing that $W^u(x_\epsilon)$ perturbs to the inside of $\tilde{W}^s(x_\epsilon)$ in both cases. For $\epsilon$ sufficiently close to 0, $\tilde{W}^s(x_\epsilon)$ remains close to $\gamma_0$, and it perturbs below $\gamma_0$ as $\epsilon$ increases. In (B), labeled manifolds and points indicate the $\epsilon = 0.1$ case.*

point, and $W^u(x_{\epsilon_2})$ remains on the inside of $W^u(x_{\epsilon_1})$.

Assuming that the trajectories do not cross during the brief transient between the crossing of the TTC and the switch to the fStance phase (which we observe numerically), then $W^u(x_{\epsilon_1})$ is above $W^u(x_{\epsilon_2})$ at the onset of fStance. This initial alignment in fact ensures that the manifolds do not cross in the fStance phase. Again, if they were ever to touch, then $\dot{q}_2 = \dot{q}_1$, and thus $\dot{v}_2 \leq \dot{v}_1 \leq 0$, since $\dot{v}_2 - \dot{v}_1 = (\epsilon_2 - \epsilon_1)(M_F(q, v, m_{fSt}) - M^*_{fSt})/I \leq 0$. Therefore, $W^u(x_{\epsilon_1})$ lies to the right of $W^u(x_{\epsilon_2})$ at the end of fStance and, equivalently, at the start of the fSwing phase. Now, if the manifolds were ever to touch in this phase, then $0 \geq \dot{v}_2 \geq \dot{v}_1$ since $\dot{v}_2 - \dot{v}_1 = (\epsilon_2 - \epsilon_1)(M_F(q, v, m_{fSw}) - M^*_{fSw})/I \geq 0$. Thus, $W^u(x_{\epsilon_1})$ remains outside of $W^u(x_{\epsilon_2})$ until $\Sigma$ is reached, i.e. $h^u_v(\epsilon_2) \geq h^u_v(\epsilon_1)$, and we have obtained the first condition that we seek.

We next consider the backward flow in eSwing. $\tilde{W}^s(x_{\epsilon_1})$ lies to the left of $\tilde{W}^s(x_{\epsilon_2})$ in a neighborhood of $x_{\epsilon_1}$ and $x_{\epsilon_2}$ for $\epsilon_1, \epsilon_2$ sufficiently close to each other with $\epsilon_2 > \epsilon_1$. If $\tilde{W}^s(x_{\epsilon_2})$ and $\tilde{W}^s(x_{\epsilon_1})$ intersect, then $\dot{q}_1 = \dot{q}_2$ and $\dot{v}_1 - \dot{v}_2 = -(\epsilon_1 - \epsilon_2)(M_E(q_1, v_1, m_{eSw}) - M^*_{eSw})/I$,

106

which is greater than 0 since $\epsilon_1 - \epsilon_2$ is negative and $(M_E(q_1, v_1, m_{eSw}) - M^*_{eSw})$ is positive by construction. Thus, they move through each other and cannot cross each other again, and therefore $h^s_v(\epsilon_2) \leq h^s_v(\epsilon_1)$, as desired.

If they do not cross, then they still must traverse an interval of common $q$ values to reach $\Sigma$. For each fixed $q$ obtained by both $\tilde{W}^s(x_{\epsilon_2})$ and $\tilde{W}^s(x_{\epsilon_1})$, in the absence of a crossing, $0 > v_2 > v_1$. For system (3.19),

$$\frac{dv}{dq} = \frac{(K/I)\cos(q) + (M^*_{eSw}/I)}{v} + \frac{-b}{I} + \frac{\epsilon(M_{eSw}(q, v, m_{eSw}) - M^*_{eSw})/I}{v}, \qquad (3.24)$$

which is the sum of three negative terms over the range of $q$ values traversed in eSwing and hence is negative. Moreover, the only $v$-dependence in the right hand side of equation (3.24) occurs in the denominators of the first and third terms and in $M_{eSw}$. Thus, if we compare the right hand side of equation (3.24) at $(q, v_2)$ with $\epsilon = \epsilon_2$ versus a baseline of $(q, v_1)$ with $\epsilon = \epsilon_1$, we see that the first term becomes more negative, the second term does not change, and the third term also becomes more negative (using a calculation based on the form of $M_{eSw}$, for which we omit details). Thus, while $\tilde{W}^s(x_{\epsilon_2})$ lies above $\tilde{W}^s(x_{\epsilon_1})$, the distance between these curves shrinks over the entire range of $q$ values that both traverse, since the former exhibits a larger decrease in $v$ for each such $q$.

In summary, for any $\epsilon_1, \epsilon_2 \in (0, 1]$ with $\epsilon_2 > \epsilon_1$, we have $h^u_v(\epsilon_2) > h^u_v(\epsilon_1)$. If $\epsilon_1$ is sufficiently small, then $h^u_v(\epsilon_1) > h^s_v(\epsilon_1)$, by our Melnikov calculation. Thus, we have shown analytically that $h^u_v(\epsilon)$ stays above $h^s_v(\epsilon)$ for some range of small $\epsilon$. We have also shown rigorously that for any $\epsilon_1, \epsilon_2 \in (0, 1]$ with $\epsilon_2 > \epsilon_1$, $h^s_v(\epsilon_1) > h^s_v(\epsilon_2)$ if $\tilde{W}^s(\epsilon_2)$ and $\tilde{W}^s(\epsilon_1)$ cross during the backwards flow of eSwing. Finally, we have an argument indicating why $|h^s_v(\epsilon_1) - h^s_v(\epsilon_2)|$ ends up being small, even if no crossing occurs. While we do not have a rigorous bound on $|h^s_v(\epsilon)|$, these arguments explain why the ordering of $h^u_v(\epsilon)$ and $h^s_v(\epsilon)$ is preserved as $\epsilon$ increases up to 1, as desired.

The results of this analysis show that for the reduced model, namely system (3.19) with $\epsilon = 1$, there exists a compact region in phase space in which limb trajectories emerging from initial conditions at the onset of the eStance phase will be trapped in forward time. Indeed, the eStance critical point $x_1 = (q_1, 0)$ of the reduced system has an unstable manifold $W^u(x_1)$, which evolves away from $x_1$ in forward time, crosses through the $q$-axis from the

107

positive $v$ half-plane to the negative $v$ half-plane, and then returns to the $q$-axis again, say at $x^u = (q^u, 0)$. From the analysis above, we know that drive can be chosen such that $\gamma_0$ exists, and we have $q_1 < q^u$ for such drive. Let $R$ denote the compact region bounded by the segment of the $q$-axis with $q$ values between $q_1$ and $q^u$, $x_1$ itself, and $W^u(x_1)$. Any trajectory starting from an eStance initial condition between $x_1$ and $x^u$ in eStance is trapped in the interior of $R$ for all time. There are no true critical points in the interior of $R$, nor could the flow of any of the continuous subsystems in the reduced model (3.13) reach any critical points inside $R$ without first causing a phase transition that causes the point to become nonsingular. Thus, a stable periodic orbit must exist in $R$ by a generalization of the Poincaré-Bendixson Theorem applied to discontinuous systems [69, 47]. The reduced model, which fixes the motoneuron output at constant values and updates the system at the switching manifolds, allows us to apply this theorem because it is a two-dimensional reduction of the full system.

While this argument establishes that there exists at least one stable periodic orbit in region $R$, it does not prove uniqueness. In theory, other solutions could co-exist with the periodic one that we have analyzed, which could either compromise the relevance of the model or point to some unexpected locomotor phenomenon. A strong contraction exhibited in the eStance phase, however, indicates numerically that this periodic orbit is unique. Figure 37 shows that trajectories starting from a range of initial conditions on the $q$-axis are quickly attracted to the unstable manifold of the eStance saddle point, which is tangent to the unstable eigenvector of the eStance critical point $x_1$ on the $q$-axis. In Section 4.1.2, we will see that the locations of this manifold and eStance $v$-nullcline are centrally important to the step phase asymmetry.

### 3.3.5 Duration of eStance but not of other phases depends on trajectory location and motoneuron strength in reduced model

While the analysis in the previous section yields the existence of a periodic orbit, it does not indicate why the stance portion of the orbit alone varies with $d$. We will use the reduced model to understand this drive dependency, since unlike in the full model, the timing of trajectories produced by the reduced model can be precisely determined (since the motoneu-
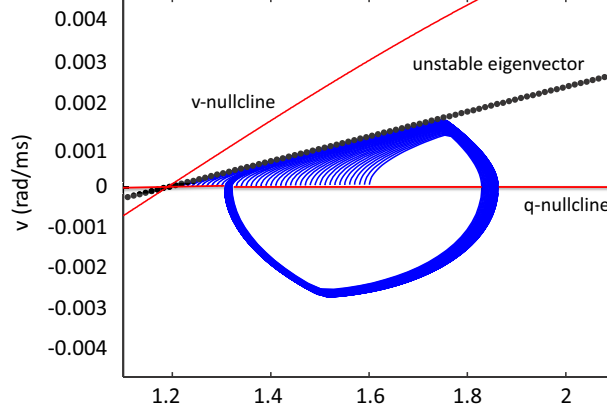
**Figure 37:** *Strong contraction to the unstable manifold of the eStance critical point suggests that the periodic orbit resulting from the Melnikov calculation is unique. The eStance limb nullclines are shown in red and the unstable eigenvector with a black dotted line. A set of eStance initial conditions on the q-axis quickly converge toward the unstable eigenvector of the critical point located where the v-nullcline intersects the q-axis.*

ron output to the limb in each phase is fixed). Recall that drive changes increase both the strength of the motoneuron output and the amplitude of the limb orbit. We will find it useful to vary both the trajectory's position in phase space and the motoneuron output in each of the four phases to analyze which of the four phases are affected by drive changes.

We choose a wide range of initial conditions on the starting manifold for each phase in a neighborhood of where we see these transitions occurring in the original model (see Figure 31). Given an initial condition located on a starting manifold for a phase (either the TTC, the WTC, or a segment on the $q$-axis), system (3.17) can be integrated up to the time when the solution reaches that phase's ending manifold. For instance, the duration of the eSwing trajectory for a fixed drive can be found by setting the output of $Mn\text{-}E$ equal to $m_{eSw}$ and forward integrating from an initial condition lying on the WTC up until the time when the solution hits the $q$-axis. Then, we increase the drive strength (in our reduced model, this means we update the value of $\{m\}$) and record the duration that a trajectory with given initial condition took from beginning to end of that phase. The difference in duration over the range of initial conditions and input strengths in fStance, fSwing, and eSwing is relatively small, with durations ranging over at most a few hundreds

of milliseconds, compared to the eStance durations, which varied from roughly 200 ms to 2200 ms (see Figure 38). In particular, the eStance trajectories with the longest durations
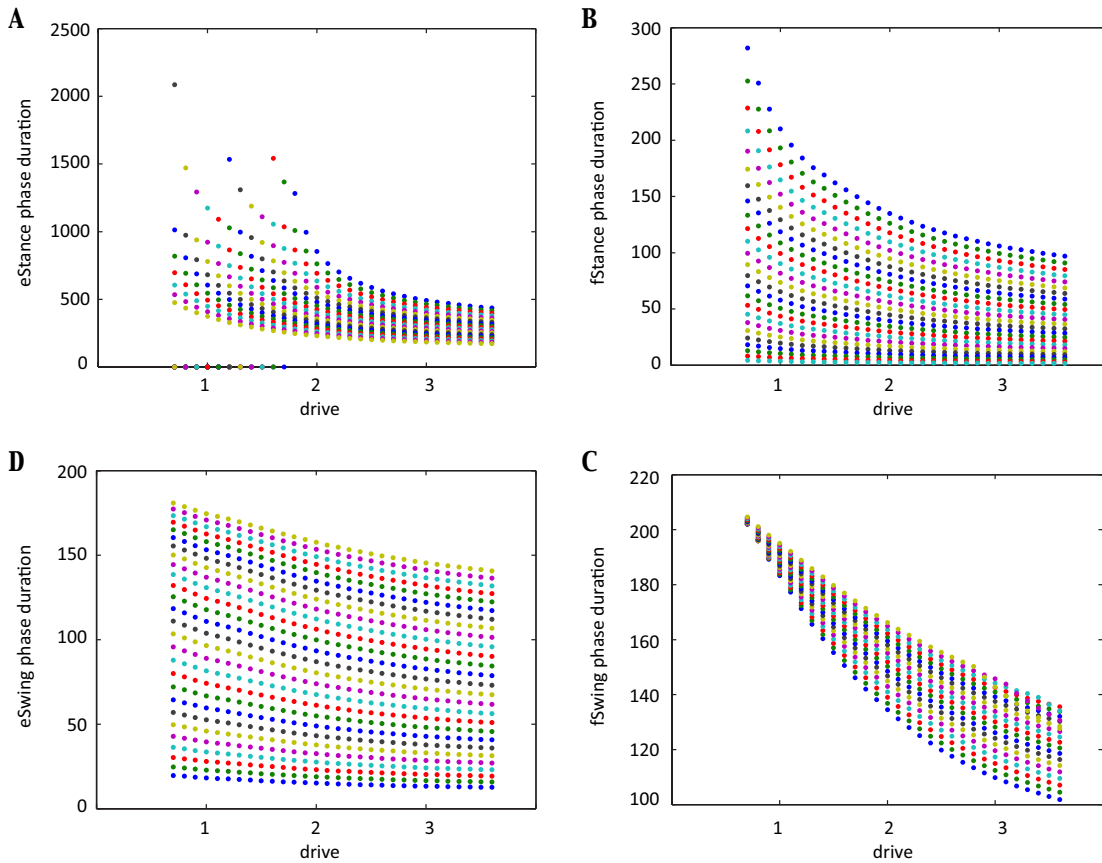


**Figure 38:** *Phase durations are plotted against drive for a range of relevant initial conditions in each of the four phases. (A)-(D) show results for the eStance, fStance, fSwing, and eSwing phases, respectively. The durations of fStance, fSwing, and eSwing change relatively little compared to the eStance duration.*

occurred for small drive values, where the initial conditions chosen lie close to the eStance critical point. In some cases, trajectories starting from certain initial conditions failed to enter the region of positive velocity entirely. The results of these simulations show that eStance phase duration depends strongly on drive. In the next section, we will return to the full model to analyze the source of this asymmetric dependence of phase duration on drive.

## 3.4 DISCUSSION

Given a model consisting of a system of differential equations, simulations can be used to explore model behavior. Dynamical systems analysis can yield insights about which model features are responsible for which aspects of the observed model outputs, what conditions are needed for particular model behavior to occur, and what other sorts of activity might be observed from a model. In this chapter, we have used dynamical systems techniques to analyze important aspects of the behavior of a simplified neuromechanical model of locomotion, a study that we will continue in Chapter 4. These findings were published in [75] and [76].

In Section 3.2, we investigated the difference in the transition mechanisms within the CPG between the case of fictive locomotion, without afferent feedback, and normal locomotion, with feedback. In the latter case, phase transitions occur when excitatory feedback signals allow interneurons within the CPG to escape from cross-inhibition. Thus, we would predict, for example, that providing a small boost in feedback to a suppressed interneuron would be a more effective way to promote a phase change than providing a small boost to a suppressed rhythm generating neuron would be and that decreasing feedback to interneurons would compromise locomotion more drastically than would diminishing feedback to rhythm generators. Since this transition mechanism is driven by the limb component of the system that generates the feedback, we could define transition curves in the phase plane associated with this component, which will be particularly useful in subsequent analysis of model dynamics [76]. Without feedback, the interneurons cannot escape, and hence oscillations can only occur through escape of suppressed rhythm generator neurons in the CPG, which in turn requires a sufficiently large supra-spinal drive. Thus, we explained the simulation result [46] that the range of supra-spinal drives yielding fictive locomotion is more limited than those supporting normal locomotion.

In a half-center type model that generates oscillations, increases in feedback strength can increase the period, by prolonging the activity of the dominant component, or decrease the period, by promoting the onset of activity in the suppressed component. The former effect occurs with transitions through release, while the latter occurs with escape-based transitions [74, 68, 19]. Thus, our identification of escape-based transitions in the neuromechanical

model in both the fictive and normal cases explains simulation results that show a speed-up in oscillations with increased feedback.

The relatively complicated nature of the model led us to reduce the model into a qualitatively consistent form more amenable to dynamical systems analysis (Section 3.3), which required us to determine which model features could be simplified, and in what way, without compromising model dynamics (see also [75]). Given the reduced model, the construction of an existence proof required a detailed exploration of how various model components affect its dynamics. In particular, this investigation led us to an appreciation of the central importance of the limb phase plane, and especially of the differences in nullcline structure within this phase plane across different locomotor phases, for understanding solution behavior. More generally, mathematical analysis of existence, stability, and uniqueness for a biologically observed solution helps verify the relevance of the model that generates this solution, establish the constraints on parameters under which the model is valid, and identify other solutions or changes in solution features that may be expected under certain conditions. Our particular existence and stability argument relied on Melnikov's method and the Poincaré-Bendixson theorem, adapted for the discontinuities occurring at phase transitions in the model, combined with a few numerical calculations. Our existence result required the assumption that a certain closed orbit could be constructed when the motoneuron output function was assumed to be piecewise constant, with values satisfying certain constraints that are discussed in detail within the thesis, and we observed that this assumption holds as long as the supra-spinal drive in the model is not too small. We also found a strong contraction among trajectories within the eStance phase, which appears to yield uniqueness of the periodic solution.

Previously, many models of locomotion have focused on understanding the mechanisms regarding the neurophysiology and the biomechanics separately, but only recently has consideration been given to how the synergy between these elements are generated, including the roles of feedforward CPG outputs and movement-related feedback to the CPG (see e.g. [20] and references therein). Several studies have analyzed resonance and entrainment in relatively simple models, considering the CPG and limb as having intrinsic frequencies (associated with damped oscillations to rest in the latter case) and investigating how the two

interact to set a frequency for oscillations in the full network [34, 37, 81, 70]. Our analysis breaks the network oscillation into four phases. Within stance or swing, transitions between extensor and flexor control occur at the CPG level, depending on the time course of afferent feedback. These CPG transitions cause jumps in the vector field for the limb dynamics, which in turn enable limb velocity to switch sign and lead to transitions between stance and swing phases, with associated alterations in feedback signals. Thus, we see that control of each phase transition is directly impacted by one particular component of the model, the CPG or the muscle-driven limb, yet that component is influenced by the activity of the other. In another closed loop model [55], a simple CPG comprised of two half center oscillators drove the activity of a simple mechanical limb. Phase switching rules (reminiscent of Cruse's behavioral rules for limb coordination [14]) generated by the limb produced sensory signals that overrode switching in the CPG, shortening phase durations to promote locomotor stability when CPG durations were too long. Our model analysis also emphasizes phase transitions driven by limb dynamics, and yields insights into why oscillations exist in the model, how they can be lost as parameters vary, and how phase durations are determined.

In the next chapter, we will reveal how the proximity of the limb trajectory to a saddle point in phase space can be indirectly modulated by drive, creating the dependency of stance phase durations on this parameter. The model's performance after spinal cord injury, under body weight support, and under modulations of feedback strength will be considered. We will utilize our understanding of the mechanisms contributing to model dynamics to explain how various behaviors are produced under these modifications, and, where possible, suggest perturbations that could be implemented to optimize desired dynamics.

# 4.0   MODEL APPLICATIONS

In the previous chapter, we introduced a neuromechanical locomotor model and used dynamical systems tools to analyze its performance under the presence and absence of feedback. Using insights from that analysis, we were able to propose a tractable reduced model and prove existence of a locomotor cycle in that configuration. In this chapter, we will use the framework we have developed to explain how the model captures a few experimentally observed phenomena. First, we will explain how the model responds asymmetrically to changes in drive, replicating an important feature of mammalian locomotion. The reduced model suggests that the drive dependence is constrained to one particular phase of the locomotor cycle (Figure 38), so we will focus our attention on how the pendular dynamics differ in each of the four phases. This analysis will reveal a key relationship between the limb trajectory and a saddle point in the eStance phase that must be maintained in order for oscillations to be supported. Furthermore, the duration of that phase is controlled by the proximity of these two components, which is influenced by drive. These insights enable us to explain the model's response to parameter changes that evoke various applications. For instance, setting the drive parameter equal to zero represents loss of supra-spinal input after spinal cord injury, ceasing oscillations. However, locomotor activity can be recovered by increasing the feedback strength, in part because it restores this key relationship between components at the onset of eStance. This enables us to provide predictions for which feedback channels and muscular structures should be strengthened to promote stable walking after injury. In another application, we vary the strength of the ground reaction force, which decreases the duty cycle by altering this important alignment. This result replicates observations from body weight support experiments that test locomotion under reduced load. Finally, a limbless model which was fit to the same data as the neuromechanical model provides predictions

114

on how input to the CPG is encoded to produce a desired velocity. We will analyze that relationship in this model, expanding the discussion by utilizing the limb system to calculate a different representation of speed.

## 4.1 FAST TRANSITIONS IN SEGMENT DYNAMICS REVEAL SOURCE OF PHASE ASYMMETRY

A key feature of mammalian locomotion regards the way frequency increases occur. As treadmill speed is increased, the step cycle duration decreases, but it does so through changes to stance duration only. In a reduced model where the locomotor phase was naturally separated into four components, dependence of step duration on changes in drive was confined to only one phase in particular. Taking cues from that reduction, we look for differences in the dynamics in each of the four phases in the full model and reveal how the asymmetric response to changes in drive occurs due to a proximity between a saddle point and the limb trajectory in one phase, and why the other phases are insensitive to drive strength.

### 4.1.1 Limb nullclines are oriented differently in each phase

As noted in Section 3.3.1, four important transitions occur in each step cycle that drastically change the limb dynamics. In the previous chapter, we saw that in the reduced model, the eStance dynamics play a critical role in promoting uniqueness of a periodic orbit (Figure 37) and that that phase is particularly sensitive to changes in initial conditions and drives (Figure 38). Building on these observations, we can now characterize the source of the phase asymmetry.

Consider the location of the $q$-nullcline, defined by the set of all $(q, v)$ such that $\dot{q} = v = 0$, and the $v$-nullcline, the set of all $(q, v)$ satisfying $\dot{v} = 0$, of equation (3.5), in the $(q, v)$ plane. Figure 39 shows a segment of the limb trajectory selected within each of the four phases. In each phase, sample points on the trajectory are chosen and the corresponding $v$-nullclines at the associated timepoints are plotted, with colors used to indicate which points and

nullclines go together. The eStance phase, illustrated in Figure 39A, features positively sloped $v$-nullclines, such that the trajectory is in close proximity to the nullcline at the onset of this phase. After the CPG changes dominance from $E$ to $F$, the segment trajectory enters fStance (Figure 39B). Notice that the position of the $v$-nullcline is significantly altered due to the drastic change in motoneuron outputs, and hence in the right hand side of equation (3.5) at the transition from eStance to fStance. When the trajectory crosses the $q$-axis, the velocity of the segment changes sign and the segment enters the swing phase. The ground reaction force terminates at this transition, and the nullcline position in fSwing (Figure 39C) reflects this loss of force; the slope of the $v$-nullcline switches from positive to negative between these two phases. The final plot in Figure 39D exhibits the trajectory and nullclines in the eSwing phase. When the CPG changes dominance between these phases, the extensor motoneuron force term is activated (and the flexor motoneuron force term is deactivated), which is reflected in the altered nullcline position. In the following sections, we discuss in further detail the different dynamics in each phase and use these observations to explain how limb feedback creates the phase asymmetry evident in Figure 26B.

### 4.1.2 Discussion of eStance Dynamics

At the start of eStance, the ground reaction force initiates, which causes the $v$-nullcline to assume the orientation seen in Figure 39A. This configuration has a crucial effect on the activity of the system. We note that increased drive corresponds to larger $Mn\text{-}E$ output, which raises the $v$-nullcline. For smaller drives, and hence smaller $Mn\text{-}E$ output, the $v$-nullcline is lower, and the critical point it forms with the $q$-nullcline lies extremely close to where the trajectory enters this phase. Furthermore, initially $\dot{v} > 0$ and the $v$-nullcline moves down because $Mn\text{-}E$ output decreases over the course of eStance (the output of $Mn\text{-}E$ controls the strength of $M_E$ in equation (3.5)).

This relationship is important for three reasons. The first involves the ability of the model to produce oscillations. If a trajectory enters the eStance phase to the left of the $v$-nullcline, the dynamics in that region will prevent it from completing the eStance phase. Indeed, to the left of the eStance $v$-nullcline, the eStance direction field points down towards

116
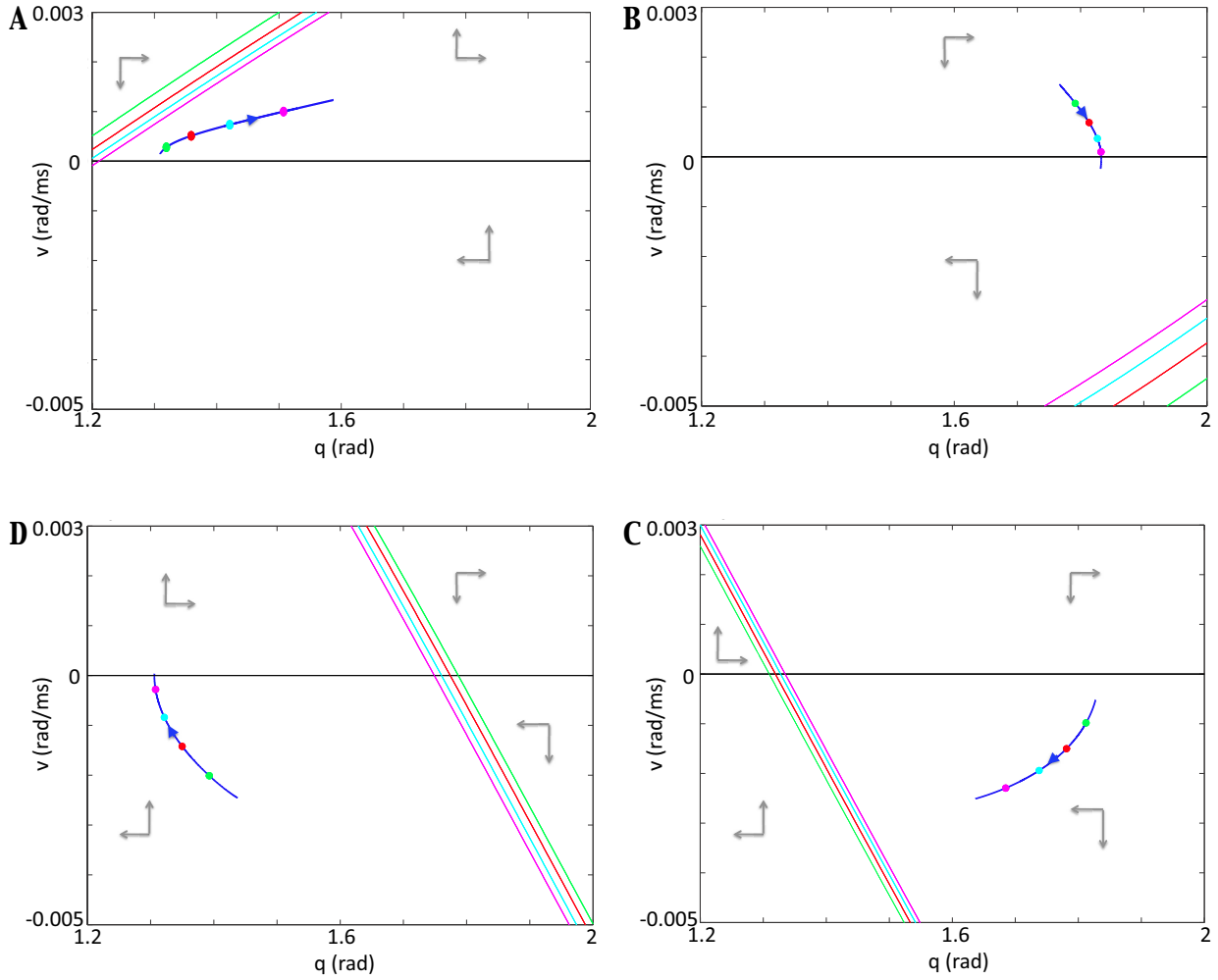
**Figure 39:** *The alignment of the limb trajectory relative to the v-nullcline depends on phase. (A), (B), (C), and (D) display structures in (q, v) phase space in the eStance, fStance, fSwing, and eSwing phase, respectively, with panel ordering selected to reflect the order in which the phases occur, progressing clockwise. In each, the q-nullcline, which is the q-axis, is shown in black. A portion of the trajectory is plotted in blue, with different colored time points highlighted, and the same color is used for each corresponding v-nullcline, since the v-nullcline changes position over time as the output of the active motoneuron changes. Note that the v-nullcline positions differ drastically between phases, due to dominance switching in the CPG and the influence of ground contact.*
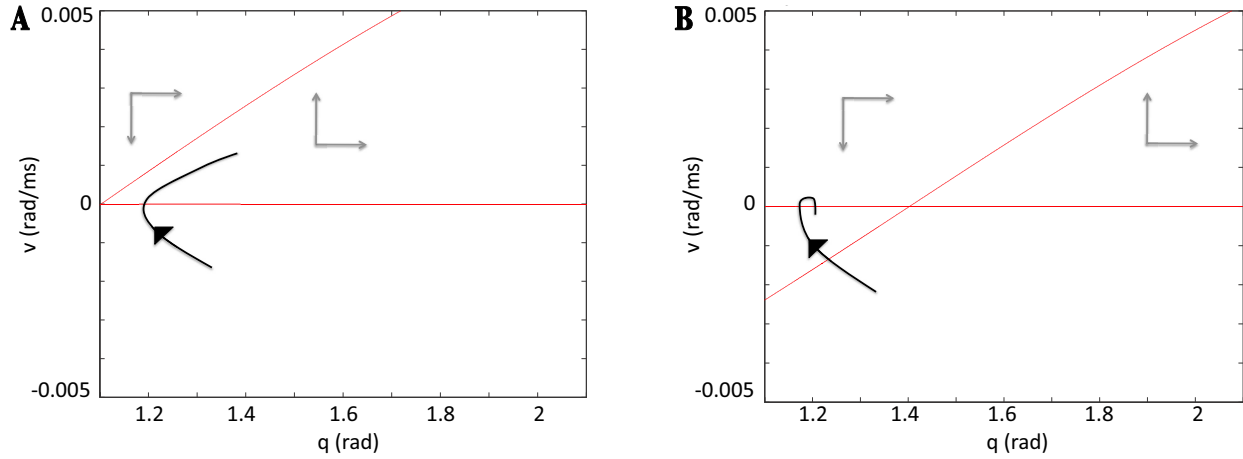
**Figure 40:** *Schematic illustration of the possible relationships the eStance v-nullcline can have with the limb trajectory at the onset of eStance. (A) The limb trajectory moves up and to the right through phase space when it enters eStance to the right of the eStance v-nullcline. (B) To the left of the v-nullcline, the vector field points down and to the right. Thus, the limb cannot proceed if it tries to enter eStance to the left of the eStance v-nullcline.*

the $q$-axis (Figure 39A, and the eSwing direction field points up towards it (Figure 39D). Thus, the limb remains pinned at the $q$-axis, which interrupts oscillations. This effect is the reason why both the original and reduced models fail to produce oscillations for small drives. If we track a limb trajectory generated by the full model with sufficiently small drive and corresponding small $Mn\text{-}E$ output, from an initial condition on the $q$-axis to the right of the $v$-nullcline at the start of eStance, the trajectory will progress through eStance, fStance, fSwing and eSwing and then will leave eSwing and return to eStance to the left of the $v$-nullcline. In terms of the calculations in the previous section, the Melnikov function would be positive for such drive values. A schematic illustration of this oscillation failure mechanism is shown in Figure 40.

The second reason that this positioning is important is that it is the key feature in establishing the phase asymmetry. The time of passage for a trajectory to exit the neighborhood of a saddle point from an initial condition within that neighborhood becomes arbitrarily large as the initial condition approaches the saddle point. Furthermore, the position of the

$v$-nullcline bounds the growth in $v$ even when the trajectory moves away from the critical point, slowing the rate at which the limb can access higher velocities, reach the TTC, and exit the eStance phase. As drive is increased, however, the nullcline is lifted away from the location of eStance onset, and thus the influence it has on the timing of this phase will be minimal. Therefore, the duration of eStance can vary significantly with changes in drive. This crucial relationship of the orientations of the trajectory and the $v$-nullcline does not exist in the other phases (Figure 39B-39C). The presence of ground reaction force creates a unique trajectory/nullcline alignment that opposes an increase of acceleration, which is essential to the asymmetric phase response to changes in drive. We note that changing the strength of the feedback in the model, particularly the $Ib\text{-}E$ feedback term, can also scale the extent of the asymmetry in phase durations, again by altering the trajectory/nullcline alignment.

The third role played by the configuration of the trajectory relative to the $v$-nullcline at the onset of the eStance phase is that this configuration yields the strong contraction of trajectories from different initial conditions on the $q$-axis observed in eStance in Section 3.3.4; see Figure 37. This contraction results because near eStance onset, but away from the $v$-nullcline, $dv/dq = \dot{v}/\dot{q} = \dot{v}/v$ is very large, since $v$ is near 0 and $\dot{v}$ is not. Thus, trajectories entering eStance away from the eStance critical point are all funneled strongly upward, toward the $v$-nullcline, until $\dot{v}$ and $v$ become closer in size.

One final observation, which we exhibited for the reduced system in Section 3.3.4, involves the presence of an unstable manifold that lies in the eStance domain. Linearizing around the critical point of system 3.5 at fixed values of $Mn\text{-}E$ indicates that the critical point in eStance is a saddle. The unstable eigenvector has a positive slope and lies between the $q$-axis and the $v$-nullcline, and near the critical point, it lies tangent to the unstable manifold. For simplicity, and because we saw how the unstable eigenvector remains a good approximation of the manifold throughout the eStance phase in the reduced case, we use the unstable eigenvector, rather than the actual unstable manifold, in the following figures. As $Mn\text{-}E$ changes, the $v$-nullcline and critical point shift, and hence, so does the location of the unstable eigenvector. Figure 41 exhibits a family of eigenvector and limb trajectory locations in $(q, v)$ space with corresponding colors for various timepoints throughout this phase. For small

119
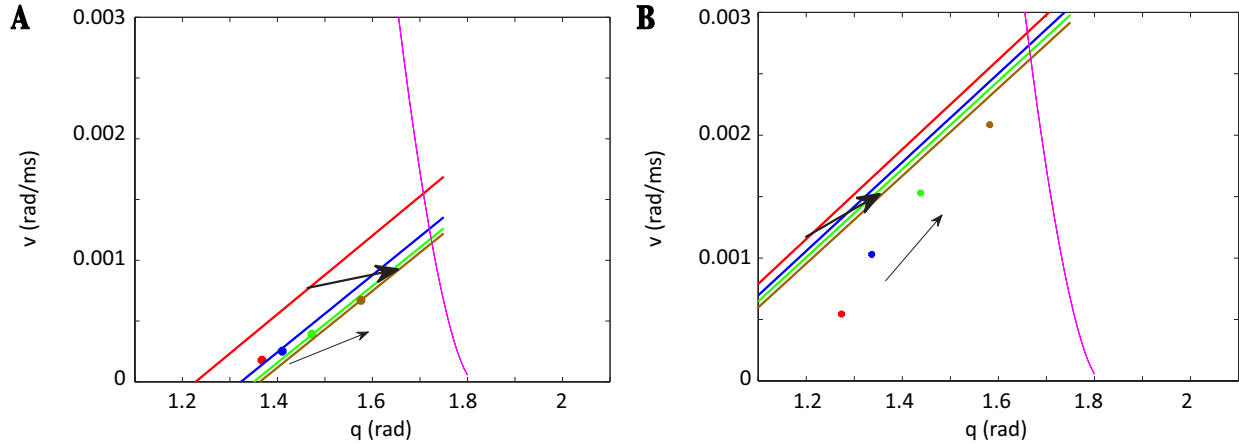
**Figure 41:** *The location of the unstable eStance eigenvector determines the position where the limb trajectory crosses the TTC. Colored dots on the limb trajectory are plotted at various time points with their corresponding unstable eigenvector. The TTC is shown in magenta. (A) For a small drive value, hence, small $Mn\text{-}E$ output, the unstable eigenvector lies at low velocities, and the trajectory lies very close to these eigenvectors until it crosses through the TTC. (B) For a large drive value, hence, large $Mn\text{-}E$ output, the unstable eigenvector is far from the initial position the trajectory takes in eStance. The trajectory is pulled upwards toward the eigenvector and thus crosses the TTC at a higher velocity than in the small drive case.*

drives (Figure 41A), since the trajectory enters the eStance phase close to the critical point, the trajectory quickly converges to the unstable eigenvector, as discussed above. For larger drives (Figure 41B), the eigenvector, like the nullcline, is lifted away from the trajectory at eStance onset. The trajectory flows toward this manifold as it travels through eStance, until it crosses the TTC at higher velocities than were reached in the small drive case. Thus the location of intersection between the unstable eigenvector and the TTC plays a role in where the limb will begin the fStance phase. We will see in the next subsection that this entry location plays a important role in the limb's ability to reach the swing phase.

### 4.1.3 Discussion of fStance Dynamics

As in the eStance phase, critical points computed at specific time points in fStance are saddle points. In fStance, however, the critical point is on the exit manifold (the $q$-axis) of the phase, not the entrance manifold (the TTC), and thus there is no risk that the trajectory

120

will be delayed at the onset of the fStance phase. The stable eigenvector corresponding to the fStance saddle point for each $Mn$-$F$ output slices through the fStance region of $(q, v)$ phase space. Figure 42 shows a collection of these eigenvectors, signifying their movement over time as changing $Mn$-$F$ output alters the position of the critical point and $v$-nullcline. If a trajectory entered fStance above the stable manifold, it would continue to travel above and along the manifold toward the $q$-axis. Before it could reach the axis, however, it would have to cross the fStance $v$-nullcline, and $\dot{v}$ would change from negative to positive. Thus, the trajectory would move in a direction of increasing $v$ and increasing $q$, remaining forever bounded away from the $q$-axis and hence unable to complete a transition to the fSwing phase. In addition, if the trajectory entered the fStance below, but sufficiently close to the stable manifold, that trajectory could still complete the fStance phase, but be significantly slowed before reaching the $q$-axis, yielding a very long fStance duration.

However, as discussed in the previous subsection, the limb trajectory travels throughout the eStance phase tracking close to, but below, the unstable manifold, which lies well below the fStance stable manifold. Indeed, although the eStance unstable eigenvector crosses the TTC with larger $v$ for larger drives, the stable eigenvectors in fStance in the large drive case (Figure 42B) are also shifted farther upward than the eigenvectors in the small drive case (Figure 42A), allowing completion of the fStance phase despite larger initial velocities. Thus, the limb is bounded away from the fStance stable manifold, and hence is able to complete the fStance phase with timing that is not influenced by the saddle point.

In Section 4.1.6, we shall verify numerically that the fStance initial conditions, influenced by the contraction in the eStance phase, keeps the fStance phase durations relatively independent of drive strength despite these possible complications.

### 4.1.4 Discussion of fSwing Dynamics

Unlike the stance phases, the critical point for the fSwing vector field is a stable spiral. In this case, $v$-nullcline proximity to the trajectory does not greatly impact the trajectory of the limb. Indeed, if $Mn$-$F$ output is sufficiently weak, the trajectory could cross through the $v$-nullcline, which would change the dynamics from decreasing to increasing velocity. Even
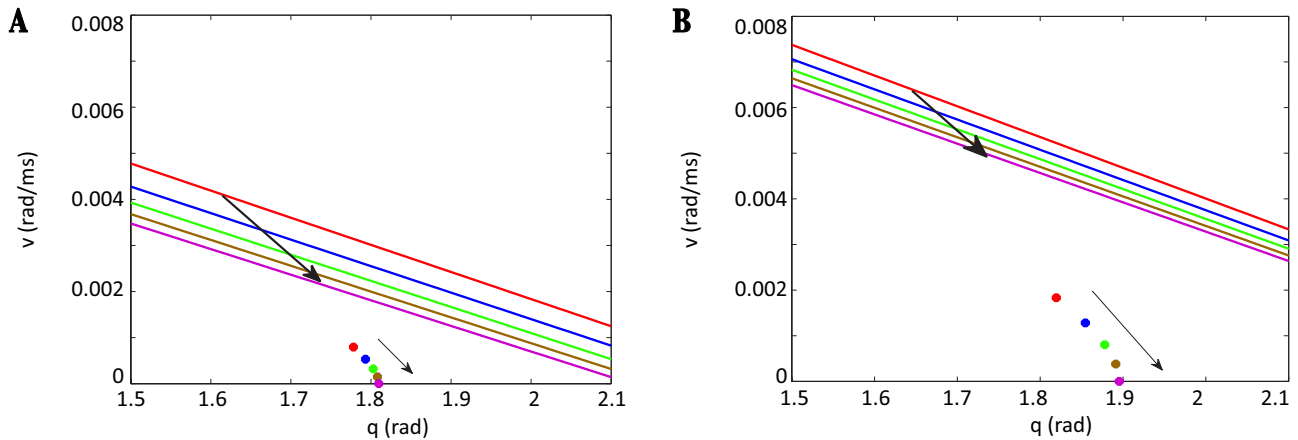
**Figure 42:** *The positions of the stable eigenvectors and the limb trajectory change with drive strength. (A) Small drive leads to small $Mn$-$F$ output and stable eigenvectors that lie in a region of small positive velocity, but the limb trajectory enters this phase far below them. (B) Large drive, with large $Mn$-$F$ output, yields stable eigenvectors shifted farther upward than in (A), such that trajectories with larger initial fStance velocities still lie below them. Time points on the limb trajectory are shown with dots, while the color-coordinated lines are the corresponding stable eigenvectors.*

with such a change, however, the trajectory would continue to approach the WTC and make the transition to the eSwing phase, and oscillatory activity would not be compromised.

To investigate why the duration of the fSwing phase remains independent of drive changes, we evaluated $\dot{v}$ over a range of $q$ and $v$ values for two choices of $Mn$-$F$, shown in Figure 43. Figure 31 exhibits the range of initial conditions for this phase obtained by model simulations as drive is increased, which lie on the $q$-axis between 1.8 and 1.95. As exhibited in that figure, we have argued that as drive increases, the oscillation trajectory enters fSwing at a larger $q$, and thus larger $Mn$-$F$ corresponds to oscillations with larger amplitudes than those resulting from small drive simulations. Thus, the trajectory must travel a farther distance to the WTC than would a smaller drive trajectory. But, since the larger drive trajectory initial condition has a larger $q$-component and hence yields a larger value of $K\cos(q)$, as well as a larger $Mn$-$F$, $|\dot{v}|$ becomes larger as drive is increased, and the necessary distance in $q$ can be covered more quickly. On the other hand, the velocity that a large drive trajectory can achieve cannot become extremely large relative to the velocity

of a small drive trajectory. Suppose that the muscle force is relatively constant, say with a value $\hat{M}$, and consider the function $\hat{L} = v^2/2 - K/I\sin(q) - \hat{M}/Iq$. The level curves of this function ($\hat{L} = $ constant) are curves in phase space that have a curvature that is similar to the shape of the trajectories in this phase (see Figure 43). As this constant decreases, the level curves lie closer to the $q$-axis. Notice that the function $\hat{L}$ has a time derivative $d\hat{L}/dt = v\dot{v} - K/I\cos(q)\dot{q} - \hat{M}/I\dot{q} = -bv^2/I$. Since $d\hat{L}/dt$ is negative, solutions to system (3.5) travel in the direction of lower $\hat{L}$, i.e. toward the $q$-axis. Thus, the level curve on which a trajectory begins the fSwing phase provides a lower bound for the path of that trajectory in phase space, under the assumption that $M_F$ remains relatively constant during fSwing, which holds as long as the right branch of the $Mn$-$F$ voltage nullcline is not strongly sloped. Even for a very negative $\hat{M}$, corresponding to a large drive and $Mn$-$F$ output, the trajectory enters fSwing on a level set that crosses the WTC with velocity larger than -0.005, and thus is bounded away from very negative velocities (Figure 43). Hence, large drive trajectories cannot move significantly faster than slowly driven trajectories.
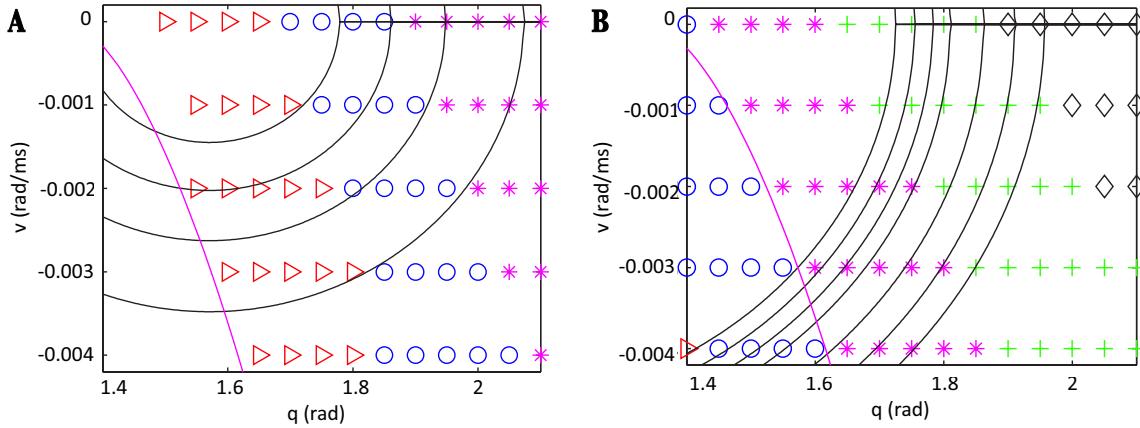


**Figure 43:** *$\dot{v}$ values at sample $(q, v)$ points and level sets of $\hat{L}$ in the fSwing phase for small $Mn$-$F$ (A) and large $Mn$-$F$ (B). In both plots, black diamonds, green plus signs, magenta stars, blue circles, and red arrows correspond to $\dot{v}$ values within (+/-) 5e-6 of -5e-5, -4e-5, -3e-5, -2e-5, and -1e-5, respectively. Level curves of $\hat{L}$ are plotted in black, and smaller $\hat{L}$ values correspond to level curves with smaller radii. The WTC is plotted in magenta. Initial conditions for this phase lie on the q-axis with varying angles. For the drive shown in (A), the oscillation trajectory would begin fSwing closer to the WTC but travel more slowly than in (B), where the trajectory would enter fSwing at a larger angle but travel faster. For constant $Mn$-$F$ output, trajectories move in the direction of decreasing $\hat{L}$.*

### 4.1.5 Discussion of eSwing Dynamics

As in fSwing, the critical point in the eSwing system is a stable spiral. Analogous to the discussion we presented in the previous section, an investigation of the strength of $\dot{v}$ over the eSwing domain can be performed. Figure 31 exhibits the initial entrance conditions to this phase, which are shifted slightly from the WTC. The vector field varies very little as $Mn\text{-}E$ is increased, and again, the larger amplitude oscillations that occur for larger drives need to travel a larger distance to complete the phase (from a more negative $v$ up to $v = 0$) but do so faster because they travel through regions with larger $\dot{v}$; see Figure 44. Recall that the relationship between where the trajectory exits eSwing and the location of the eStance critical point is crucial for the allowing limb motion to continue. There are two factors that ensure that these points maintain the necessary relationship for oscillatory behavior to be continued as drive is increased. The first is that for larger drives, the motoneuron output is larger, and thus the eStance $v$-nullcline is higher, with a critical point whose angle is much smaller. In addition, for larger drives, the eSwing trajectory travels on level sets of a function that have a steeper slope than in the small drive case. Again, if the muscle force is relatively constant, corresponding to little change in $Mn\text{-}E$ output while it is active, say with a value $\bar{M}$, then the function $\bar{L} = v^2/2 - K/I \sin(q) - \bar{M}/Iq$ has time derivative $d\bar{L}/dt = -bv^2/I$. So limb trajectories travel in the direction of lower $\bar{L}$, curves that have smaller radii. Thus, the curve that the eSwing entrance point lies on forms a lower bound in phase space for the solution trajectory, and if the level curve it lies on intersects the $q$-axis to the left of the eStance critical point, we can guarantee that the trajectory will have that relationship as well (which is necessary for oscillations, see the discussion in Section 4.1.2).

For larger $\bar{M}$, the slope of these levels sets is much steeper, so although trajectories start farther from the $q$-axis (and hence, could travel to very low $q$ values since $\dot{q} = v$), they are constrained by steeper level sets of $\bar{L}$, which ensures that trajectories exit the eSwing phase to the right of the eStance critical point.
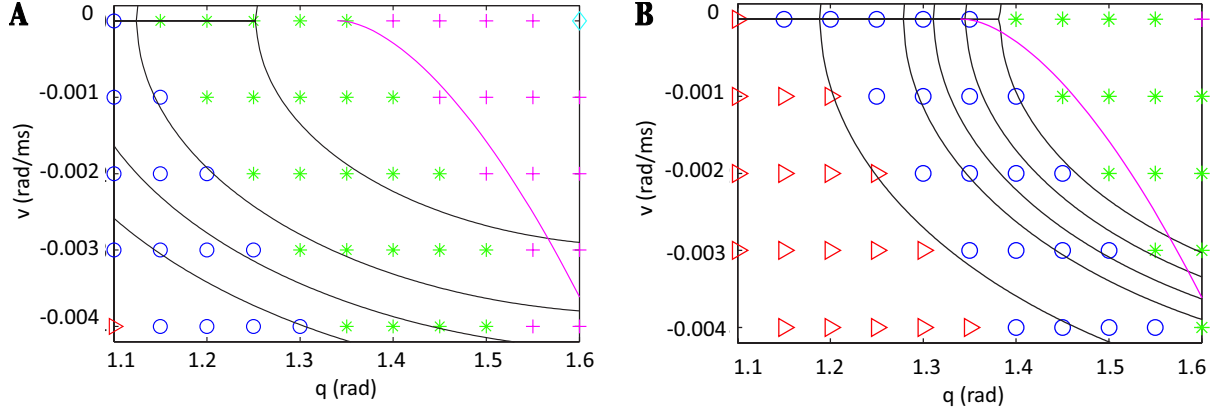
**Figure 44:** *$\dot{v}$ values for a sample of $(q, v)$ points and level curves in the eSwing phase for small $Mn\text{-}E$ (A) and large $Mn\text{-}E$ (B). Magenta plus signs, green stars, blue circles, and red diamonds correspond to $\dot{v}$ values within (+/-) 5e-6 of 1e-5, 2e-5, 3e-5, 4e-5, and 5e-5, respectively. Level curves of $\bar{L}$ are plotted in black and the WTC is plotted in magenta. Ignoring the transient, trajectories enter this phase on the WTC. In (A), trajectories begin closer to the q-axis but travel more slowly than in (B), where trajectories begin farther from the q axis, but travel faster. The slope of the level curves becomes steeper as drive increases; thus, there is a bound on how small the q values reached by large drive trajectories can be.*

### 4.1.6 eStance is the sole contributor to the phase asymmetry

Now that we have fully described the dynamics in each phase, we verify that the asymmetry is almost completely confined to the eStance phase, not to the stance phase in its entirety, as shown numerically in Figure 45.

In these sections, we considered the dynamics in four separate phases – eStance, fStance, fSwing, and eSwing – of the locomotor cycle. In all cases, changes in drive corresponded to changes in motoneuron output, which influenced the position of the limb's $v$-nullcline. This position was crucial in eStance, since the relationship between the limb trajectory and the saddle point in that phase controlled phase timing and prevented oscillations if a certain configuration was not supported. The alignment was less crucial in the other three phases. In fStance, we showed that the trajectory remained far from its stable manifold and hence could complete that phase due to entry constraints, produced by the unstable manifold in eStance. In fSwing and eSwing, critical points corresponded to stable spirals, and we used level curve arguments in those cases to bound the growth of the trajectory away from regimes
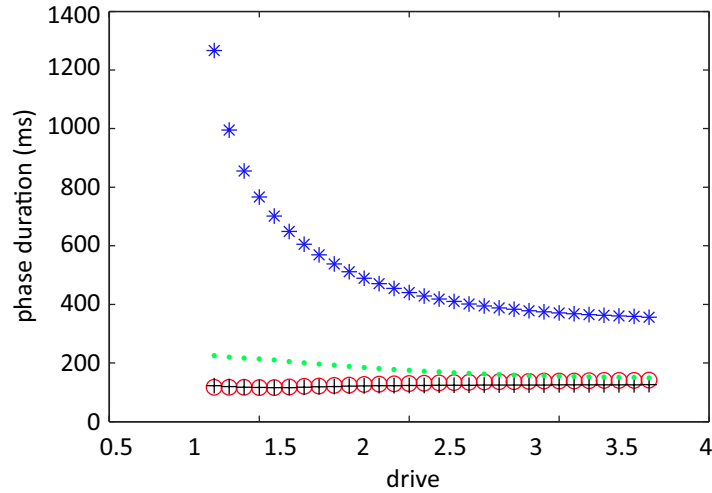
**Figure 45:** *Durations of each of the four subphases are plotted against drive strength. The duration of eStance is shown in blue, fStance in black, fSwing in green, and eSwing in red. The phase asymmetry shown in Figure 26B is almost entirely restricted to the eStance phase, due to the unique nullcline/trajectory alignment that occurs for small drive values.*

where $v$ was sufficiently large. These three phases were insensitive to drive changes due to compensation between distance and speed – large drive orbits had larger amplitudes than orbits corresponding to small drives, but the trajectories traveled through regimes where $v$ was larger.

## 4.2  INCREASED BODY WEIGHT SUPPORT DECREASES DUTY CYCLE

Load plays a role in shaping motoneuron output during stepping, and changes in load can occur instantaneously, such as in assisted walking, or gradually, due to weight loss [36]. Experiments where various percentages of body weight are unloaded using support from an apparatus can be performed on human subjects to investigate how the body adapts to load changes. Data from these studies indicate that the duty cycle, that is, the ratio of stance duration to cycle duration, decreases as body weight support is increased [36, 63],

and in air stepping, when the body is 100% supported, the stance duration does not change significantly with increases in speed [36].

We tested the Markin model to verify whether it supported these results. Figure 46 shows results of the dynamics of the system with full, half, and no ground reaction force over a range of drives to see how load changes affect the durations of the swing and stance phases. As the magnitude of the ground reaction force term is decreased, the $v$-nullcline in the eStance phase loses its positive slope and becomes oriented similarly to the eSwing $v$-nullcline. By reducing the size of the ground reaction force, we eliminate the nullcline-trajectory alignment at the start of eStance. This alteration removes the drive-dependence of the stance duration, with no effect on swing duration. Thus the model replicates experimental observations, and verifies our claim that the presence of ground reaction force opposes an increase in acceleration at the onset of stance, and is essential to set up conditions under which the presence of feedback can generate the asymmetric phase response to changes in drive.
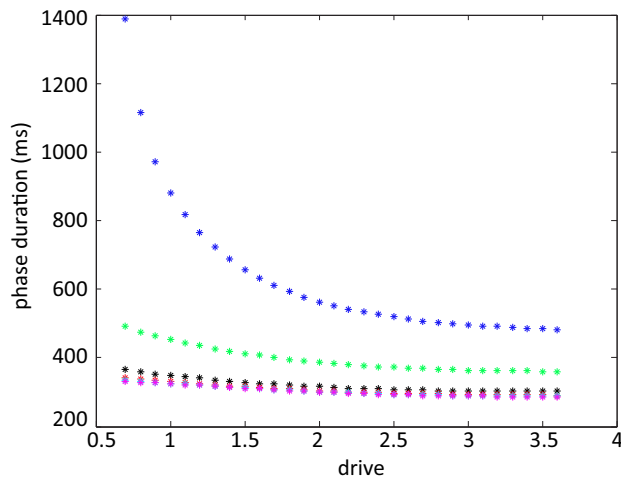


**Figure 46:** *Stance and swing durations for various ground reaction force magnitudes ($M_{GRmax}$) are plotted against drive. The stance durations for full, half, and no GRF are plotted in blue, green, and black, respectively. The swing durations are plotted in red, cyan, and magenta and the resulting curves lie on top of each other. By reducing the impact of the ground strike force, the dependence of stance duration on drive (upper curves) is lost. The swing durations (lower curves) remain unaffected by this change.*

## 4.3   RECOVERY OF RHYTHMICITY AFTER SIMULATED SPINAL CORD INJURY (SCI)

Another open question about mammalian locomotion relates to the recovery of locomotor rhythmicity after spinal cord injury (SCI). A complete spinal transection removes supraspinal inputs to the CPG, which, it is believed, leaves the CPG too weakly excited to maintain its rhythmic output. Locomotor training, a combination of training and pharmacology, or applied spinal cord or afferent stimulation can partly restore locomotor function in cats [58, 4, 60, 24, 59, 61, 78]. While this recovery likely involves potentiation of afferent feedback signals, the details of the mechanism underlying this recovery remain to be elucidated.

Whether augmented feedback could reestablish oscillations after SCI was considered in this neuromechanical model in [46]. In that paper, they emulated injury by setting the drive parameter to zero, which ceased oscillations. They then proportionally increased the weights of feedback to all model neurons, and found that although this could reestablish rhythm generation in the CPG, the limb "fell" within the first few steps. Only when the weight of $Ib$ strength was increased five-fold and the weights of $Ia$ and $II$ were increased by 31% did the model demonstrate stable movement. A comparison of the limb orbits in the normal case ($d$=1.4 under baseline feedback) and after SCI ($d$=0 with disproportionally increased feedback strengths) is shown in Figure 47A. The limb orbit in the SCI case has a significantly smaller amplitude than in normal locomotion, and exhibits a "dip" in the trajectory in the stance phase. We wish to address how the feedback increase accomplishes this goal and to clarify the role of specific feedback components in this recovery. In Section 4.3.1, we propose an argument that reveals the mechanism responsible for oscillations under this adjustment to the system. In Section 4.3.2, we show how this feedback increase alters the qualitative form of the oscillation and the location of the transition curves defined in the previous chapter.

### 4.3.1 CPG transition mechanisms under SCI

When descending input is removed and feedback is increased, how do CPG neurons coordinate their activity to generate an oscillation? Does this adjustment recover the $In$ escape mechanism present in the full system? Or, since removing drive reduces the excitation from the active $RG$ to the corresponding $In$ and hence the inhibition to the silent $RG$, perhaps the mechanism controlling SCI oscillations is through $RG$ escape, which we observed when we reduced excitation in a different way, through removing the feedback. It is also possible that the oscillations are due to an entirely different, hybrid mechanism. In this subsection, we explain why, after removing the drive, increasing the feedback strength to a sufficiently large value in fact recovers oscillations controlled by the $In$ escape mechanism.

First, suppose we set $d = 0$ and initialize the limb with initial conditions corresponding to a point on a normal locomotor oscillation, existing for some $d > 0$, in either the eStance or fSwing phase (recall that eStance refers to the part of the stance phase with extensor neurons active, with similar definitions for other phases, as introduced in Section 3.3.1). A phase transition, to fStance or eSwing respectively, requires a change in which $Mn$ is active, which in turn must follow from a switch of active and silent neurons in the CPG. Letting $d = 0$ raises the $RG$ $V$-nullclines, such that fixed points move to more negative $V$ values relative to the $d > 0$ case, for each fixed feedback value. Since the $RG$ could not escape from the silent phase with the original drive, this change in nullcline position implies that they certainly cannot do so with $d = 0$. Moreover, the nullcline change weakens the output of the active $RG$ and hence of the active $Mn$. The weaker $Mn$ output reduces the magnitude of the limb velocity and correspondingly of the feedback signals to the CPG, making it harder still for the silent $RG$ to escape and become active. For these weaker feedback signals, the only two possibilities are that the silent $In$ escapes and causes a phase transition or limb velocity $v \to 0$ before a phase transition occurs, since the weaker feedback also may prevent $In$ escape.

We observe both of these events in simulations, depending on initial conditions. In the former case, although the CPG makes a transition due to $In$ escape, we still cannot guarantee that an oscillation will occur, because the fStance to fSwing or eSwing to eStance phase

transitions may be compromised, as we explore in the next subsection. For the remainder of this subsection, we focus on the latter case, supposing that in the absence of supra-spinal drive, no phase transition can occur. We now explain why, if feedback strengths are increased enough to restore CPG phase transitions, these transitions will still occur through $In$ escape. To do so, we suppose that we increase proportionally the weights $w_{i,j}$ of all feedback terms in the model and consider the same initial condition as previously. The stronger feedback results in lowered $RG$ $V$-nullclines with less negative $V$ values at fixed points and also increases $\dot{V}$ for the $In$s. At the larger voltage associated with its new nullcline, the active $RG$ provides a stronger output to its $Mn$, which results in an increased limb speed and helps push the feedback amplitudes $fb_i$ back toward their $d > 0$ values. If the feedback $\Sigma_i w_{i,j} fb_i$ to a silent $In$ becomes as strong as it was with $d > 0$, then the $In$ can escape (recall that the $In$s do not receive supra-spinal drive). However, in this case the total input to the silent $RG$ would be given by this $d > 0$ feedback signal alone (and no drive), and hence would be smaller than the original case where it received $d > 0$ as well. Since the $RG$ could not escape even with the original signal (drive plus feedback), it certainly will not be able to do so given this new, weaker signal present with drive removed. While this argument is not precise, because the limb and feedback signals will undergo altered time courses with $d = 0$ relative to the $d > 0$ case, the main idea should nonetheless be clear: even when the feedback signal to the silent $In$ is increased enough to allow it to escape, the loss of drive results in a weaker feedback signal to the silent $RG$, relative to that with drive present, which maintains its suppressed status, and hence CPG phase transitions remain under $In$ control when increased feedback weights restore locomotor oscillations in the model.

In summary, there is a positive minimal feedback strength that is required for one or more CPG phase transitions to take place in the absence of supra-spinal drive. While the strength needed depends on initial conditions, those transitions that occur will do so via $In$ escape. In the next subsection, we consider the possibility of sustained oscillations in the absence of supra-spinal drive.

### 4.3.2   Limb phase plane dynamics under SCI

By plotting the dynamics in limb phase space, we can recast the concept of $In$ escape in a different light. Provided that the trajectory transitions through each phase, that is, hits each switching manifold in succession, the system will perform a successful oscillation. By increasing the feedback after SCI, we alter the position of the transition curves from the normal case. In the full system, the TTC is calculated by the equation $FB_{In\text{-}F} = FB_{crit}$, where specifically, $FB_{In\text{-}F} = w_{Ia\text{-}F,In\text{-}F}Ia\text{-}F + w_{II\text{-}F,In\text{-}F}II\text{-}F$. Increasing the strength of the feedback after SCI means changing $w_{Ia\text{-}F,In\text{-}F}$ and $w_{II\text{-}F,In\text{-}F}$ to larger values, $w^{SCI}_{Ia\text{-}F,In\text{-}F}$ and $w^{SCI}_{II\text{-}F,In\text{-}F}$. Thus, the TTC satisfies a new equation, $FB_{crit} = w^{SCI}_{Ia\text{-}F,In\text{-}F}Ia\text{-}F + w^{SCI}_{II\text{-}F,In\text{-}F}II\text{-}F$, the right hand side of which is still just a function of $(q, v)$, but with updated coefficients. The WTC is analogously affected. Figure 47A shows the location of these curves after SCI, which have a closer proximity to one another than in the normal case, shrinking the range of $q$ values over which the limb oscillates. By identifying this compression of transition curves, our analysis has revealed that it is the change in the source driving the $In$ escape mechanism in SCI that results in a smaller amplitude oscillation.

By turning next to the relationship between the trajectory and the $v$-nullcline in phase space, we can identify an important mechanism through why oscillations can fail and can also explain why velocity decreases slightly during part of the eStance phase in SCI. Figure 47B shows the $v$-nullcline positions at a sequence of time points during the eStance phase, along with color coordinated dots indicating the position of the trajectory when each nullcline is defined. In the eStance phase, $Mn\text{-}E$ is active while $Mn\text{-}F$ is not; increasing (decreasing) the $Mn\text{-}E$ output shifts the $v$-nullcline upward (downward) in phase space. To the left of a particular $v$-nullcline, $\dot{v}$ is negative, and to the right of a particular $v$-nullcline, $\dot{v}$ is positive. Thus, if a trajectory enters the eStance phase to the left of this nullcline, it immediately exits the phase, and the system will not produce an oscillation (see the discussion in Section 4.1.2). To prevent this phenomenon from occurring, the output of $Mn\text{-}E$ has to be sufficiently strong at the transition from eSwing to eStance to allow the limb trajectory to enter on the right side of the $v$-nullcline and accelerate away from the $q$-axis. In SCI, the output of $Mn\text{-}E$
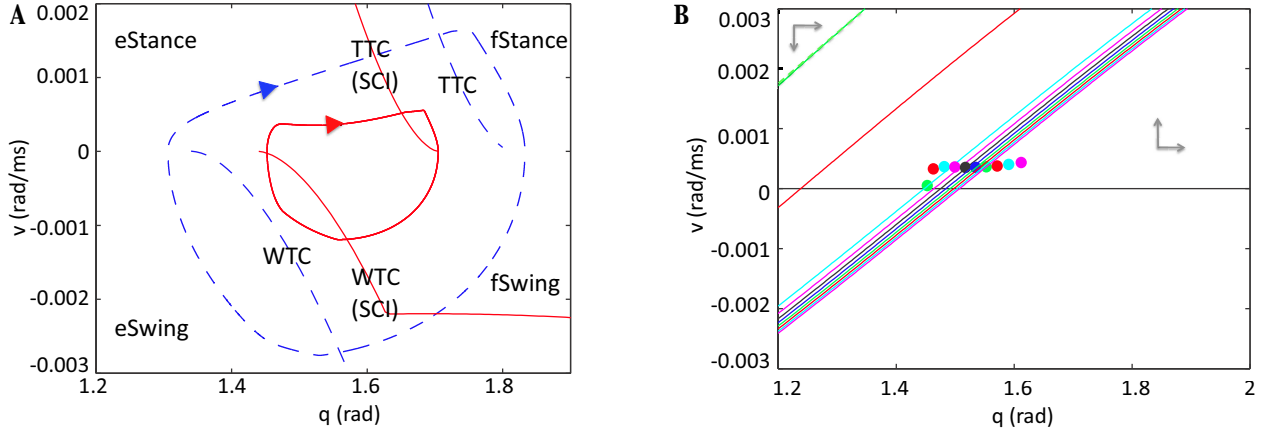
**Figure 47:** *Limb dynamics changes quantitatively and qualitatively after SCI. (A) Limb trajectory and transition curves under normal conditions (blue dashed) and SCI (red solid). By increasing the feedback strength, the transition curves shift, producing an oscillation of smaller amplitude as well as a qualitatively different velocity profile during eStance. (B) eStance v-nullclines and limb position in phase space at different timepoints are indicated with corresponding colors. The earliest time points and nullclines are the farther to the left and are colored green, red, and cyan. A quick drop in the v-nullcline near the onset of eStance, between the red time point and the cyan time point, causes the convex orbit shape seen after SCI.*

is weaker than in normal walking, since the CPG receives no drive in the former case, as discussed in subsection 4.3.1. Increasing the feedback strength, however, increases excitatory input to the CPG and to $Inab\text{-}E$, which results in stronger $Mn\text{-}E$ output. Hence, increasing the feedback terms shifts the $v$-nullcline upwards, so that the trajectory and $v$-nullcline have a relationship that allows the limb to proceed through the eStance phase. In summary, for the recovery of oscillations under SCI, feedback must be strong enough to achieve two effects: it must allow $In$ escape to occur and it must, via effects on $Mn\text{-}E$ output, allow the limb to achieve a positive velocity at the onset of the stance phase.

In Figure 47B at eStance phase onset, $Mn\text{-}E$ output is sufficiently strong such that the $v$-nullcline (indicated in green) is high enough to allow the trajectory to enter the eStance phase. Shortly after this event, however, feedback $Ib\text{-}E$ shuts down (due to decreased input from $Mn\text{-}E$) which causes the $v$-nullcline to drop significantly. The nullcline does stabilize, because of the saturating form of the $Mn\text{-}E$ output function, as is also evident in Figure 47B. By the time this occurs, the limb trajectory lies to the left of the nullcline (e.g., light blue

dot and curve), but it has been able to accelerate to sufficiently large $v$ values before this reversal occurs. Thus, although the limb must travel with decreasing velocity, since $\dot{v} < 0$ in this region, it is able to cross to the right of the $v$-nullcline where $\dot{v} > 0$ and avoid hitting the $q$-axis, which would have prevented it from completing the rest of the phase. Once the trajectory crosses the $v$-nullcline, it maintains an increasing velocity until it reaches the TTC to complete the eStance phase. This transient switch to $\dot{v} < 0$ causes the concave shape of the trajectory in the case without supra-spinal drive, displayed in red in Figure 47A.

Markin et. al. noted that increasing the feedback weights quickly reestablished oscillations, but that the movement of the limb remained unstable until $Ib$-$E$ was increased more strongly (five fold) than $Ia$ and $II$-$F$ (which were increased by 31%) [46]. Our analysis elucidates why $Ib$-$E$ is the optimal feedback to increase. Recall that force-dependent $Ib$-$E$ is active only when the extensor neurons are. Thus, it does not contribute to the location of the WTC, since this curve is defined by the feedback to $In$-$E$ when $In$-$E$ is silent. It also does not affect the location of the TTC, which is a function of $Ia$-$F$ and $II$-$F$. However, since it is active while $RG$-$E$ is, $Ib$-$E$ provides additional excitatory input to $RG$-$E$, $PF$-$E$, and $Inab$-$E$ and therefore indirectly to $Mn$-$E$. Thus, strongly increasing $Ib$-$E$ retains the qualitative structure of the transition curves (Figure 47A) but sufficiently raises the eStance $v$-nullcline position to allow the limb to transition from the eSwing to the eStance phase.

To our knowledge, this locomotor recovery, although observed experimentally with locomotor training of various types [58, 4, 60, 24, 59, 61], has not been analyzed using dynamical systems methods in previous models. Our analysis predicts that restored oscillations will be particularly susceptible to perturbations near the onset of stance and that modulation of $Ib$-$E$ feedback signals would be particularly effective for restoring or speeding up oscillations under SCI. For the restored oscillations, we also observe that velocity can decrease during part of the eStance phase, due to a rapid change in $Mn$-$E$ output strength resulting from the cessation of the $Ib$-$E$ feedback signal, but that because this output saturates, velocity subsequently increases and the eStance phase can be completed. Interestingly, this analysis generalizes to imply that there will exist a critical curve in the space of feedback strengths and drive levels, such that parameter values above this curve are required to sustain oscillations, with more feedback needed as drive decreases. For example, partial restoration of

drive effects via electrical stimulation or other manipulations could reduce the amount of training-induced feedback strength enhancement required for locomotion. A dip in the limb velocity profile during eStance may signify that the system is near this critical curve and hence lies in a state where it is particularly susceptible to lose its rhythmicity via alterations in $Ib\text{-}E$ feedback and $Mn\text{-}E$ output.

## 4.4  CONTROL SIGNALS EXPRESSED AS THE DESIRED SPEED OF MOVEMENT

We saw in the previous section that feedback contributes to recovery after spinal cord injury because it promotes a necessary alignment between the limb trajectory and the limb nullcline at the onset of eStance. In this section, we analyze the contribution of feedback to another open question, regarding the signals produced to control locomotion. In a simpler, limbless model of an open loop half-center CPG, parameters were obtained that fit the output of the CPG to the phase asymmetry seen in the Halbertsma data [31] as a constant input varied [83]. Given a fixed input $d$, the CPG generated a rhythm of a particular duration ($T(d)$). In absence of a limb, the period of the CPG represented the duration of the step cycle, with the stance phase considered to be synonymous with the extensor phase and the swing phase synonymous with the flexor phase. In that model, as $d$ increased, $T(d)$ decreased due to changes in the extensor duration only (the flexor duration remained relatively constant). Thus, the period of the CPG exhibited an asymmetric response to changes in drive. This period could then be translated into forward velocity ($V_G$) using an equation based on a previously described power function [27],

$$T(d) = 0.5445 V_G^{-0.5925}. \tag{4.1}$$

We will refer to this calculation of velocity as the Goslow velocity. The CPG input ($d$) was plotted against Goslow velocity ($V_G$) and the resulting relationship was highly linear (with an $r^2$ value of 0.9978). This finding supported the idea that the CPG could be configured to receive drive signals which encode the desired speed of the animal [83].

134

In the original limbed neuromechanical Markin model, supra-spinal input (drive) generates a rhythm of a particular duration, and the relationship between input and velocity can be obtained using equation (4.1). Not surprisingly, the relationship is again fairly linear due to the quality of fit that the model exhibits with the Halbertsma data (Figure 48). Up to
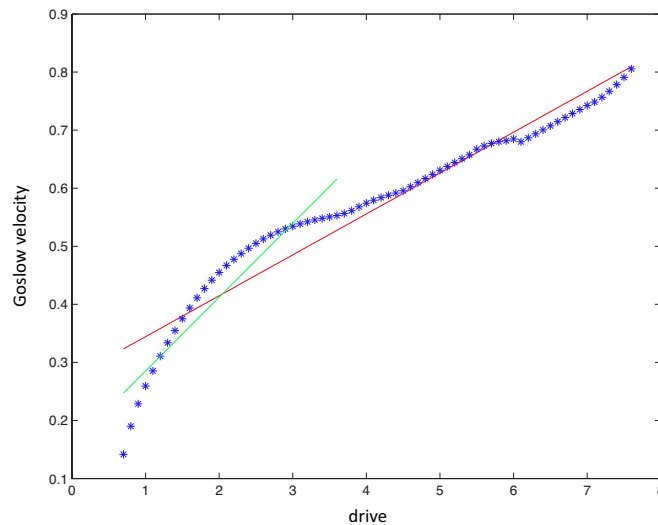


**Figure 48:** *Velocity of limb versus drive strength for a large drive range. Goslow velocity is plotted in blue against drive. Red and green linear regression are computed over the entire range and over the normal range of drives, with correlation coefficients of 0.9164 and 0.889, respectively.*

this point we have only considered the performance of the model over the range of drives for which it was fit ($d \in [0.7, 3.6]$). In Figure 48, we extend our consideration to a much larger input range to verify that under this calculation the model can reach the same range of speeds represented by the limbless model. The preferred speed of cats is around 0.4-0.5m/s (though cats can walk at much faster speeds), and this data indicates the Markin model is indeed capable of reaching sufficient speeds before breakdown. Over the normal and the wider drive range, the relationship between $V$ and $d$ is fairly linear, with a slightly larger $r^2$ value over the longer range of drives. These results indicate further support that control signals driving this network are expressed in the desired locomotor speed.

How robust is this linearity to changes in feedback? We calculate the relationship between drive and Goslow velocity as the strength of the feedback varies from its baseline in Figure 49. Over the normal range, $r^2$ values indicate that both increasing and decreasing
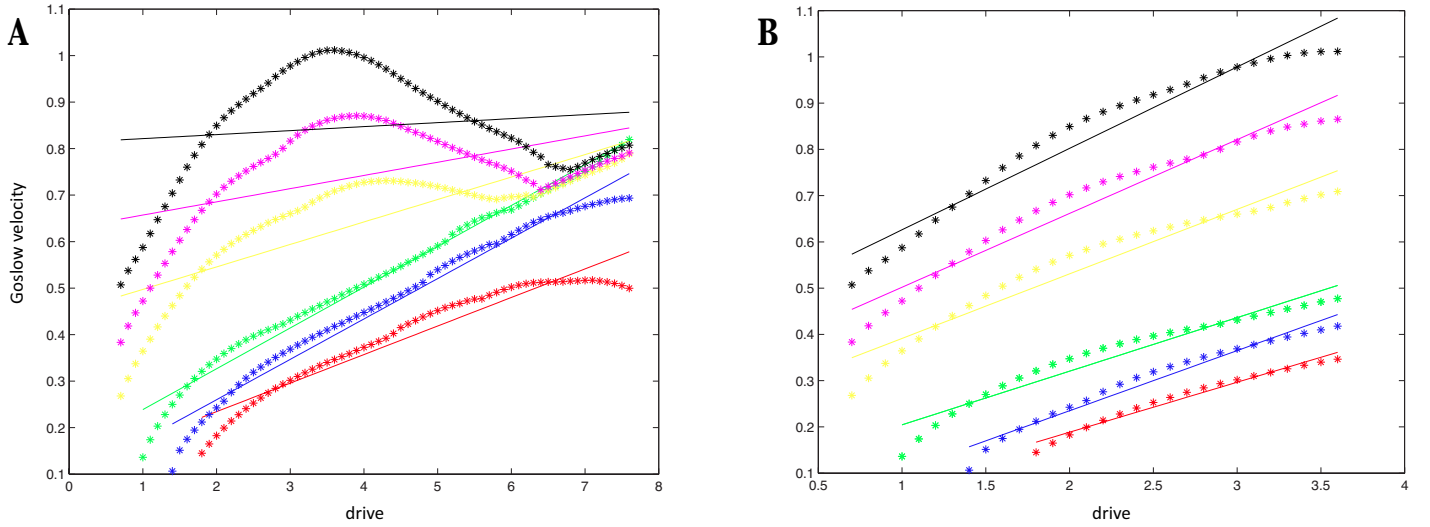
**Figure 49:** *Drive vs. velocity shown for various feedback strengths in each of the velocity calculations. Red, blue, green, yellow, magenta, and black stars indicate the model output at 70, 80, 90, 110, 120, 130% of normal feedback strength, respectively. Linear regression lines are plotted with corresponding colors. (A) $r^2$ values were computed over a large range of drives with values of 0.9243, 0.9751, 0.9842, 0.6716, 0.2575, and 0.0205 corresponding to the strength of feedbacks previously indicated. (B) Linear fit was only calculated over the range of normal drives, with values of 0.9747, 0.9629, 0.9351, 0.9316, 0.9523, and 0.9458.*

the feedback would improve the linearity of the relationship between drive and velocity. Decreased feedback strength, however, reduces the range of drives over which the model oscillates, in particular the lower range (the crucial regime that generates the asymmetry). Increasing the feedback, while increasing the linearity over the normal range, significantly decreases linearity over the full range (Figure 49). This leads us to conclude that the baseline feedback appears to be configured at an optimal level with respect to producing linearity over the widest range of drive values.

Note that for large feedback strengths, the model produces the counterintuitive result that increases in drive lead to decreases in velocity. Since V and T are inversely related (equation 4.1), this is equivalent to the result that step durations begin to increase with

drive when drive is sufficiently large (see Figure 51A). Intuitively, stronger feedback should lead to a speed up in step duration – the mechanism of oscillations under presence of feedback occurs through escape of the silent $In$, which is controlled entirely by feedback. Thus when feedback strength is increased, the voltage of the silent $In$ should be able to reach threshold more quickly than in the normal case (see the discussion in section 3.2.3 and Figure 30). In this case, however, that event does not immediately initiate the transition in the CPG. Since the excitation to the cells is very large, active neurons can access much larger voltages than in the normal case, and thus can provide much stronger inhibition to an $RG$ in the silent phase, which will delay that neuron from entering the active phase. Figure 50 shows the difference between nullclines under normal feedback strength and increased feedback strength. Under baseline feedback, once the silent $In$ hits threshold, inhibition to the silent $RG$ is sufficiently reduced so that the nullcline immediately drops (left and middle plot) and $RG$ is able to jump to the active phase. Under increased feedback, notice that the silent $In$ has already crosses threshold, but the silent nullcline is still raised in phase space, since the voltage of the active $In$ is very large. Thus at large feedback values, the limb sends a signal to the CPG to make a switch at a time when it is not equipped to do so.

The model analysis indicates two particular pathways in the CPG that could be modulated to reduce this delay and promote frequency increases even under strong feedback. The first method would be to reduce the excitation from $RG$ to $In$, which would counteract the flood of excitation present in the CPG. Alternatively, if the strength of inhibition from $In$ to $RG$ was lowered, then the silent $RG$ would lie on a less inhibited nullcline, and thus able to hit the knee sooner. Figure 51 shows that altering the connections within the CPG in either of these ways reduces the increase in step speed for large drives. Interestingly, both decreasing excitation and inhibition within the CPG can produce qualitatively similar results, suggesting that entrainment can occur through various system modifications. This also provides additional support for the benefits of model analysis, since counterintuitive changes in parameter values can yield favorable results.

Note that the Goslow velocity is calculated from the data through which the models are fit. An advantage of the Markin model over the limbless model is that the limb dynamics can produce a different velocity calculation, as the ratio of distance and time. Distance

137
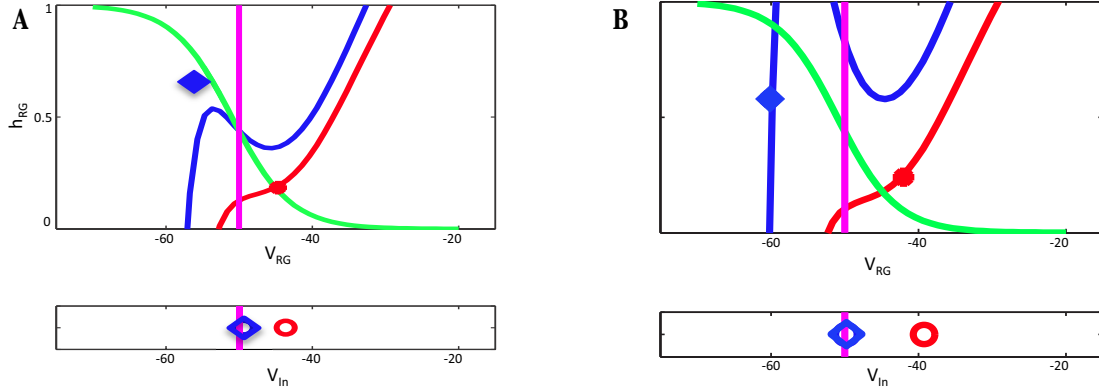
**Figure 50:** *Transition from RG-F to RG-E's active phase under (A) normal feedback and (B) at 130% of baseline. In each plot, top frame shows the nullclines in RG phase space and the bottom frame tracks the activity of $In$ (blue corresponds to extensor and red corresponds to flexor). (A) Under normal feedback strength, $In$-$E$ crosses threshold and the nullcline immediately drops, so that $RG$-$E$ is above the knee and can jump to the active phase. (B) Under increased feedback strength, when $In$-$E$ escapes, strong inhibition from $In$-$F$ delays $RG$-$E$ from entering the active phase.*

is an organic result of the modeling, which makes this description of velocity particularly interesting to study. We can calculate the total distance traveled by the animal as the distance between the end of the rigid limb at stance onset and swing onset. Given that the length of the limb is 0.3 meters, the total distance traveled is $0.3(\cos(q_{min}) + \cos(\pi - q_{max})) = 0.3(\cos(q_{min}) - \cos(q_{max}))$. Here, $q_{min}$ corresponds to the angle the hip makes with the horizontal at touch down and $q_{max}$ the angle at lift. Thus the joint velocity can be calculated as

$$V_J = (0.3(\cos(q_{min}) - \cos(q_{max})))/T. \tag{4.2}$$

We plot the relationship between $V_J$ and drive in Figure 52. Over the normal range, this relationship is even more linear than the Goslow relationship, producing an $r^2$ value of 0.9698. Outside of this range, however, the joint velocity peaks at a top speed of roughly 0.3 m/s and begins to decrease with increases in drive, contrary to what we might expect.

What contributes to this velocity decrease? Simulations show that outside of the normal
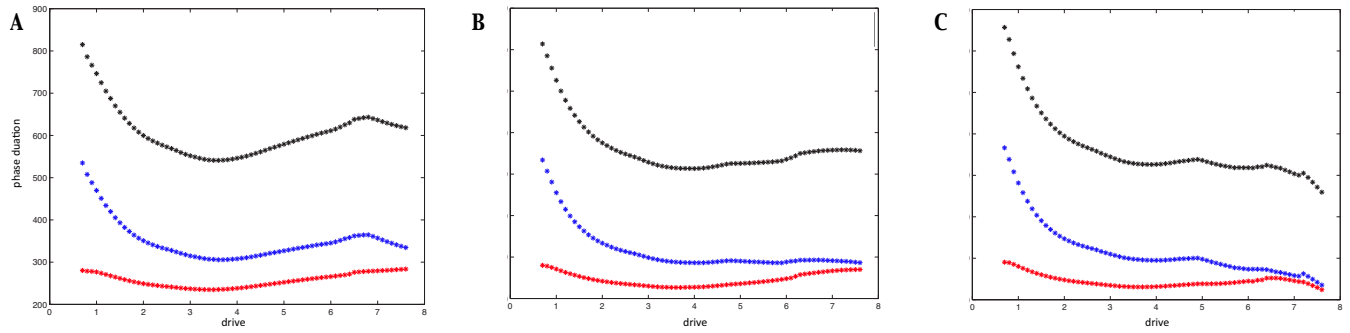
**Figure 51:** *Step, stance, and swing phase durations under (A) baseline excitation/inhibition, (B) decreased excitation from RG to In, (C) decreased inhibition from In to RG. Under large feedback strength, increases in drive lead to counterintuitive increases in phase duration (A), but various modifications to connectivity in the CPG can promote frequency increases with increase in drive (B), (C).*
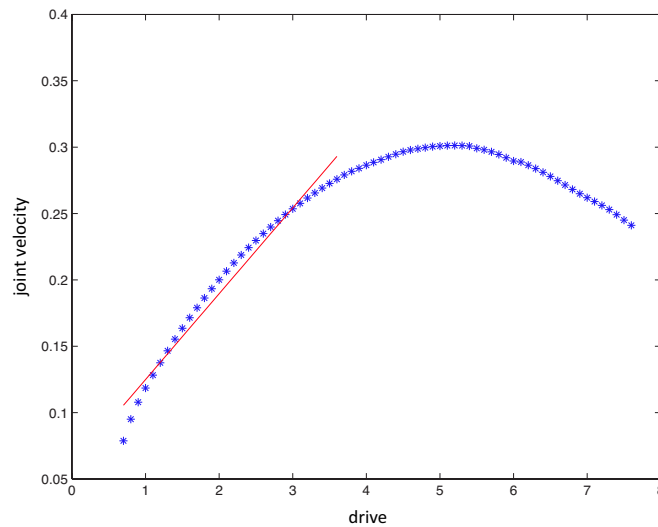


**Figure 52:** *Joint velocity of limb versus drive strength over a large drive range. This calculation indicates that at relatively high drive values, increases in drive correspond to decreases in velocity. This relationship is linear, however, over the normal range of drives with an $r^2$ value of 0.9698.*

drive range, velocity dips because the distance traveled by the animal eventually begins to decrease with drive, due to an increasing touch down angle $q_{min}$ (recall that $q$ indicates the angle the limb has with the horizontal, so larger touch down angles indicate stepping down with an orientation closer to upright). This is counterintuitive, as faster walking should accommodate farther distances and wider deviations from vertical, exhibiting a limitation of the model when we consider its performance outside of the normal drive range.

To conclude, this model agrees with findings produced by the limbless model, which suggest that input signals to the CPG may be expressed as the desired speed of movement. Our result is particularly significant, since we verify this finding in a different representation of speed which is based on an observable not directly fit to experimental data (at least over the normal range of drives we have considered).

## 4.5   DISCUSSION

In normal overground locomotion, frequency increases occur due to decreases in stance phase duration only. Many past works support the hypothesis that the spinal locomotor CPG features a symmetric organization [41, 84, 64, 39, 48], such that the asymmetric response would require other sources such as feedback asymmetries. However, other authors argue that the CPG itself is a source of asymmetry [26]. Asymmetry within a model CPG emerged from a numerical optimization procedure tuned to fit parameters to the asymmetric phase response data [31, 83], and asymmetries allowed a model CPG to fit disordered limb coordination data from Parkinson's disease patient [3], but these results were inevitable, since the models involved did not include possible sources of asymmetry outside of the CPG, such as feedback [3, 83]. An interesting future direction would be to repeat these studies in a neuromechanical model, such that the relative capabilities of different possible asymmetry sources could be compared. Biologically, sources of locomotor asymmetry may vary across species or even across behavioral or environmental contexts, and in fact there may be multiple asymmetries within a single locomotor network.

In Section 4.1, we elucidated the crucial role of the limb dynamics in generating the

phase asymmetry exhibited by the full model, and used an array of arguments to explain why only the eStance phase duration depended on the value of the supra-spinal drive to the CPG. More specifically, we found that the inclusion of the ground reaction force, which was present during stance but not during swing, imposed an intrinsic asymmetry on the mechanical component of the system, which we found to be crucial in constraining the range of drives over which oscillations could occur and in eliciting the phase response asymmetry (Section 4.1.6). The strength of the feedback (particularly the $Ib\text{-}E$ feedback term) in the model scaled the intensity of this asymmetry. Interestingly, the same mechanisms that yielded contraction in the eStance phase were identified as being responsible for the sensitivity of the phase duration to the drive strength there. Decreasing the amplitude of the ground reaction force reduced this asymmetry and decreased the duty cycle, replicating conclusions obtained from reduced load experiments (Section 4.2).

In Section 4.3, we investigated the effect of increased feedback strength on the system after the removal of supra-spinal drive, which simulated SCI. We showed how strengthening the feedback could restore the conditions needed for limb oscillations and how the resulting oscillations differed from model rhythms present under baseline conditions. Analysis of this recovery revealed that sufficiently weak CPG output could render the limb unable to oscillate by failing to allow the limb to assume a positive velocity at the onset of the stance phase. The model exhibited an interesting dependence on the degrees to which different feedback signals were strengthened, which we were able to explain by elucidating the contribution of particular feedbacks to the shape of the transition curves and the position of the $v$-nullcline at eStance onset.

After SCI, restored oscillations maintained transitions by escape, the same mechanism responsible for oscillations in the normal case. The consistency in transition mechanisms, and hence in frequency responses to input variations, across these different oscillation regimes is in agreement with the general idea that top-down and feedback sensory signals to a locomotor CPG can together synergistically encode a targeted locomotor speed. This concept was explored with top-down input only to the CPG in a limbless model in [83]. In Section 4.4, we extended this discussion by showing that inputs to the CPG from both supra-spinal drive and limb feedback were expressed in the desired frequency of limb movement, using various

definitions of speed.

Our results are consistent with past work in which a genetic algorithm was applied to evolve a set of model CPG networks, each composed of three, four, or five recurrently-connected neurons, controlling the activity of a simulated leg of an insect-like body [6, 13, 5]. The passage of a solution trajectory close to a fold of a steady state input-output curve was found to elongate the duration of the stance phase, resembling the dynamics exhibited at the onset of the eStance phase in our model. Interestingly, the model correspondingly exhibited a high sensitivity to perturbations near this region [13], similar to the dynamics exhibited at the onset of the eStance phase in our model. Indeed, the dynamic mechanisms that we have uncovered also predict such a sensitivity, along with several other expected outcomes relating to step failure and responses to disturbances, especially at relatively low drive levels. Specifically, a kick that slightly decreased limb angle late in the eSwing phase, when the limb speed is small, could terminate oscillations if it caused the trajectory to enter the eStance phase to the left of the eStance critical point. Similarly, a perturbation in the direction of larger limb velocity arriving in the fStance phase might push the trajectory above the stable manifold of the fStance critical point, which would prevent it from completing that phase, or might lead to very long fStance durations, if it pushed the trajectory very close to the stable manifold. Swing phase durations should be less sensitive to perturbations, on the other hand. These ideas are also related to past numerical simulations of a qualitatively similar but more simplified model, which showed that combined feedforward and feedback signaling yields an overall improved robustness to unexpected disturbances and imperfect sensory information, relative to pure feedback or feedforward control, although differences across phases were not emphasized there [40].

The analysis that we have done stands apart from past mathematical work on related models in that the model that we consider was generated to reproduce a variety of qualitative and quantitative experimental observations, and as such was not tailored to provide ease in analysis. Indeed, we saw that despite the relative simplicity of the model, its dynamic inhibition, excitation, and nonlinear feedback components presented challenges that complicated our analysis, and these features also prevented the application of additional analytical techniques, such as phase response curves (e.g., [56]). However, we were able to

142

utilize variations of many familiar arguments from the realm of dynamical systems, in spite of this complexity.

# 5.0 CONCLUSION

In this thesis, we used simplified mathematical models to investigate how network structure and sensory inputs contributed to rhythmic movements. In Chapter 2, we proposed various structures that were capable of producing distinct swim and scratch patterns under different levels of stimulation. We found that in order to reproduce an experimental benchmark regarding swim frequency increases, transitions in the swim network must occur via the escape mechanism, where recovery from adaption allows inhibited neurons to overcome suppression from other neurons. We generated collections of parameters sets that were able to produce swim and scratch in the various modeling structures, and tested those sets for their performance under dual stimulation. Random parameter generation was not able to produce sets exhibiting dynamics that we desired, which corresponded to tonic steady state activity by one or more neurons as the stimulus strength was decreased. We used analysis on a simplified system to generate inequalities that constrained parameter space, such that a targeted search in this regime generated sets that produced desired dynamics. We concluded that a network structure comprised of multifunctional and specialized neurons was most likely to have generated experimental observations, given its ability to reproduce all of the experimental benchmarks we were considering. This corroborates with conclusions from our collaborators, who deduced that distinct rhythms produced by the same motoneurons and muscles likely share key circuitry [32].

In Chapters 3 and 4, we analyzed the performance of a neuromechanical model that operated under feedback control. Though the CPG was able to oscillate in the open loop configuration, we found that when feedback was present, CPG switches occurred at a particular relationship between limb angle and velocity, reminiscent of if-then rules suggested by Cruse, and more recently, Prochazka. We proved the existence of the separate mecha-

nisms present when feedback was absent and present, and used these observations to proffer a reduced model that was tractable for rigorous discussion. Discontinuities in the dynamics required us to adapt theorems from classical dynamic systems theory before applying them to our analysis. This analysis also highlighted the existence of a key relationship in the limb dynamics, where the proximity between components allowed the model to replicate a key feature of locomotion, constrained limb activity to promote a unique periodic orbit, and inhibited oscillations when the CPG was too weakly excited. We then utilized our understanding of the model to explain its response to changes in load and after spinal cord injury. Finally, we considered the relationship between input to the CPG and locomotor speed, extending conclusions made in [83].

The capability of CPG circuits to generate locomotor oscillations has received extensive attention in recent review papers with various perspectives [29, 10, 52]. Many authors have worked on models of locomotor CPGs or, of particular relevance to this work, on models of combined CPG and limb dynamics. Several of these works have treated highly simplified closed loop neuromechanical systems, focusing on resonance between the CPG and the limb or CPG entrainment by the limb [34, 37, 81, 70]. Perhaps the most relevant to our approach, in which we analyze transition mechanisms within the CPG under different feedback conditions, is work by Sekerli and Butera [66]. These authors distinguish multiple possible phase transition mechanisms in their neuromechanical model, but these all involve the effects of feedback inhibition from the mechanical component to a half-center CPG, treated in as a synaptic current. In the model that we consider, all feedback signals are excitatory and the signals are more complicated, derived based on muscle stretch and velocity and motoneuron outputs [46]. Indeed, while dynamical systems methods have been used to understand CPG gait rhythm generation or closed loop neuromechanical model dynamics with perturbative feedback signals (e.g. [21, 56]), dynamical systems analysis of a closed loop neuromechanical locomotor model with excitatory, continuous or piecewise continuous afferent feedback signals (see especially [76]) still represents a frontier in this area.

While the neuromechanical model that we analyzed in Chapters 3 and 4 is complex from a mathematical point of view, it is undoubtedly extremely simplified relative to the actual spinal/limb interactions that occur in vivo. The CPG component of this model is

minimal, comprised of extensor and flexor rhythm generator neurons, interneurons, and pattern formation neurons, each represented by a single model neuron. Furthermore, the limb in the model is a simple, single-joint segment, able to move with only one degree of freedom through the actions of only two antagonistic muscles, and the interaction of the limb and ground is incorporated in a very basic way that neglects many possible effects. Future work to address these limitations will be important, as will additional modeling to incorporate the control and interaction of multiple limbs and corresponding CPG units.

We are currently considering extensions to this model. We aim to implement specific forcing terms that represent the interaction between the limb and the treadmill during treadmill locomotion. We intend to investigate how this modification affects the mechanisms responsible for rhythm generation, and how changes in drive and feedback levels affect the performance of the model in this case.

# BIBLIOGRAPHY

[1] MJ Angel, P. Guertin, T. Jimenez, and DA McCrea, *Group I extensor afferents evoke disynaptic EPSPs in cat hindlimb extensor motorneurones during fictive locomotion.*, The Journal of Physiology **494** (1996), no. Pt 3, 851–861.

[2] M.J. Angel, E. Jankowska, and D. McCrea, *Candidate interneurones mediating group I disynaptic EPSPs in extensor motoneurones during fictive locomotion in the cat*, The Journal of Physiology **563** (2005), no. 2, 597–610.

[3] Y. Asai, T. Nomura, S. Sato, A. Tamaki, Y. Matsuo, I. Mizukura, and K. Abe, *A coupled oscillator model of disordered interlimb coordination in patients with parkinson's disease*, Biological Cybernetics **88** (2003), no. 2, 152–162.

[4] H. Barbeau, D.A. McCrea, M.J. O'Donovan, S. Rossignol, W.M. Grill, and M.A. Lemay, *Tapping into spinal circuits to restore motor function*, Brain Research Reviews **30** (1999), 27–51.

[5] R D Beer, H J Chiel, and J C Gallagher, *Evolution and analysis of model cpgs for walking: Ii. general principles and individual variability*, Journal of Computational Neuroscience **7** (1999), no. 2, 119–147.

[6] R D Beer and J C Gallagher, *Evolving dynamical neural networks for adaptive behavior*, Adaptive Behavior **1** (1992), no. 1, 91.

[7] K.L. Bellman and F.B. Krasne, *Adaptive complexity of interactions between feeding and escape in crayfish*, Science **221** (1983), no. 4612, 779–781.

[8] MB Berkinblit, TG Deliagina, AG Feldman, IM Gelfand, and GN Orlovsky, *Generation of scratching. i. activity of spinal interneurons during scratching*, Journal of Neurophysiology **41** (1978), no. 4, 1040–1057.

[9] A. Berkowitz, *Multifunctional and specialized spinal interneurons for turtle limb movements*, Annals of the New York Academy of Sciences **1198** (2010), no. 1, 119–132.

[10] K.L. Briggman and W.B. Kristan, Jr., *Multifunctional pattern-generating circuits*, Annual Review of Neuroscience **31** (2008), 271–294.

147

[11] T G Brown, *The intrinsic factors in the act of progression in the mammal*, Proceeding of the Royal Society London. Series B. **84** (1911), no. 572, 308–319.

[12] T.G. Brown, *On the nature of the fundamental activity of the nervous centres; together with an analysis of the conditioning of rhythmic activity in progression, and a theory of the evolution of function in the nervous system*, Journal of Physiology **48** (1914), no. 1, 18.

[13] H J Chiel, R D Beer, and J C Gallagher, *Evolution and analysis of model cpgs for walking: I. dynamical modules*, Journal of Computational Neuroscience **7** (1999), no. 2, 99–118.

[14] H. Cruse, *What mechanisms coordinate leg movement in walking arthropods?*, Trends Neuroscience **13** (1990), no. 1, 15–21.

[15] S.N. Currie and PS Stein, *Electrical activation of the pocket scratch central pattern generator in the turtle*, Journal of Neurophysiology **60** (1988), no. 6, 2122–2137.

[16] R. Curtu, *Singular hopf bifurcations and mixed-mode oscillations in a two-cell inhibitory neural network*, Physica D: Nonlinear Phenomena **239** (2010), no. 9, 504–514.

[17] R. Curtu and J. Rubin, *Interaction of canard and singular hopf mechanisms in a neural model*, SIAM Journal on Applied Dynamical Systems **10** (2011), 1443.

[18] R. Curtu, A. Shpiro, N. Rubin, and J. Rinzel, *Mechanisms for frequency control in neuronal competition models*, SIAM Journal on Applied Dynamical Systems **7** (2008), no. 2, 609.

[19] S. Daun, J.E. Rubin, and I.A. Rybak, *Control of oscillation periods and phase durations in half-center central pattern generators: a comparative mechanistic analysis*, Journal of Computational Neuroscience **27** (2009), no. 1, 3–36.

[20] S. Daun-Gruhn, *A mathematical modeling study of inter-segmental coordination during stick insect walking*, Journal of Computational Neuroscience (2011), 1–24.

[21] S. Daun-Gruhn and T.I. Tóth, *An inter-segmental network model and its use in elucidating gait-switches in the stick insect*, Journal of Computational Neuroscience **31** (2011), no. 1, 43–60.

[22] G.M. Earhart and P.S.G. Stein, *Scratch-swim hybrids in the spinal turtle: blending of rostral scratch and forward swim*, Journal of Neurophysiology **83** (2000), no. 1, 156–165.

[23] _____, *Step, swim, and scratch motor patterns in the turtle*, Journal of Neurophysiology **84** (2000), no. 5, 2181–2190.

[24] V.R. Edgerton, N.J. Tillakaratne, A.J. Bigbee, R.D. De Leon, and R.R. Roy, *Plasticity of the spinal circuit after injury*, Annual Review of Neuroscience **27** (2004), 145–167.

[25] G.B. Ermentrout and D. Terman, *Mathematical foundations of neuroscience*, vol. 35, Springer Verlag, 2010.

[26] A. Frigon and J.P. Gossard, *Asymmetric control of cycle period by the spinal locomotor rhythm generator in the adult cat*, The Journal of Physiology **587** (2009), no. 19, 4617–4628.

[27] G.E. Goslow Jr, R.M. Reinking, and D.G. Stuart, *The cat step cycle: hind limb joint angles and muscle lengths during unrestrained locomotion*, Journal of Morphology **141** (1973), no. 1, 1–41.

[28] S Grillner, *Control of locomotion in bipeds, tetrapods, and fish*, Handbook of Physiology. The Nervous System: Motor Control, Sect. 1, Vol. II, Pt. 2 (VB Brooks, ed.), American Physiological Society, Bethesda, MD, 1981, pp. 1179–1236.

[29] S. Grillner, *Biological pattern generation: the cellular and computational logic of networks in motion*, Neuron **52** (2006), no. 5, 751–766.

[30] J. Guckenheimer and P. Holmes, *Nonlinear oscillations, dynamical systems, and bifurcations of vector fields*, vol. 42, Springer-Verlag, 1997.

[31] J.M. Halbertsma, *The stride cycle of the cat: the modelling of locomotion by computerized analysis of automatic recordings.*, Acta Physiologica Scandinavica Supplementum **521** (1983), 1.

[32] Z.Z. Hao, L.E. Spardy, E.B.L. Nguyen, J.E. Rubin, and A. Berkowitz, *Strong interactions between spinal cord networks for locomotion and scratching*, Journal of Neurophysiology **106** (2011), no. 4, 1766–1781.

[33] R.M. Harris-Warrick and E. Marder, *Modulation of neural networks for behavior*, Annual review of neuroscience **14** (1991), no. 1, 39–57.

[34] N.G. Hatsopoulos, *Coupling the neural and physical dynamics in rhythmic movements*, Neural Computation **8** (1996), no. 3, 567–581.

[35] H.B. Hayes, Y.H. Chang, and S. Hochman, *An in vitro spinal cord-hindlimb preparation for studying behaviorally relevant rat locomotor function*, Journal of Neurophysiology **101** (2009), no. 2, 1114.

[36] YP Ivanenko, R. Grasso, V. Macellari, and F. Lacquaniti, *Control of foot trajectory in human locomotion: role of ground contact forces in simulated reduced gravity*, Journal of Neurophysiology **87** (2002), no. 6, 3070.

[37] T. Iwasaki and M. Zheng, *Sensory feedback mechanism underlying entrainment of central pattern generator to mechanical resonance*, Biological Cybernetics **94** (2006), no. 4, 245–261.

[38] J. Juranek and S.N. Currie, *Electrically evoked fictive swimming in the low-spinal immobilized turtle*, Journal of Neurophysiology **83** (2000), no. 1, 146–155.

[39] L. Juvin, J. Simmers, and D. Morin, *Locomotor rhythmogenesis in the isolated rat spinal cord: a phase-coupled set of symmetrical flexion–extension oscillators*, The Journal of Physiology **583** (2007), no. 1, 115.

[40] A.D. Kuo, *The relative roles of feedforward and feedback in the control of rhythmic movements*, Motor Control **6** (2002), no. 2, 129–145.

[41] M. Lafreniere-Roula and D A McCrea, *Deletions of rhythmic motoneuron activity during fictive locomotion and scratch provide clues to the organization of the mammalian central pattern generator*, Journal of Neurophysiology **94** (2005), no. 2, 1120.

[42] P.R. Lennard and P.S. Stein, *Swimming movements elicited by electrical stimulation of turtle spinal cord. i. low-spinal and intact preparations*, Journal of Neurophysiology **40** (1977), no. 4, 768–778.

[43] P.L. Lutz and S.L. Milton, *Negotiating brain anoxia survival in the turtle*, Journal of Experimental Biology **207** (2004), no. 18, 3141–3147.

[44] E. Marder and R.L. Calabrese, *Principles of rhythmic motor pattern generation*, Physiological reviews **76** (1996), no. 3, 687–717.

[45] E. Marder and JM Weimann, *Modulatory control of multiple task processing in the stomatogastric nervous system*, Neurobiology of Motor Progamme Selection (1992), 3–19.

[46] S.N. Markin, A.N. Klishko, N.A. Shevtsova, M.A. Lemay, B.I. Prilutsky, and I.A. Rybak, *Afferent control of locomotor cpg: Insights from a simple neuro-mechanical model*, Cellular and Network Functions in the Spinal Cord (J. Fetcho, S. Hochman, A. McDermott, P. Stein, and L. Ziskind-Conhaim, eds.), Annals of the New York Academy of Sciences, New York Academy of Sciences, 2010.

[47] A.S. Matveev and A.V. Savkin, *Qualitative theory of hybrid dynamical systems*, Birkhauser, 2000.

[48] D A McCrea and I A Rybak, *Modeling the mammalian locomotor cpg: insights from mistakes and perturbations*, Progress in Brain Research **165** (2007), 235–253.

[49] D.A. McCrea and I.A. Rybak, *Organization of mammalian locomotor rhythm and pattern generation*, Brain Research Reviews **57** (2008), no. 1, 134–146.

[50] L.I. Mortin, J. Keifer, and PS Stein, *Three forms of the scratch reflex in the spinal turtle: movement analyses*, Journal of Neurophysiology **53** (1985), no. 6, 1501–1516.

[51] L.I. Mortin and PS Stein, *Spinal cord segments containing key elements of the central pattern generators for three forms of scratch reflex in the turtle*, The Journal of neuroscience **9** (1989), no. 7, 2285–2296.

[52] B. Mulloney and C. Smarandache, *Fifty years of CPGs: two neuroethological papers that shaped the course of neuroscience*, Frontiers in Behavioral Neuroscience (2010), DOI 10.3389/fnbeh.2010.00045.

[53] A. Prochazka, *Quantifying proprioception*, Progress in Brain Research **123** (1999), 133–142.

[54] A. Prochazka and M. Gorassini, *Models of ensemble firing of muscle spindle afferents recorded during normal locomotion in cats*, The Journal of Physiology **507** (1998), no. 1, 277.

[55] A. Prochazka and S. Yakovenko, *Predictive and reactive tuning of the locomotor cpg*, Integrative and Comparative Biology **47** (2007), no. 4, 474–481.

[56] J. Proctor and P. Holmes, *Reflexes and preflexes: on the role of sensory feedback on rhythmic patterns in insect locomotion*, Biological Cybernetics **102** (2010), no. 6, 513–531.

[57] G.A. Robertson, L.I. Mortin, J. Keifer, and PS Stein, *Three forms of the scratch reflex in the spinal turtle: central generation of motor patterns*, Journal of neurophysiology **53** (1985), no. 6, 1517–1534.

[58] S. Rossignol, *Neural control of stereotypic limb movements*, Handbook of physiology, Section 12. Exercise: Regulation and Integration of Multiple Systems (L.B. Rowell and J.T. Shepherd, eds.), American Physiological Society, Oxford, UK, 1996, pp. 173–216.

[59] S. Rossignol and L. Bouyer, *Adaptive mechanisms of spinal locomotion in cats*, Integrative and Comparative Biology **44** (2004), 71–79.

[60] S. Rossignol, L. Bouyer, D. Barthelemy, C. Langlet, and H. Leblond, *Recovery of locomotion in the cat following spinal cord lesions*, Brain Research Reviews **40** (2002), no. 1-3, 257–266.

[61] S. Rossignol, R. Dubuc, and J.P. Gossard, *Dynamic sensorimotor interactions in locomotion*, Physiological Reviews. **86** (2006), 89–154.

[62] J.E. Rubin, *Bursting induced by excitatory synaptic coupling in nonidentical conditional relaxation oscillators or square-wave bursters*, Physical Review E **74** (2006), no. 2, 21917.

[63] H. Ruckstuhl, J. Kho, M. Weed, M.W. Wilkinson, and A.R. Hargens, *Comparing two devices of suspended treadmill walking by varying body unloading and froude number*, Gait & posture **30** (2009), no. 4, 446–451.

[64] I A Rybak, K. Stecina, N A Shevtsova, and D A McCrea, *Modelling spinal circuitry involved in locomotor pattern generation: insights from the effects of afferent stimulation*, Journal of Physiology **577** (2006), no. 2, 641.

[65] I.A. Rybak, N.A. Shevtsova, M. Lafreniere-Roula, and D.A. McCrea, *Modelling spinal circuitry involved in locomotor pattern generation: insights from deletions during fictive locomotion*, The Journal of Physiology **577** (2006), no. 2, 617–639.

[66] M. Sekerli and R.J. Butera, *Oscillations in a simple neuromechanical system: Underlying mechanisms*, Journal of Computational Neuroscience **19** (2005), no. 2, 181–197.

[67] C.S. Sherrington, *Flexion-reflex of the limb, crossed extension-reflex, and reflex stepping and standing*, The Journal of physiology **40** (1910), no. 1-2, 28.

[68] A. Shpiro, R. Curtu, J. Rinzel, and N. Rubin, *Dynamical characteristics common to neuronal competition models*, Journal of Neurophysiology **97** (2007), no. 1, 462.

[69] S.N. Simic, K.H. Johansson, J. Lygeros, and S. Sastry, *Hybrid limit cycles and hybrid Poincaré-Bendixson*, IFAC World Congress, Barcelona, Spain, Citeseer, 2002.

[70] M.F. Simoni and S. DeWeerth, *Sensory feedback in a half-center oscillator model*, IEEE Trans. Biomed. Eng **54** (2007), no. 2, 193–204.

[71] F.K. Skinner, N. Kopell, and E. Marder, *Mechanisms for oscillation and frequency control in reciprocally inhibitory model neural networks*, Journal of Computational Neuroscience **1** (1994), no. 1, 69–87.

[72] _____, *Mechanisms for oscillation and frequency control in reciprocally inhibitory model neural networks*, Journal of Computational Neuroscience **1** (1994), no. 1, 69–87.

[73] F.K. Skinner, G.G. Turrigiano, and E. Marder, *Frequency and burst duration in oscillating neurons and two-cell networks*, Biological Cybernetics **69** (1993), no. 5, 375–383.

[74] _____, *Frequency and burst duration in oscillating neurons and two-cell networks*, Biological Cybernetics **69** (1993), no. 5, 375–383.

[75] L.E. Spardy, S.N. Markin, N.A. Shevtsova, B.I. Prilutsky, I.A. Rybak, and J.E. Rubin, *A dynamical systems analysis of afferent control in a neuromechanical model of locomotion: I. rhythm generation*, Journal of Neural Engineering **8** (2011), 065003.

[76] _____, *A dynamical systems analysis of afferent control in a neuromechanical model of locomotion: I. phase asymmetry*, Journal of Neural Engineering **8** (2011), 065004.

[77] P.S.G. Stein, G.A. Robertson, J. Keifer, M.L. Grossman, J.A. Berenbeim, and P.R. Lennard, *Motor neuron synaptic potentials during fictive scratch reflex in turtle*, Journal of Comparative Physiology A: Neuroethology, Sensory, Neural, and Behavioral Physiology **146** (1982), no. 3, 401–409.

[78] R. van den Brand, J. Heutschi, Q. Barraud, J. DiGiovanna, K. Bartholdi, M. Huerlimann, L. Friedli, I. Vollenweider, E.M. Moraud, S. Duis, et al., *Restoring voluntary control of locomotion after paralyzing spinal cord injury*, science **336** (2012), no. 6085, 1182–1185.

[79] X.J. Wang and J. Rinzel, *Alternating and synchronous rhythms in reciprocally inhibitory model neurons*, Neural Computation **4** (1992), no. 1, 84–97.

[80] ———, *Alternating and synchronous rhythms in reciprocally inhibitory model neurons*, Neural Computation **4** (1992), no. 1, 84–97.

[81] C.A. Williams and S.P. DeWeerth, *A comparison of resonance tuning with positive versus negative sensory feedback*, Biological Cybernetics **96** (2007), 603–614.

[82] D.M. Wilson, *The central nervous control of flight in a locust*, J. exp. Biol **38** (1961), no. 47, l–490.

[83] S. Yakovenko, *A hierarchical perspective on rhythm generation for locomotor control. in: Breathe, walk and chew, the neural challenge.*, Progress in Brain Research **188** (2011), 151–165.

[84] S. Yakovenko, D A McCrea, K. Stecina, and A. Prochazka, *Control of locomotor cycle durations*, Journal of Neurophysiology **94** (2005), no. 2, 1057–1065.